NORTHWESTERN UNIVERSITY

High Pressure Study of $Gd_5(Si_xGe_{1-x})_4$ Giant Magnetocaloric Materials Using X-ray Magnetic Circular Dichroism

A DISSERTATION

SUBMITTED TO THE GRADUATE SCHOOL

IN PARTIAL FULFILLMENT OF THE REQUIREMENTS

for the degree

DOCTOR OF PHILOSOPHY

Field of Materials Science and Engineering

By

Yuan-Chieh Tseng

EVANSTON, ILLINOIS

June 2009

ABSTRACT

High Pressure Study of $Gd_5(Si_xGe_{1-x})_4$ Giant Magnetocaloric Materials Using X-ray Magnetic Circular Dichroism

Yuan-Chieh Tseng

The role of Si-doping in enhancing the magnetic ordering temperature (T_c) of $Gd_5(Si_xGe_{1-x})_4$ giant magnetocaloric compounds was investigated using x-ray magnetic circular dichroism (XMCD) and diamond anvil cell (DAC) techniques. The purpose of the study is to understand the mechanism of doping-induced ferromagnetic order in these compounds that may advance the magnetic refrigeration technology. The results demonstrate that hydrostatic pressure leads to similar effects as Si-doping for $x \geq 0.125$ because the P-T phase diagram reproduces the most notable features of the x-T phase diagram, indicating that the magnetic properties of these compounds are volume-driven. The low-x ($0 < x \leq 0.75$) region exhibits an inhomogeneous magneto-structural ground state featured by a mixed antiferromagnetic (orthorhombic (II))$-$ferromagnetic (orthorhombic (I)) phase at low temperature. Pressure was found to remove this magneto-structural inhomogeneity by fully restoring the magnetization that is obtained for $x \geq 0.125$. However, unlike the nearly constant dT_c/dP obtained for $0.125 \leq x < 0.5$, dT_c/dP of the low-x samples is strongly

x-dependent. This suggests that the emergence of the ferromagnetic order from within the antiferromagnetic phase of Gd_5Ge_4 parent compound cannot be simply described as a volume-effect due to the existence of the magneto-structural inhomogeneity. Finally, the quantitative correspondence between Si-doping and hydrostatic pressure was examined in order to know if the properties of these materials are monotonically volume-dependent. It was found that Si-doping increases T_c much more effectively than pressure, by a factor of ~ 11 for a given volume reduction. A local lattice contraction was found around Si atoms as a result of the substitution of Ge by the smaller Si atoms resulting in a remarkably high local chemical pressure. This local contraction results in a stronger Si $3p$-Gd $5d$ orbital hybridization benefiting the indirect ferromagnetic exchange and hence responsible for a more effective T_c increase, overthrowing the concept prior to this study that macroscopic volume contraction is the major course determining T_c increase.

Approved

Professor Michael J. Bedzyk
Department of Materials Science and Engineering
Northwestern University Evanston, IL

Final Examination Committee:
Prof. Michael J. Bedzyk, Chair
Dr. Daniel Haskel
Dr. George Srajer
Prof. Christopher M. Wolverton
Prof. Mark C. Hersam

Acknowledgements

It is a great pleasure to thank the many people who made this thesis possible. My utmost gratitude goes to my Argonne advisor Dr. Daniel Haskel because of his selfless guidance throughout my graduate studies. I greatly appreciate his mentoring based on trust and friendship − working with him is an unforgettable experience. I also thank Prof. Bedzyk and Dr. Srajer for providing me with the opportunity to work at Argonne National Laboratory. I also appreciate Prof. Wolverton and Prof. Hersam for their valuable comments in my final exam. In addition, I need to thank Dr. N. M Souza-Neto for the precious partnership in all experiments, and also Dr. S. Sinogeikin and Dr. Y. Ding for enriching my knowledge in high pressure field. Besides, Dr. Y. Choi, Dr. M. A. Laguna-Marco, Dr. J. C. Lang who provided important suggestions to my thesis deserve my acknowledgement as well. I am very thankful for having been a member of the Magnetic Materials Group and I appreciate every single person in this group who ever helped me over the past 3 years.

I can't neglect Prof. V. K. Pecharsky, Prof. K. A. Gschneidner, Dr. Ya. Mudryk, and Dr. D. Paudyal at Ames Laboratory for their remarkable contributions to the magnetocaloric materials project. I also thank my Northwestern colleagues, V. Kohli, Z. Feng, M. McBriarty, J. Alaboson, J. Emery, S. Christensen, J. Klug, and C.Y. Leung for enriching my graduate life. I would also like to express my gratitude to Ching-Hui for joining my life in my last year at Northwestern, making my life never alone. Moreover, I especially thank my best roommate and colleague, Jui-Ching (Phillip) Lin for accompanying me to Northwestern a few years ago and

walking through different life experience together. I appreciate the encouragements given by a few close friends including Wei-Chih, Nicole, Shu-Te, Shan-Wei, Meng-Chun, Ching-Hsuan, Yu-Chen, Yi-Kai, Shih-Han, and church members like Emily, Hsieh-Ke, Past. Wu, Dr. Lin and Prof. Chen. My younger brother, Hsin-Wu, has also been my loyal supporter and I wish him the best for his study at the Univ. of Florida. Finally, I would like to dedicate this dissertation to my dear parents and family in Kaohsiung, Taiwan−it is their encouragements that gave me the initial motivation to study in the U.S. and their long-lasting supports that helped me persevere in despite of all the difficulties.

Yuan-Chieh Tseng

Northwestern University, June 2009

Table of Contents

ABSTRACT 3

Acknowledgements 5

List of Tables 10

List of Figures 11

Chapter 1. Introduction 15

1.1. Giant magnetocaloric effect and $Gd_5(Si_xGe_{1-x})_4$ compounds 15

1.2. The role of Si-doping in $Gd_5(Si_xGe_{1-x})_4$ 24

1.3. Volume effect in $Gd_5(Si_xGe_{1-x})_4$ 24

1.4. Motivation for high pressure study 25

Chapter 2. Introduction to synchrotron techniques 28

2.1. X-ray magnetic circular dichroism (XMCD) 28

2.2. X-ray absorption fine structure (XAFS) 38

2.3. X-ray powder diffraction (XRD) 42

Chapter 3. High pressure experimental setup 46

3.1. High-pressure XMCD beamline setup 46

3.2. Diamond anvil cell (DAC) 48

3.3. Sample preparation 50

3.4. Pressure calibration 50

Chapter 4. Role of Si-doping in enhancing ferromagnetic interactions in $Gd_5(Si_xGe_{1-x})_4$ compounds 57

4.1. Introduction 57

4.2. Experiment 58

4.3. Results for $Gd_5(Si_{0.125}Ge_{0.875})_4$ and $Gd_5(Si_{0.5}Ge_{0.5})_4$ compounds 59

4.4. Discussions for $Gd_5(Si_{0.125}Ge_{0.875})_4$ and $Gd_5(Si_{0.5}Ge_{0.5})_4$ 63

4.5. Results and discussions for $Gd_5(Si_{0.375}Ge_{0.625})_4$ 67

4.6. Conclusion 69

Chapter 5. Emergence of ferromagnetic order from within antiferromagnetic phase of Gd_5Ge_4: pressure studies of low-x region 70

5.1. Introduction 70

5.2. Experiment 71

5.3. Results 73

5.4. Discussion 79

5.5. Modified phase diagram of $Gd_5(Si_xGe_{1-x})_4$ 86

5.6. Conclusion 90

Chapter 6. Quantitative discrepancy between Si-doping and pressure effects upon $Gd_5(Si_xGe_{1-x})_4$ compounds 91

6.1. Introduction 91

6.2. Experiment 92

6.3. Results 94

6.4. Discussion 100

6.5. Conclusion 106

Chapter 7. Summary and future work 108

7.1. Thesis summary 108

7.2. Future work 110

References 114

Appendix A. Local structure analysis using IFEFFIT calculation 121

A.1. Introduction to IFEFFIT 121

A.2. Data analysis process 121

Appendix B. FDMNES calculations 127

B.1. Introduction 127

B.2. Program inputs 127

B.3. Examples 130

List of Tables

1.1	MCE of different materials	20
6.1	Si and Ge interatomic distance change determined by K -edge XAFS	103

List of Figures

1.1	Schematic illustration of magnetic refrigeration cycle	17
1.2	The entropy-temperature diagram of the MCE materials	18
1.3	Analogy between magnetic refrigeration and traditional vapor-compressed refrigeration	19
1.4	Crystal structures of $Gd_5(Si_xGe_{1-x})_4$	22
1.5	Phase diagram of $Gd_5(Si_xGe_{1-x})_4$	23
2.1	Schematic illustration of the circularly polarized x-ray induced electronic transition responsible for XMCD	29
2.2	helicity-dependent XAS and XMCD spectra	30
2.3	Temperature dependence of the coercive field (H_c) for ε-Fe_2O_3 nanoparticles	33
2.4	Temperature-dependence of m_{orb}, m_{spin} and m_{orb}/m_{spin} for ε-Fe_2O_3 nanoparticles	34
2.5	Schematic illustration of the vectorial-probe characteristic of XMCD	35
2.6	Magnetic-field dependence of out-of-plane XMCD signal for Mn and Ru in $SrRuO_3/SrMnO_3$ multilayer	36
2.7	Schematic illustration of the spin configuration of $SrRuO_3/SrMnO_3$ multilayer	37
2.8	Schematic illustration of a XAFS process	39

2.9	XAFS analysis process	41
2.10	Schematic illustration of the Bragg diffraction	42
2.11	Angle-dispersive powder diffraction setup	44
2.12	2-D diffraction image pattern and 2θ diffraction pattern of $Gd_5(Si_xGe_{1-x})_4$	45
3.1	Schematic illustration of the experimental high-pressure XMCD setup	47
3.2	Configuration of the diamond anvil cell, cold finger extension, and electromagnet	49
3.3	Cu XAFS pressure calibration	53
3.4	Pressure-dependent ruby R-line fluorescence spectra	55
3.5	Portable ruby fluorescence detector	56
4.1	Gd L_3 -edge XMCD signal as a function of temperature for P = 0.25 and 14.55 GPa for $Gd_5(Si_{0.125}Ge_{0.875})_4$	60
4.2	XMCD as a function of temperature for different applied pressures for $Gd_5(Si_{0.125}Ge_{0.875})_4$ and $Gd_5(Si_{0.5}Ge_{0.5})_4$	61
4.3	Magnetic phase diagram as a function of Si concentration and applied pressure	62
4.4	dT_c/dP comparison for $Gd_5(Si_{0.125}Ge_{0.875})_4$, $Gd_5(Si_{0.375}Ge_{0.625})_4$, and $Gd_5(Si_{0.5}Ge_{0.5})_4$; the P-T phase diagram of $Gd_5(Si_{0.375}Ge_{0.625})_4$	68
5.1	Lattice parameters and unit-cell volume of x-dependent $Gd_5(Si_xGe_{1-x})_4$	72
5.2	Temperature-dependent dc magnetization of $Gd_5(Si_xGe_{1-x})_4$	73

5.3 X-ray diffraction pattern of $Gd_5(Si_xGe_{1-x})_4$ at T = 17 K and Rietveld refinements 75

5.4 Gd L_3 -edge XMCD signal taken at P = 9.2 GPa for $Gd_5(Si_{0.025}Ge_{0.975})_4$ 76

5.5 Temperature-dependent Gd L_3 -edge XMCD for $Gd_5(Si_{0.025}Ge_{0.975})_4$, $Gd_5(Si_{0.05}Ge_{0.95})_4$, and $Gd_5(Si_{0.075}Ge_{0.925})_4$ at ambient condition 77

5.6 Temperature-dependent Gd L_3 -edge XMCD for $Gd_5(Si_{0.025}Ge_{0.975})_4$, $Gd_5(Si_{0.05}Ge_{0.95})_4$, and $Gd_5(Si_{0.075}Ge_{0.925})_4$ at various pressures 78

5.7 (a)Temperature-dependent saturation magnetization and (b) dT_c/dP for $Gd_5(Si_{0.025}Ge_{0.975})_4$, $Gd_5(Si_{0.05}Ge_{0.95})_4$, and $Gd_5(Si_{0.075}Ge_{0.925})_4$ 79

5.8 Modified magnetic phase diagram of $Gd_5(Si_xGe_{1-x})_4$ 88

5.9 Modified structural phase diagram of $Gd_5(Si_xGe_{1-x})_4$ 89

6.1 Comparison of XRD at selected pressure points for $Gd_5(Si_{0.125}Ge_{0.875})_4$ 95

6.2 XRD and Rietveld refinement for $Gd_5(Si_{0.125}Ge_{0.875})_4$ at P = 7 GPa 96

6.3 Pressure-dependence of three lattice constants from ambient to 8 GPa for $Gd_5(Si_{0.125}Ge_{0.875})_4$ 97

6.4 Lattice constant change and related volume change with pressure and Si-doping, and their corresponding T_cs for $Gd_5(Si_{0.125}Ge_{0.875})_4$ 99

6.5 Magnitude of Fourier transform (FT) of Ge and Si K -edge XAFS spectra 102

6.6 Si and Ge K -edge experimental and simulated XANES and XMCD for $Gd_5(Si_{0.125}Ge_{0.875})_4$ 104

6.7 Schematic illustration of the local contraction effect present in crystal lattice 105

6.8 Schematic illustration of FM percolation in $Gd_5(Si_xGe_{1-x})_4$ 106

A.1 Ge K -edge XAFS raw data with background removal and k -dependent spectrum 122

A.2 ARTEMIS interface with FEFF paths 123

A.3 FEFF fitting parameters 124

A.4 FEFF fitting results 125

A.5 k-dependent and the Fourier transform of Ge K -edge XAFS with FEFF fitting results 126

B.1 Basic codes for FDMNES calculation 128

B.2 Flow-chart for a complete FDMNES calculation process 129

B.3 Si K -edge XMCD and XANES spectra collected from FDMNES calculation 130

B.4 Ge K -edge XMCD and XANES using different convolution width in FDMNES calculation 131

CHAPTER 1

Introduction

1.1. Giant magnetocaloric effect and $Gd_5(Si_xGe_{1-x})_4$ compounds

Attention to environmental and energy issues has been on the rise in recent years, with people becoming aware that the earth's environment is gradually destroyed and the limited energy resources are being over consumed by human activities. Global warming is considered one of the most severe, requiring prompt strategies. Our current vapor-compressed refrigerant technology is inefficient in electricity consumption, and its usage of chlorine-based refrigerant results in fairly high greenhouse gas emission and ozone layer depletion which are responsible for the global warming effect. To circumvent this, an alternative concept using solid state materials as refrigerant was created. The key principle behind this concept is the magnetocaloric effect (MCE)[**1**], where it harnesses the degree of ordering of nuclear or electronic magnetic dipoles in order to reduce a material's temperature and allow the material to serve as a refrigerant (Fig. 1.1)[**2**]. This phenomenon was originally discovered in iron by Warburg[**1**] and explained independently by Debye [**3**]and Giauque [**4**]. The cooling capability of the MCE is reflected by the magnetic entropy (ΔS_M) and the adiabatic temperature (ΔT_{ad}) change upon applied magnetic field, and these two parameters can be expressed as:

$$\Delta S_M(T, \triangle H) = \int_{H_1}^{H_2} (\frac{\partial M(T,H)}{\partial T})_H dH \tag{1.1}$$

$$\Delta T_{ad}(T, \triangle H) = -\int_{H_1}^{H_2} (\frac{T}{C(T,H)})_H (\frac{\partial M(T,H)}{\partial T})_H dH \tag{1.2}$$

M, C and H represent the magnetization, the heat capacity of the material and the applied magnetic field, respectively. The thermodynamics of the MCE in terms of ΔS_M and ΔT_{ad} is illustrated in Fig. 1.2 [**5**].The analogy between a vapor-compressed and a magnetic refrigerant is illustrated in Fig. 1.3 [**6**]. Conceptually, without emitting greenhouse gas and free of ozone-depleting refrigerant, the magnetic refrigeration can perform as a more environmentally-friendly counterpart. The MCE concept has been practical at very low temperature [**5**], but in order to improve magnetic refrigeration technology to the household near room temperature refrigeration based on the MCE is imperatively necessary.

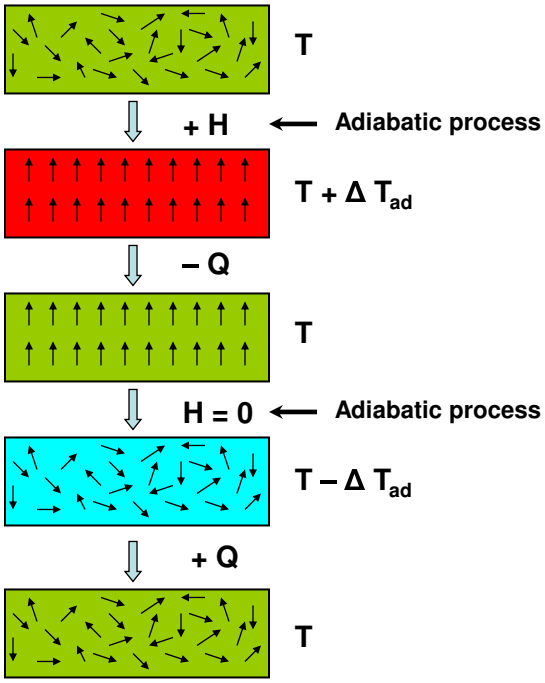

Figure 1.1. Schematic illustration of magnetic refrigeration cycle. The MCE material is placed in an isolated environment (adiabatic condition). When a magnetic field (H) is applied, the magnetic dipoles are aligned. Since the process is adiabatic, the magnetic entropy is not reduced yet, thereby increasing the temperature of the MCE material (T+ΔT). The added heat can be removed by coolant such as fluid or gas (-Q), while H is still held to prevent magnetic dipoles from re-absorbing the heat. Once the heat is removed, the MCE material undergoes an adiabatic process again to retain total entropy but H is decreased. The thermal energy will cause magnetic dipoles to overcome H, hence reducing the temperature of the material (T-ΔT). At this moment, the MCE material will be contacted with the substance wanted to be refrigerated. Because the MCE material is cooler than the substance, the heat will be transferred to the MCE material (+Q) finally to achieve the cooling purpose. Figure is reproduced from Ref. [**2**]

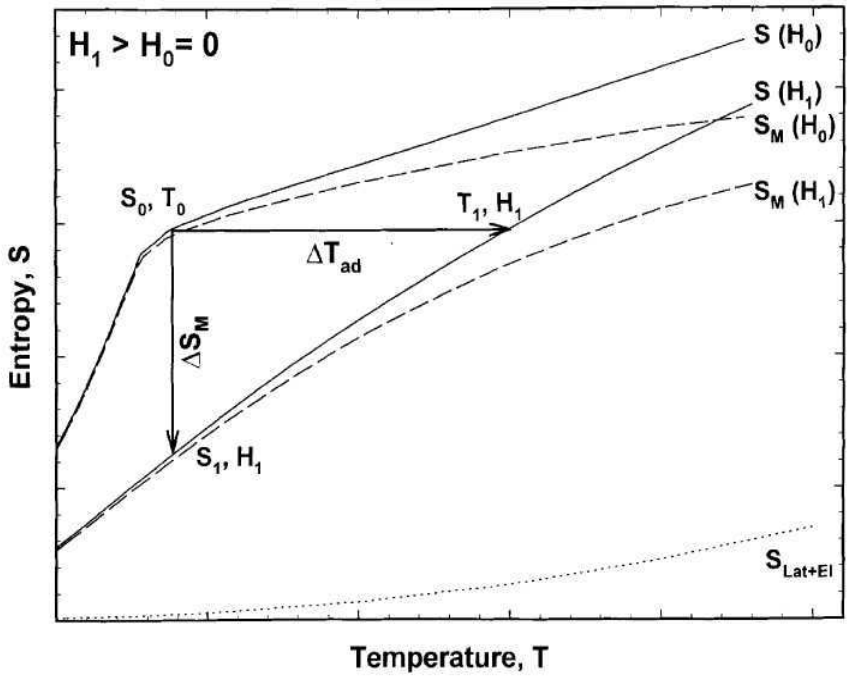

Figure 1.2. The entropy-temperature diagram taken from Ref. [**5**] illustrates the magnetocaloric effect. S_0, T_0 represent the entropy and temperature status without applied field, and S_1 and T_1 represent those with applied filed. The solid lines represent the total entropy change with ($S(H_1)$) and without ($S(H_0)$) applied field. The dotted line represent the electronic and lattice (non-magnetic) entropy change, and the dashed lines represent the magnetic entropy change with ($S_M(H_1)$) and without ($S_M(H_0)$) applied field. The horizontal arrow and vertical arrow represent the change of ΔT_{ad} and ΔS_M with applied field, respectively.

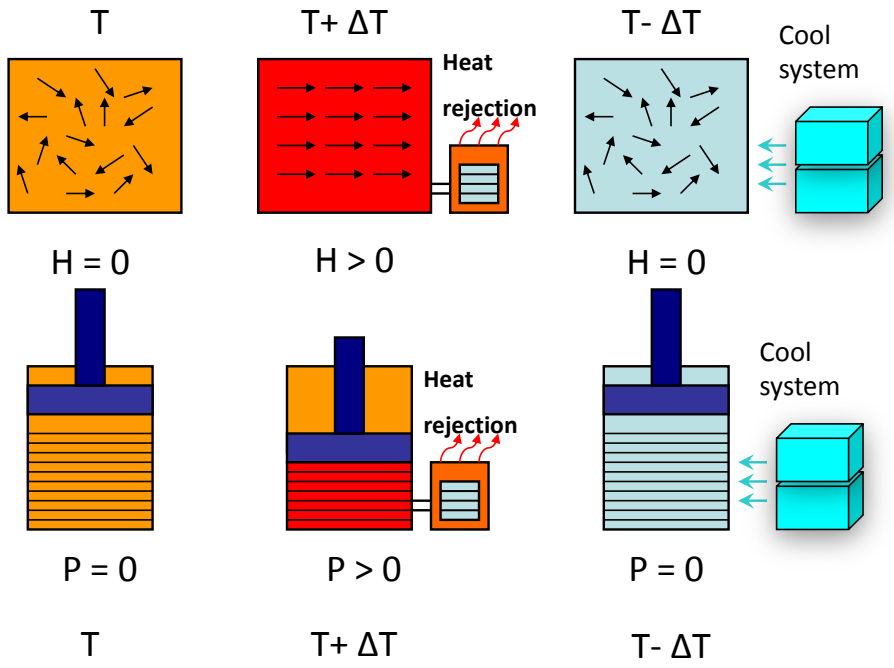

Figure 1.3. Analogy between magnetic refrigeration and traditional vapor-compressed refrigeration. In principle, the thermodynamic cycle used in magnetic refrigeration can replace the Carnot cycle used in traditional refrigeration for it performs better efficiency ($\sim$ 30 to 60 % of the Carnot cycle depending on applied field [**1**]) and is free to ozone-depleting coolants. Figure is reproduced from Ref. [**6**].

Material	T_c(K)	ΔH(T)	ΔS(J/kgK)	ΔT_{ad}(K)	Reference
$La(Fe_xSi_{1-x})H$	274−291	2−5	-24−-28	7−13	[7-9]
$Mn(As_xSb_{1-x})$	230−318	2−5	-18−-32	4.7−13	[10,11]
$La(Ca,Sr)MnO_3$	230−263	1.5−5	-3.8−8	< 3	[12,13]
$Gd_5(Si_xGe_{1-x})_4$	80−275	2−5	-14−-19	12−16	[14,15]
$Tb_5(Si_xGe_{1-x})_4$	50−110	5	-20	-	[16]
$Dy_5(Si_xGe_{1-x})_4$	~ 65	5	-34	-	[17]

Table 1.1. Entropy change, ΔS_M and adiabatic temperature change, ΔT_{ad}, occurring at the transition temperature T_c at different applied filed increase, ΔH, for materials displaying the giant MCE.

There has been several compounds displaying near or above room temperature MCE reported in recent studies. These include the series of La(Fe, Si)H [**7, 8, 9**], Mn(As, Sb) [**10, 11**], $La(Ca, Sr)MnO_3$ [**12, 13**], and $R_5(Si, Ge)_4$ [**14-17**]. Their MCE parameters (ΔS_M, ΔT_{ad}) and Curie temperatures (T_c) are present in Table 1. Among all candidate magnetocaloric materials, $R_5(Si_xGe_{1-x})_4$ where R is a rare earth (Gd, Tb, Dy) has drawn much attention due to its very strong coupling between structural and magnetic properties, leading to a giant MCE and making itself a competitive candidate. The intriguing crystal structures, composed of Gd containing slabs, together with the magnetic coupling mechanisms within and between the slabs, have been the subject of intense research. The phase transitions obtained in these materials usually involve change of crystal structure, such as breaking or forming of inter-slab Si(Ge) covalent bonds (Fig. 1.4) [**6**]. If the structural change occurs concomitantly with a magnetic transition, it results in a 1^{st} order magneto-structural transition. In such case, the change in structural entropy is added to the magnetic entropy change and the MCE of the material is greatly enhanced. $Gd_5(Si_xGe_{1-x})_4$ is renowned for its sizable MCE which could result in adiabatic temperature changes as high as 16 K [**13, 18, 19**]. More importantly, its 1^{st} order magneto-structural transition responsible for

the giant MCE can be tuned to reach $\sim$ 275 K, displaying great potential for room temperature (R.T.) operation of a magnetic refrigerant [**18-23**].

The building blocks of the crystal structure of $Gd_5(Si_xGe_{1-x})_4$ are the atomic-slabs shown in Fig. 1.4. The slabs contain three inequivalent crystallographic sites for Gd ions and two for Si(Ge) (T_2 and T_3, 25 % occupancy for each). The third crystallographic site for Si(Ge) is located between slabs (T_1, 50 % occupancy). This particular site is key because it effectively controls the degree of atomic-interactions between slabs, as well as playing a key role in modifying the crystal structures and magnetic properties [**14, 19**]. Figure 1.5 [**6**] shows the magnetism- and structure- related phase diagram of $Gd_5(Si_xGe_{1-x})_4$. There are three extended substitutional solid solutions in the phase diagram. First is with Gd_5Si_4 type structure ($0.5 < x \leq 1.0$) where the material's paramagnetic phase (PM) exhibits fully connected Si(Ge) covalent bonds, orthorhombic I (O(I)) structure. Second is with $Gd_5Si_2Ge_2$ type structure ($0.24 \leq x \leq 0.5$) where only half of Si(Ge) covalent bonds are present at monoclinic (M), PM phase. The third is with Gd_5Ge_4 type structure ($0 \leq x \leq 0.2$), and the material's PM phase displays an orthorhombic II (O(II)) structure with broken Si(Ge) covalent bonds. Interestingly, the material displays x-independent ($0 < x \leq 1.0$), Si(Ge) bond-connected O(I) structure for ferromagnetic (FM) state. In addition, an O(II), antiferromagnetic (AFM) intermediate phase is only present for $0 \leq x \leq 0.2$.

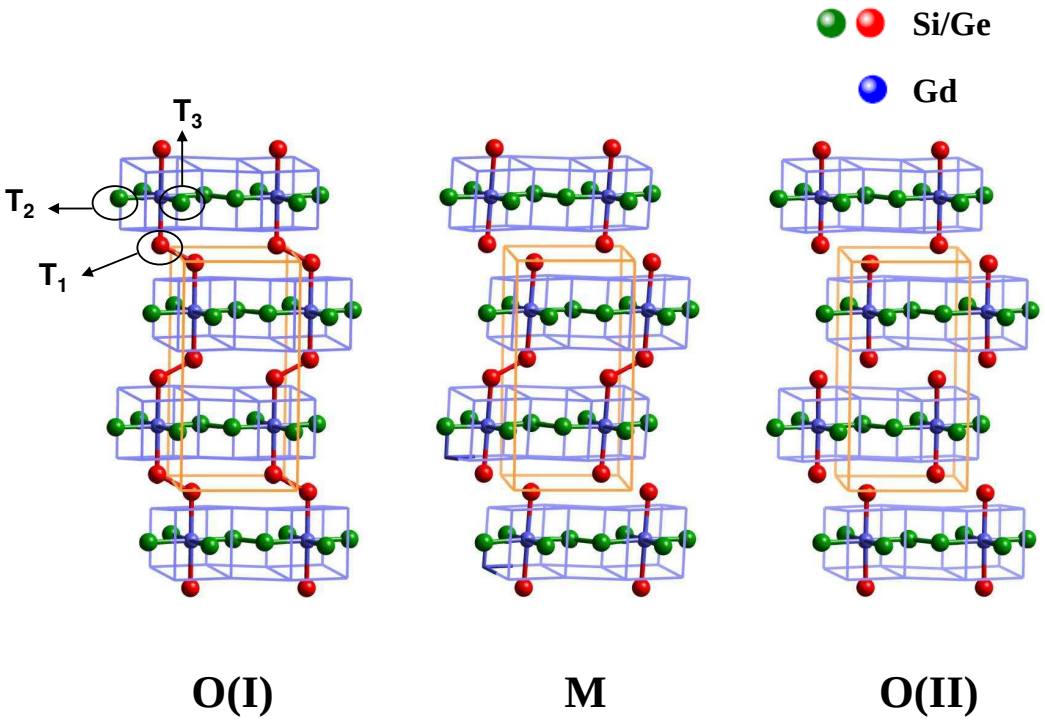

Figure 1.4. Crystal structures for $Gd_5(Si_xGe_{1-x})_4$ compounds. All Gd ions are located inside the slabs, while Si(Ge) can occupy either inter-slab (T_1) or intra-slab (T_2, T_3) crystallographic sites. O(I), M and O(II) represent orthorhombic (I), monoclinic and orthorhombic (II), respectively. The presence or absence of covalent Si(Ge) bonds between the slabs is what distinguishes between the various structures. Figure is reproduced from Ref. [**6**].

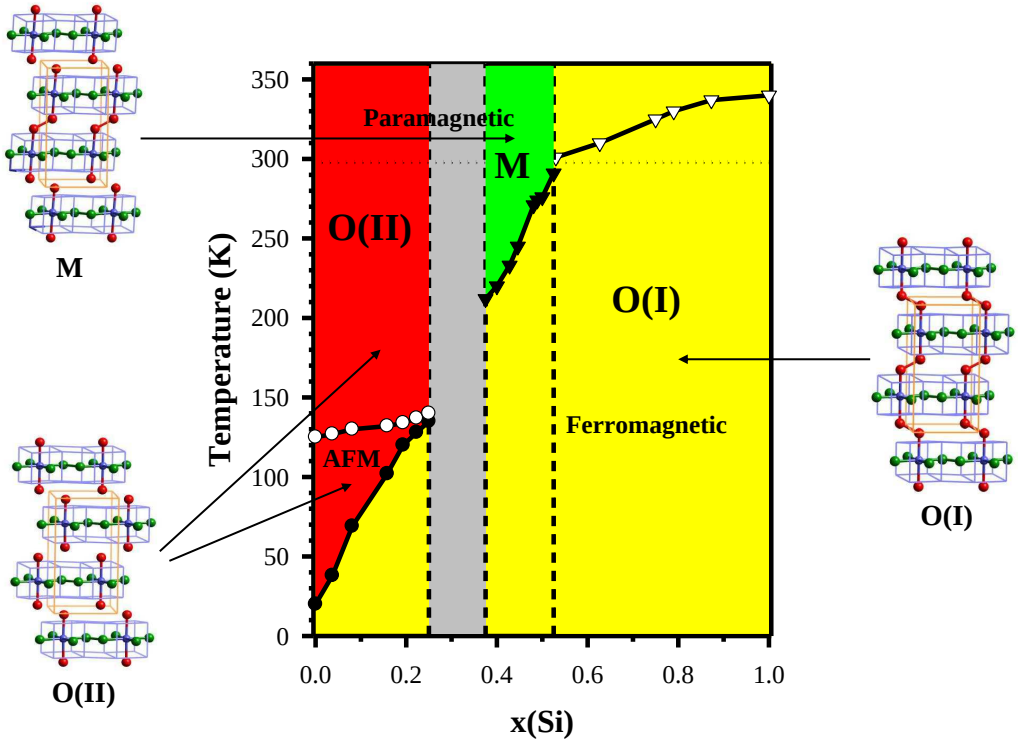

Figure 1.5. Phase diagram of $Gd_5(Si_xGe_{1-x})_4$. Different crystal structures are thereby illustrated for different magnetic phases – O(II) for AFM and P in low x region ($0 \leq x \leq 0.2$), M for PM in the middle of region ($0.24 \leq x \leq 0.5$), and O(I) for all FM ($0 < x \leq 1.0$) but for PM only in high x region ($0.5 < x \leq 1.0$). Figure is reproduced from Ref. [**6**].

1.2. The role of Si-doping in $Gd_5(Si_xGe_{1-x})_4$

A valuable feature of $Gd_5(Si_xGe_{1-x})_4$ is that T_c can be linearly increased by Si-doping, as shown in Fig. 1.5. In particular, the ordering temperature is tunable from $\sim$ 30 to $\sim$ 275 K ($0 < x \leq 0.5$) by adjusting the Si/Ge ratio without losing the giant MCE [**25**]. This expands the operational temperature range of magnetic refrigeration based on this compound. However, this striking feature disappears when the Si-content is larger than $x = 0.5$, where a purely, 2^{nd} order FM(O(I)) $\rightarrow$ PM(O(I)) transition takes place on warming ($0.5 < x \leq 1.0$) without a concomitant structural change, as also shown in Fig. 1.5 [**18, 20**]. This limits the usage of this material as a magnetic refrigerant for applications below 275 K. Thus, in order to extend the giant MCE towards R.T. in these and related materials, understanding the role of Si-doping has become an important goal. Most of the relevant studies focused on certain interesting compositions ($x = 0$, 0.125, 0.5), sporadically exploring the fundamental knowledge of their magnetic and structural properties and MCEs [**19, 20, 26, 27**]. Nevertheless, a systematic effort aimed at unveiling the mechanism by which Si enhances T_c is missing. This effort is essential as it will shed light into possible routes to achieve higher ordering temperature for the giant MCE materials, critically needed for true R.T. magnetic refrigeration based on these and related compounds.

1.3. Volume effect in $Gd_5(Si_xGe_{1-x})_4$

Having smaller atomic size than Ge, Si's role in occupying three inequivalent crystallographic sites (Fig. 1.4) is to exert chemical pressure upon the lattice causing a reduction in unit cell volume. This volume reduction directly enhances both intra- and inter-slab magnetic interactions, resulting in an increase of the FM ordering temperature. In particular, the volume reduction

also leads to the reforming of inter-slab bonds, converting either O(II) or M into O(I) structure which favors the FM phase [**6, 10, 16**].

The macroscopic volume-effect obtained with atomic substitution suggests that it itself ought to be the dominant course in modifying the material's properties. Until now, a few pressure studies were carried out to verify this hypothesis. Morellon et al. [**28**] reported that these compounds exhibit a pressure-induced increase of the ordering temperature $dT_c/dP = 0.3$ and 3.0 K kbar^{-1} for $x = 0.8$ and $0 \leq x \leq 0.5$, respectively. Another work by the same authors shows that pressure can convert Gd_5Ge_4 AFM-O(II) into FM-O(I) phase with $dT_c/dP = 4.8$ K kbar^{-1} by reforming the inter-slab bonds [**29**]. Mudryk et al. [**26**] found that a M $\rightarrow$ O(I) structural transition can be induced by applying pressures of $\sim$ 2.2 GPa in an $x = 0.5$ sample. These preliminary findings indicate that pressure does stabilize the FM phase by converting the structure from larger volume (O(II) or M) into smaller one (O(I)), similar to the effect of Si-doping. Despite these findings, whether the magnetic/structural transitions are driven *solely* by macroscopic volume effects is unclear, i.e. whether Si-doping in $Gd_5(Si_xGe_{1-x})_4$ simply reduces the macroscopic volume and hence an equivalent effect is obtained with applied pressure.

1.4. Motivation for high pressure study

One common aspect of all previous pressure studies is their limitation to the low pressure range. Extending this work to higher pressures is critical to unveil the correspondence between Si-doping and pressure. Most pressure- and magnetism- related research in $Gd_5(Si_xGe_{1-x})_4$ was done using the strain-gauge technique in a piston-cylinder, which can only provide pressures up to 1 GPa (10 kbar) [**28, 29**]. To date, the highest pressure applied to $Gd_5(Si_xGe_{1-x})_4$ was 2.5 GPa [**26**]. This limitation restricts the correspondence study to a very narrow range and thus

leaves key questions unsolved. Besides, the low-x region ($0 \leq x \leq 0.2$; Fig. 1.5) displays an AFM intermediate phase with low saturation magnetization, which is not present at higher Si content. The mechanism that leads to the emergence of the FM order from Gd_5Ge_4 with pure AFM ground state is unclear. In particular, the truth that whether the low-x region should be described as a frustrated magnet with competing FM and AFM interactions, or a magneto-structural mixed phase AFM(O(II))-FM(O(I)), hasn't been examined. A pressure study combined with x-ray powder diffraction at ambient condition could solve these questions which are not fully addressed in Ref. [**29**] also due to pressure limitation. The magnetic properties measurements of previous pressure-studies were primarily carried out in superconducting quantum interference device (SQUID). The SQUID has very limited space for sample loading, and can't avoid detecting the paramagnetic or diamagnetic backgrounds usually displayed by most of the matters. These factors limit the usage of certain pressure cells that can yield higher pressures.

In order to unambiguously determine the correlation between Si-doping and pressure, high-pressure (HP) studies (up to $\sim$ 20 GPa) were conducted on $Gd_5(Si_xGe_{1-x})_4$ in this work. The work was carried out by combining synchrotron techniques with a setup especially dedicated to HP studies, where a diamond anvil cell (DAC) was incorporated. This combined technique provides a better way to isolate the effects of volume reduction upon the magnetic/structural transitions by ruling out doping-induced effects, such as (a) nonrandom distribution of Si(Ge) among the three inequivalent sites [**30**], (b) volume-independent modifications to the electronic structure due to differences in Ge $4p$ and Si $3p$ wave functions, and (c) phase separation or spatially-inhomogeneous distribution of Si dopants depending on the conditions of the material's synthesis [**31**]. Within this approach, the correspondence between Si-doping and pressure was investigated both qualitatively and quantitatively. Especially, we carried out the HP magnetic

properties measurements using x-ray magnetic circular dichroism (XMCD) which is renowned for probing element-specific magnetism (described in Chapter 2). This work basically covers pressure studies for most of the interesting regions of the phase diagram, including Ge-rich ($0 < x < 0.1$) and middle ($0.125 \leq x \leq 0.5$) regions. Two specific compositions ($x = 0.125$ and 0.5) were chosen to do quantitative investigations.

The dissertation is organized as follows. Chapter 1 is the introduction. Chapter 2 provides the introduction of the synchrotron techniques used in this work. Chapter 3 describes the experimental setup of HP. Chapter 4 contains pressure studies for the middle region ($0.125 \leq x \leq 0.5$), and Chapter 5 for Ge-rich ($0 < x < 0.1$) region. Chapter 6 discusses quantitatively, the correspondence between Si-doping and pressure. Thesis summary and future work are presented in Chapter 7.

CHAPTER 2

Introduction to synchrotron techniques

2.1. X-ray magnetic circular dichroism (XMCD)

XMCD is a spectroscopic technique especially suitable to probing ferromagnetism, or materials with non-zero net magnetization such as ferrimagnetism or canted antiferromagnetism. XMCD measurements require circularly polarized x-rays usually generated by specialized insertion devices [**32, 33**] or phase retarding optics [**34**] adopted in third-generation synchrotron facilities. The circularly polarized x-ray is helicity-dependent, carrying right- and left- circularly polarized photons. X-ray absorption process involves excitation of a core electron to unoccupied electronic states. When a helicity-dependent photon comes in, it carries angular moment along its propagation direction, and this projection of the angular momentum is then transferred to spin-polarization of the excited electrons through a spin-orbit coupling. As shown in Fig. 2.1, the right- and left- circularly polarized photons would generate spin-down and -up photoelectrons, respectively. Since ferro- (ferri) magnetic or canted antiferromagnetic materials have imbalanced density of states of spin-up and spin-down, this imbalance gives rise to the difference in absorption coefficients for the opposite x-ray helicities, which is the XMCD signal.

When circularly polarized x-ray passes through a magnetic material of thickness of d, the intensity of the two polarization states, indicated as $+$ and $-$ are:

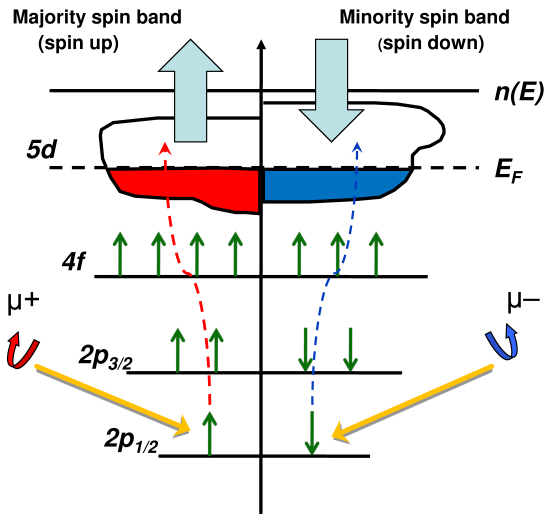

Figure 2.1. Schematic illustration of the circularly polarized x-ray induced electronic transition responsible for XMCD. The transition corresponds to the L_3 ($2p_{1/2}$) absorption edge of Gd (half-filled $4f$ orbital). The $5d$ band probed by this transition is split into spin-up and spin-down states by intra-atomic $4f$-$5d$ exchange interactions.

$$I_1^+(E) = I_0^+(E)e^{-\mu^+(E)d}\,;\; I_1^-(E) = I_0^-(E)e^{-\mu^-(E)d} \tag{2.1}$$

where μ^+ and μ^- are absorption coefficients for opposite x-ray helicities, and the absorption coefficient, taking μ^+ as an example, can be derived from the measured intensity by:

$$\mu^+(E) = (\frac{1}{d})\ln(\frac{I_0^+(E)}{I_1^+(E)}) \tag{2.2}$$

And XMCD signal is expressed by:

$$XMCD = \mu^+ - \mu^- \tag{2.3}$$

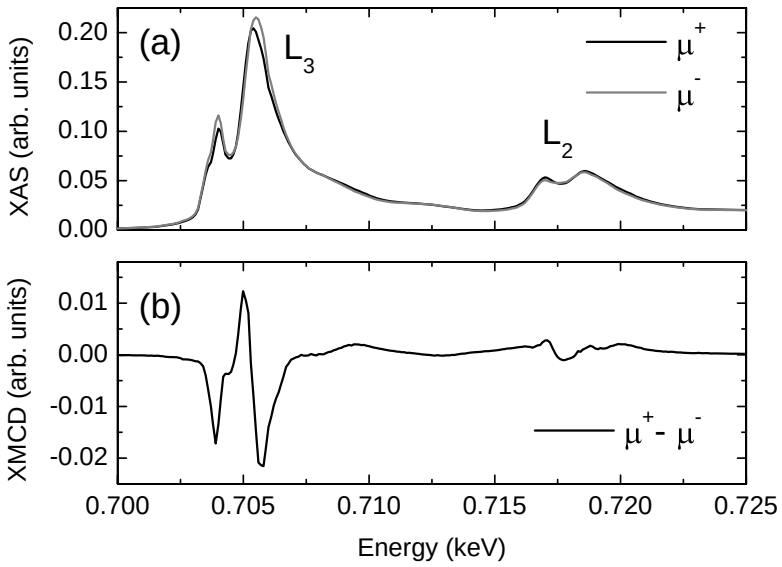

Figure 2.2. (a) helicity-dependent (μ^+ and μ^-) x-ray absorption spectra (XAS) and (b) XMCD (μ^+-μ^-) of L_2 and L_3 absorption edges for Fe^{+3} ions collected from ε-Fe_2O_3 [**50**] samples.

The correlation between helicity-dependent absorption and XMCD spectra is illustrated in Fig. 2.2. XMCD has a major impact on understanding the element-specific physics of ferromagnetic materials. By tuning the x-ray energy to selected atomic resonances, the measurements can yield element- and orbital- selective magnetization [**35**].

Materials having ferromagnetic ordering are transition metals, rare earths and their alloys. For transition metals (Ni, Co, Fe), their ferromagnetism is originated from unfilled $3d$ shells. For rare earths, Gd or Tb for example, their ferromagnetic ordering is attributed to unpaired electrons in unfilled $5d$ and localized $4f$ shells [**36**]. In rare earths, the $4f$ electron wave functions are highly localized, and their ferromagnetic ordering is interpreted as the indirect exchange between $4f$ electrons through the spin-polarized $5d$ ($6s$) conduction bands [**36**]. Unlike rare earths, transition metals possess ferromagnetic ordering based on the direct exchange between

$3d$ electrons. Thus, larger dichroic effects can be obtained at $L_{2,3}$ -edges ($2p \rightarrow 3d$) and $M_{4,5}$ -edges ($3d \rightarrow 4f$) in transition metals due to direct probe of $3d$ shell. Although probes of $L_{2,3}$ -edges ($2p \rightarrow 5d$) in rare earth also directly monitor the spin-polarization of the $5d$ shell, this shell carries relatively smaller polarization that is induced by $4f$ shell. In this work, L_3 -edge of Gd was chosen because the XMCD signal at this particular energy can be detected in a diamond anvil cell (DAC, described in Chapter 3).

The element- and orbital- selective advantages of XMCD are used in many areas ranging from fundamental to applied aspects, such as magneto-electronics [**37-40**], earth sciences [**41, 42**] and life sciences [**43, 44**]. In this work, XMCD was used at the Gd L_3 -edge to probe $5d$ polarization, which is proportional to $4f$ polarization and represents the magnetic properties of $Gd_5(Si_xGe_{1-x})_4$. Si(Ge) K -edge ($1s \rightarrow 3(4)p$) was also probed to understand how p states mediate the FM interactions within the compounds. Although neutron diffraction is also capable of probing magnetic structure, it was not used in this study because neutron diffraction requires large sample size, which is not suitable for diamond anvil cell.

2.1.1. Sum rules calculations of XMCD

In addition to element- and orbital- selectivity, XMCD is also renowned for being capable of decomposing spin (m_{spin}) and orbital (m_{orb}) contributions to total magnetic moment. The separation of m_{spin} and m_{orb} is invaluable for understanding the fundamental origins of the macroscopic magnetic properties of the matter. The decomposing process involves sum rule calculations [**45-47**]. In the following, an example from the side-project of this thesis is given to highlight this strength.

Example: **magneto-crystalline anisotropic change in ε-Fe_2O_3 magnetic nanoparticles**

ε-Fe_2O_3 magnetic nanoparticles exhibiting a large coercivity field (H_c) of 20 kOe at room temperature and bearing the characteristic of easy synthesis make it a potential candidate for magnetic storage applications [**48, 49**]. However, a large reduction of H_c with temperature decrease is obtained in this material, with a H_c of 0.8 kOe found at $\sim$ 110K (Fig. 2.3). XMCD measurements were carried out and analyzed within the framework of sum rules to unveil this magnetic softening characteristic. Details of sum rule calculations can be found in Ref. [**47**]. The $3d$ electron occupation number needed for a quantitative derivation of orbital and spin components of magnetization, was set to $n_{3d} = 5$ based on the $3d^5$ electronic configuration of Fe^{+3} ions. The temperature-dependent m_{spin}, m_{orb}, and m_{orb}/m_{spin} quantities obtained from the sum rule calculations are shown in Fig. 2.4.

The results show that m_{spin} remains largely temperature independent while m_{orb} shows a significant decrease around 120 K. In particular, the m_{orb}/m_{spin} ratio, which is independent of both the $3d$ electron configuration and the integration of XAS data, shows a significant reduction (> 50 %) of the Fe $3d$ orbital moment at T $\sim$ 120 K and subsequently increases to attain at 80 K a value of the same order than the one measured at 200 K. It is argued [**50**] that the large m_{orb} at room temperature is the origin of the moderately large anisotropy found in the material, where the large reduction in m_{orb} at 120 K, and the related weakening of spin-orbital coupling, is responsible for the decrease of the H_c around 110 K.

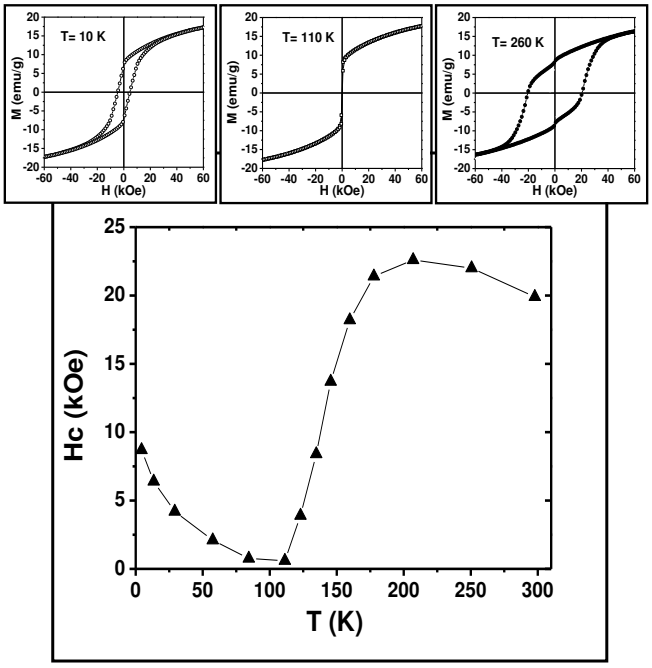

Figure 2.3. Temperature dependence of the coercive field (H_c) for ε-Fe_2O_3 nanoparticles taken from [**49**]. The upper insets show the magnetization vs. magnetic field hysteresis loops of ε-Fe_2O_3 nanoparticles measured at 10 K, 110 K and 260 K, respectively

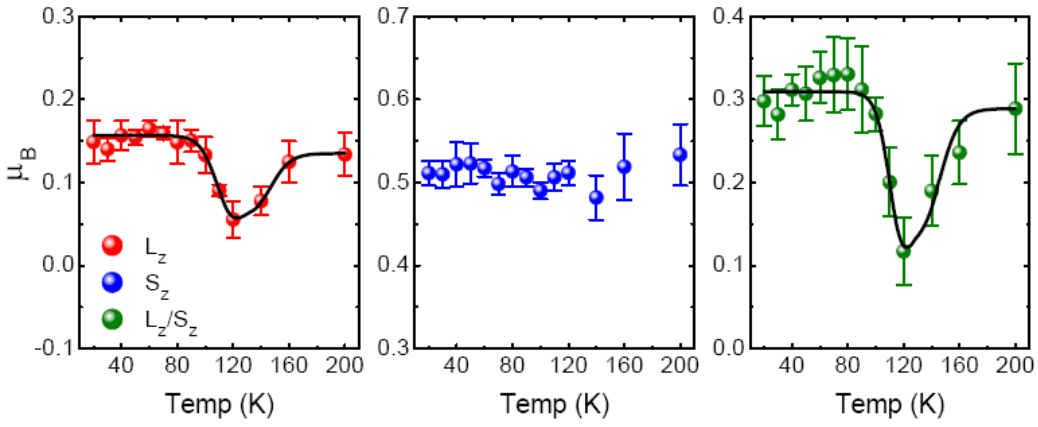

Figure 2.4. Temperature-dependence of the orbital (m_{orb}) and spin (m_{spin}) effective moments and the ratio of orbital/spin (m_{orb}/m_{spin}) for ε-Fe_2O_3 nanoparticles.

2.1.2. Vectorial characteristics of XMCD

It is also important to note that XMCD is a vectorial probe of magnetism. Since the photo-electron is spin-polarized along or opposite the x-ray helicity, i.e., x-ray propagation direction, the XMCD signal depends on the relative alignment of the x-ray wave-vector and the quantization axis determined by an applied magnetic field, , where is the local moment direction (Fig. 2.5). Since the x-ray absorption process averages over many absorbing sites, the vectorial nature of XMCD implies that an element-specific magnetization is required to yield a XMCD signal $\langle \vec{K} \cdot \vec{M} \neq 0 \rangle$. This allows XMCD to probe the net projection of moment aligned along the direction of photon wave-vector.

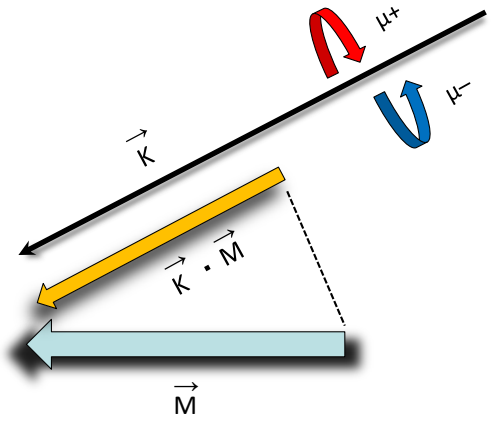

Figure 2.5. Schematic illustration of the vectorial-probe characteristic of XMCD. $\vec{K}$ represents the x-ray photon wave-vector with helicity-dependency and $\vec{M}$ represents the real magnetic moment. $\vec{K}\cdot\vec{M}$ is the effective magnetic moment probed by XMCD.

Example: **interfacial magnetism in** $SrRuO_3/SrMnO_3$ **multilayer system**

A multilayer system composed of perovskite $SrRuO_3$ (SRO) and $SrMnO_3$ (SMO) thin films was investigated. SRO is a ferromagnet with T_c of $\sim$ 163 K [**51**] and strong out-of-plane anisotropy. SMO is a G-type antiferromagnet with a Néel temperature (T_N) of $\sim$ 260 K [**52**]. XMCD measurements were carried out with the magnetic field applied parallel to the x-ray propagation direction, which is along the film normal [**53, 54**]. Since XMCD is proportional to the net magnetic moment of resonant atoms projected along the x-ray propagation direction, it can be seen in Fig. 2.6(a) that despite the AFM characteristic of SMO layer, the Mn ions possess a net out-of-plane ferromagnetic moment with applied field (H) of 10 kOe at 50 K. However, as the field increases to 40 kOe, the XMCD signal vanishes. This suggests that either the net Mn moment disappears or rotates to the direction orthogonal to photon wave-vector, or could be

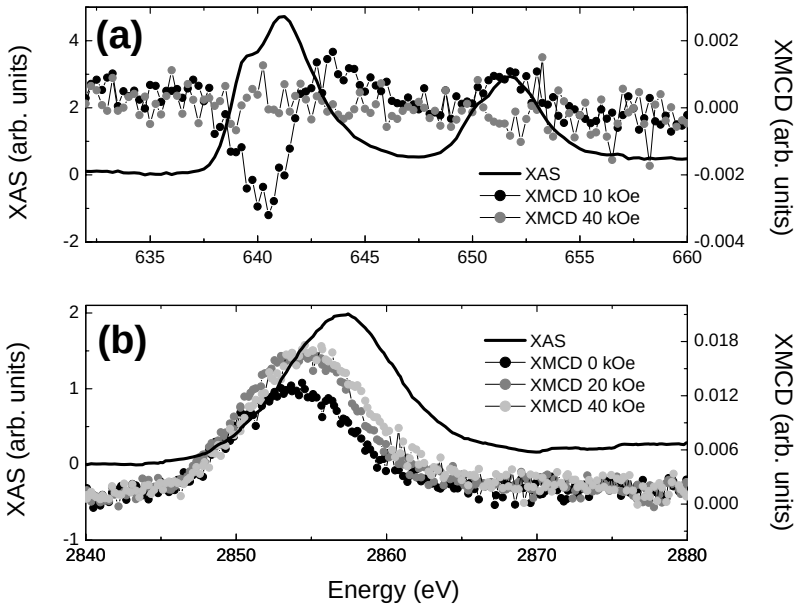

Figure 2.6. Magnetic-field dependence (in kOe) of out-of-plane XMCD signals for (a) Mn L_2, L_3 -edges and (b) Ru L_2 -edge at 50K. Ru L_3 -edge was not probed due to energy-range limitation at the beamline 4-ID-C, the Advanced Photon Source.

both. The field-dependence of Ru moment at the same temperature is shown in Fig. 2.6(b). As expected, a large out-of-plane Ru moment is observed. The remanent Ru moment obtained at H = 0 is $\sim$ 70 % of that obtained at H = 40 kOe by comparing the XMCD signal, suggesting that it results from the strong out-of-plane anisotropy of SRO layer. The reverse sign of XMCD between Mn and Ru moment upon field-dependence suggests an antiferromagnetic (AFM) coupling between SRO and SMO layers, as shown in Fig. 2.7.

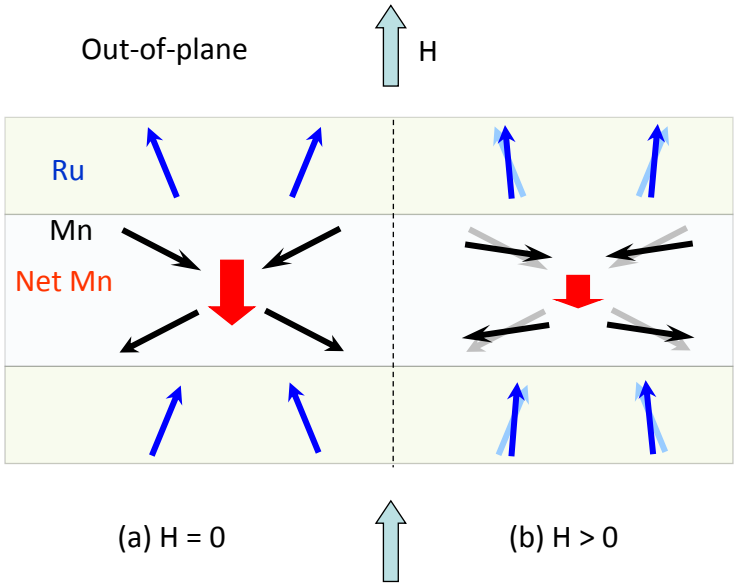

Figure 2.7. Schematic illustration of the spin configuration of SRO/SMO multilayer system with and without an out-of-plane applied field.

2.2. X-ray absorption fine structure (XAFS)

X-ray absorption fine structure (XAFS) is a powerful technique for studying local structure in both ordered and disordered materials [**55**]. The spectroscopy acquires the energy range near and above the core-level binding energy of the selected atom. XAFS can probe chemical and physical states, sensitive to the coordination number, bonding distances surrounding around the selected atoms. Fig. 2.8(a) is the sketch of XAFS process. An x-ray photon comes in and is absorbed by the selected atom [**56**]. The absorption process liberates the core-level electron, generating the outgoing photoelectron. The outgoing photoelectron leaves the absorbing atom with a spherical wave until it hits the electron-cloud of the neighboring atoms. Hence, the photoelectron is scattered by the neighboring atom and goes back to the absorbing atom. The interference between the outgoing and back scattered wave-functions results in a modulation of x-ray absorption coefficient, giving rise to the XAFS (Fig. 2.8(b)).

For XAFS, the interest is in the oscillations above the absorption edge, and define the XAFS fine structure function $\chi(E)$ as:

$$\chi(E) = \frac{\mu(E) - \mu^{\circ}(E)}{\mu^{\circ}(E)} \tag{2.4}$$

Here $\mu^{\circ}(E)$ is the absorption coefficient of an isolated atom, and $\mu(E)$ is the absorption coefficient of the atom in the material of interest. χ(E) can be further expressed as a function of photoelectron wave number, k, which has dimensions of 1/distance. Energy and wave number are related by:

$$k = \sqrt{\frac{2m(E - E^{\circ})}{\hbar^2}} \tag{2.5}$$

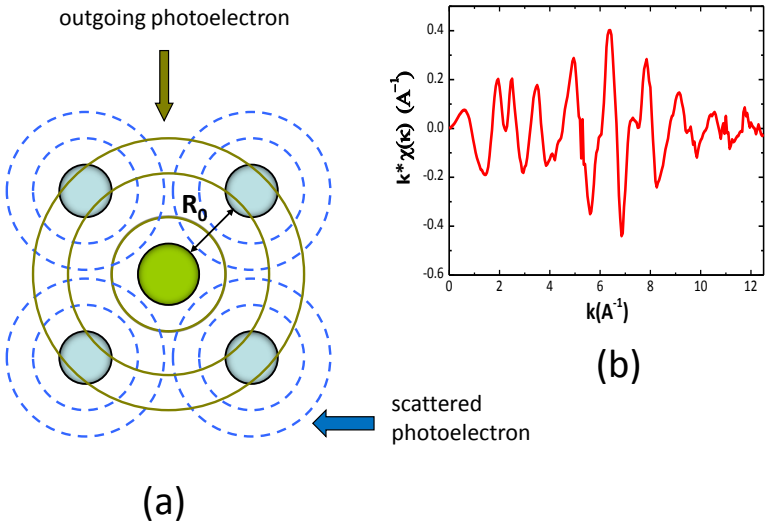

Figure 2.8. (a) Schematic of a XAFS process, in which the wave-function of outgoing and back scattered photoelectrons interfere to each other to form the XAFS signal. (b)The XAFS can be expressed in k, photoelectron wave number, in which the oscillations reflect the interference of wave-function. Figure is reproduced from Ref. [**56**].

where E° is the absorption edge energy, E is the photon energy, $E - E^\circ$ is the kinetic energy of the photoelectron, and m is the electron mass. In this way, the primary quantity for XAFS is then $\chi(k)$, which can be written as:

$$\chi(k) = \sum_j \frac{N_j e^{-2k^2\sigma_j^2} e^{-2R_j/\lambda(k)} f_j(k)}{kR_j^2} \sin[2kR_j + \delta_j(k)] \tag{2.6}$$

where $f(k)$ and $\delta(k)$ are scattering amplitude and phase, N is the number of neighboring atoms, R is the distance to the neighboring atom, $\lambda(k)$ is the mean-free-path of the photoelectron, and σ^2 is the disorder in the neighbor distance. The typical way to process the XAFS data is as follows

- Convert measured intensities to $\mu(E)$, and subtract a smooth pre-edge background from $\mu(E)$ to get rid of absorption from other edges.
- Identify the threshold energy E°, and normalize $\mu(E)$ to go from 0 to 1, so that it represents the absorption of one atom.
- Remove a smooth post-edge background function to approximate $\mu^{\circ}(E)$.
- k-weight the XAFS $\chi(k)$ and Fourier transform into real space.

A typical XAFS analysis process is shown in Fig. 2.9 [**57**]. By comparing with theoretical calculations, the XAFS data can be analyzed to obtain the local structure around the selected element. In this work, XAFS was used to probe local contraction effect around Si atoms (Chapter 6) and to calibrate pressure (Chapter 3).

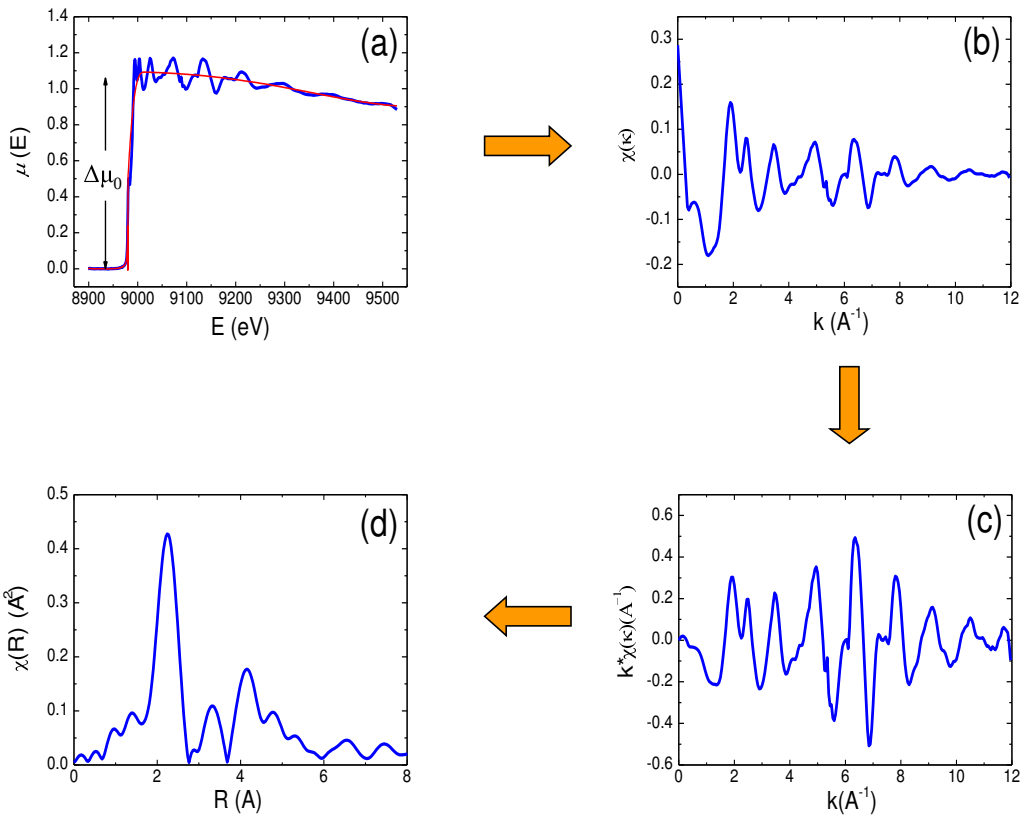

Figure 2.9. XAFS analysis process. (a) The raw XAFS spectrum is pre-edge subtracted to remove the background and then be normalized. (b) The normalized spectrum is converted into k-space and (c) be k-weighted, and (d) finally be Fourier transformed into real-space. Figure is reproduced from Ref. [**58**].

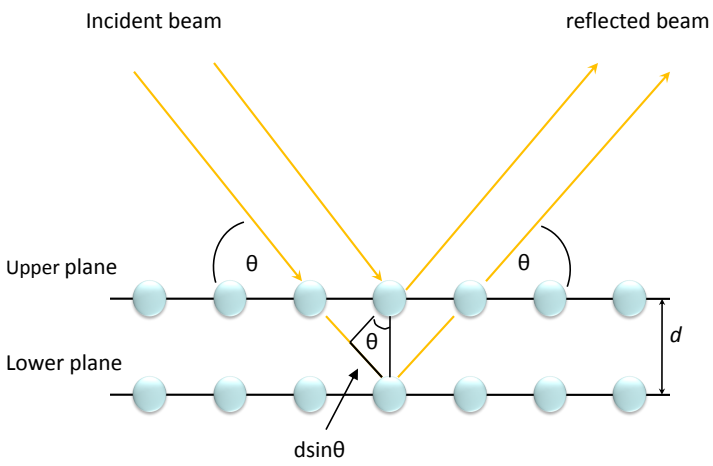

Figure 2.10. Schematic illustration of the Bragg diffraction.

2.3. X-ray powder diffraction (XRD)

X-ray powder diffraction (XRD) is widely used to determine crystal structures based on their diffraction patterns. In general, XRD could (1) determine the crystal structures of identified materials and (2) identify single- or multi-phase conditions according to Bragg diffraction law:

$$2d\sin\theta = n\lambda \tag{2.7}$$

where d is the atomic interplanar spacing; θ is the diffraction angle; n is an integer; λ is the wavelength of the x-ray. The angle of the diffraction is related to the atomic interplanar spacing (Fig. 2.10) and the intensity of the diffraction peak depends on the exact positions of atoms in the unit cell, which is the structure factor, and their disorder. The structure factor ($F(Q)$) and its relationship to the x-ray intensity (I) can be expressed as:

$$F(Q) = \sum_{r_j} F_j^{mol}(Q) e^{iQ\cdot r_j} \tag{2.8}$$

$$I = |F(Q)|^2 \tag{2.9}$$

Here r_j is the position of the j^{th} molecule in the unit cell [**58**]. In this work, in order to obtain the pressure-induced volume change (compressibility), XRD was collected in a diamond anvil cell (Chapter 3) using the angle-dispersive setup at the sector 16 of the Advanced Photon Source (Fig. 2.11).

As shown in Fig. 2.11, the diffraction patterns were collected using a MAR345 image plate (pixel size 100 $\times$ 100 gm^2. The collected two-dimensional diffraction rings on the image plate (Fig. 2.12(a)) were integrated with FIT2D program [**59**] into diffraction pattern of intensity versus 2θ (Fig. 2.12(b)). In this work, Rietveld refinement [**60**] was employed to determine crystallographic structures, lattice parameters, and quantitative amounts of different phases in pressure-induced multi-phase mixtures of the materials.

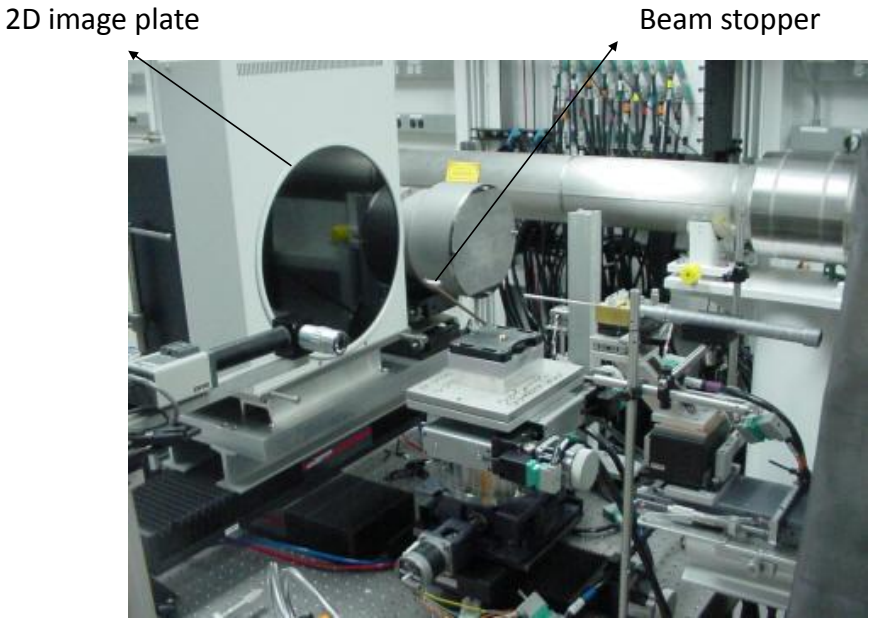

Figure 2.11. Angle-dispersive powder diffraction setup. Figure is taken from Ref. [**61**].

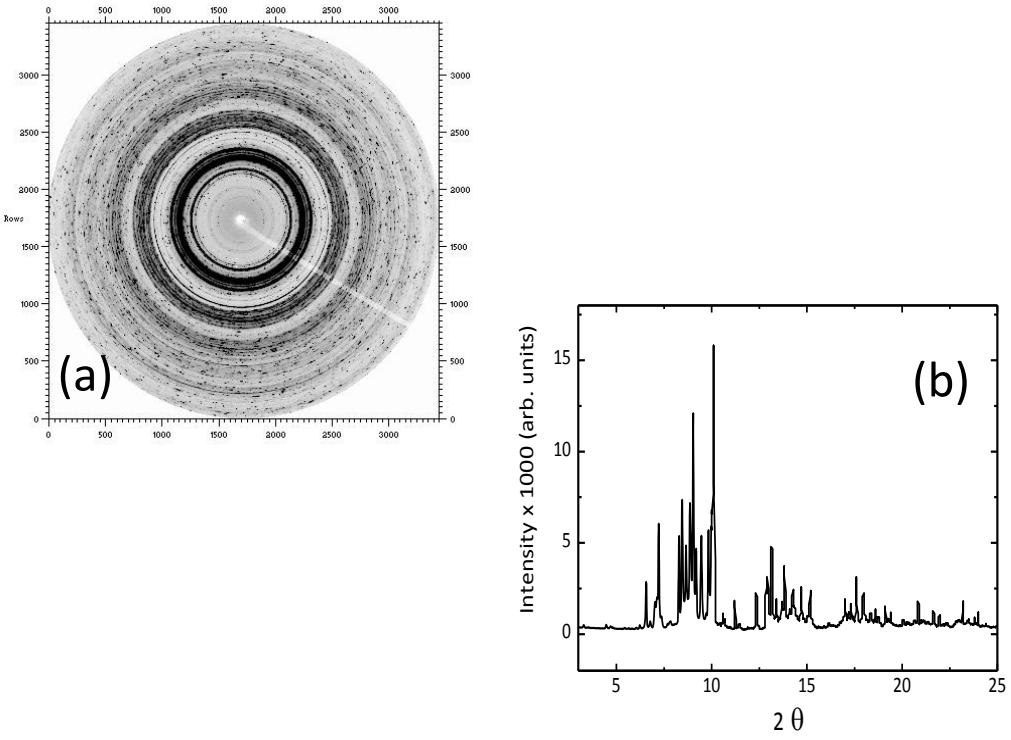

Figure 2.12. (a) The diffraction pattern of $Gd_5(Si_{0.5}Ge_{0.5})_4$ sample collected using a 2-dimensional image plate and (b) integrated into an intensity vs 2θ diffraction pattern.

CHAPTER 3

High pressure experimental setup

3.1. High-pressure XMCD beamline setup

High-pressure XMCD measurements were carried out at beamline 4-ID-D of the Advanced Photon Source, Argonne National Laboratory. The beamline setup is shown in Fig. 3.1. A 1×1 mm^2 x-ray beam produced by a 2.4 m-long linear undulator insertion device is monochromized by a Si (111) double-crystal monochromator [**32, 33**]. For XMCD measurements, the linearly polarized x-rays are converted to circularly polarized by means of a C(111), 100 μm-thick diamond crystal phase retarder (PR) optics [**34**]. Toroidal (Pd) and flat (Si) mirrors focus the x-ray beam to $\sim$ 100×180 μm^2 at the position of the slit before the sample. Harmonic rejection is critically important during the measurements due to the significant attenuation of PR, diamond anvils and the sample (100 $\sim$ 500 times at 7 keV), and the focusing mirror can provide a combined harmonic rejection of $\sim$ 105 at 7 keV. Additional harmonic rejection can be achieved by detuning the second Si (111) crystal of the monochromator away from its Bragg-peak as needed. A split ion-chamber (IC) is used to monitor and maintain the vertical beam position by adjusting the angular position of the second Si (111) crystal using a PZT and a feedback loop. The x-ray beam size is further reduced to either (100×100) or (50×50) μm^2 according to the aperture of the perforated diamond anvils (will be discussed below).

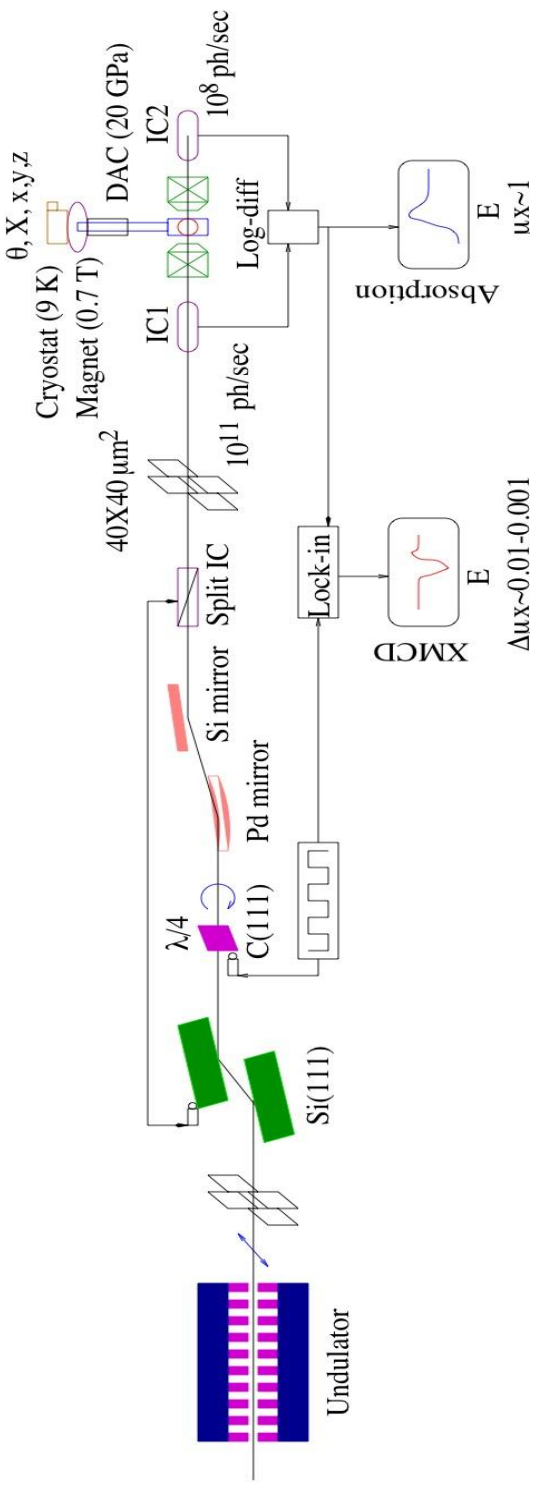

Figure 3.1. Schematic illustration of the experimental high-pressure XMCD setup established at beamline 4-ID-D of the Advanced Photon Source, Argonne National Laboratory.

IC1 and IC2 are used as detectors of incident and transmitted intensities, located before and after the sample, respectively. The XMCD signal is collected by modulating the x-ray helicity at 11.7 Hz and detecting the related modulation in the absorption coefficient with a lock-in amplifier [**62**].

A non-magnetic, piston-cylinder type copper-beryllium diamond anvil cell (DAC) manufactured by easyLab Technology is mounted on a helium-flow cryostat with an extended cold-finger (Fig. 3.2). The DAC reaches temperature as low as ~ 9 K. The cryostat itself is mounted on high resolution x, y translation stages for sample positioning with 1 μm accuracy, and placed between the pole pieces of an electromagnet, which provides a maximum magnetic field strength of 0.7 Tesla at the sample position. The long-travel X-translation stage is used to move the sample in and out of the electromagnet in order to do sample loading and in-situ pressure calibration using the ruby fluorescence method. A Huber 410 goniometer allows a θ rotation of the cryostat/DAC about the vertical axis. This allows to rotate the single crystalline diamond anvils away from unwanted Bragg diffraction which otherwise gives rise to glitches in the absorption spectra.

3.2. Diamond anvil cell (DAC)

The Diamond anvil cell (DAC) is typically used for high pressure experiments. In a conventional DAC, the material of interest is placed in the cell, in which the opposing force will be applied through the backing plates to the anvils generating pressure on the sample located in a cavity of a gasket. In this work, the absorption edge of interest is Gd L_3 (7.243 keV). In order to reduce diamond absorption at this particular edge, the diamonds were perforated. The DAC consists of a fully perforated diamond anvil (FPA) which serves as a backing plate for a mini-anvil (MA) 0.7 mm high, and an opposing, partially perforated anvil (PPA) with a 0.1 mm

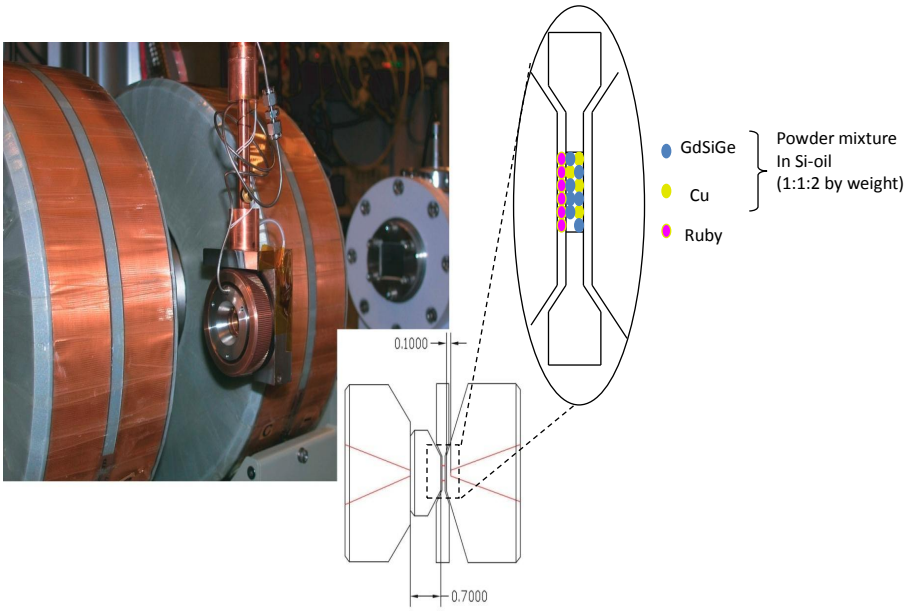

Figure 3.2. Membrane-driven diamond anvil cell mounted on the cold finger extension of a He-flow cryostat. A schematic of the asymmetric diamond anvil configuration, including fully-perforated-, partially-perforated- and mini-anvil is shown in the inset. The sample mixture (described in text) is loaded into a drilled cavity of the pre-indented gasket.

inner wall. Paired 0.6 or 0.45 mm culets for the MA and PPA were used in the DAC depending on the target pressure ranges. For 0.6 mm culet, pressure up to 16 GPa can be generated; for 0.45 mm culet, a maximum P of $\sim$ 23 GPa has been reached. The configuration of the DAC is shown in Fig. 3.2 [**63**]. The asymmetric configuration of the DAC retains a smooth optical surface on the mini-anvil side to allow in-situ ruby fluorescence pressure calibration. The rough inner surface of the partial conical perforation scatters strongly the optical fluorescent photons and reduces the intensity.

Unlike a strain-gauge pressure cell whose pressure needs to be increased ex-situ by a knob and then to be read via a transducer, pressure is changed in-situ in our DAC by controlling

the He-gas pressure in an expanding membrane which drives the piston motion of the cell. The He-gas pressure can be adjusted remotely by a pressure-control-box connected to a He cylinder bottle. The advantage of this setup is no need for warming up the cryostat for removing the DAC. While the disadvantage is that the sizable DAC inevitably limits the minimum gap of the electromagnet hence reducing the strength of the magnetic field.

3.3. Sample preparation

The sample preparation requires three elements − pressure medium (Si-oil), pressure calibrant (Cu or ruby powders), and the material of interest ($Gd_5(Si_xGe_{1-x})_4$ compounds), as shown in Fig. 3.2. The samples used in measurements require very fine powders size, usually less than 1 μm in diameter. If the pressure calibrant is Cu, the mixture of the sample follows a weight ratio of 1:1:2 for $Gd_5(Si_xGe_{1-x})_4$, Cu powders and silicon-oil, respectively in order to yield an ideal absorption jump of $\sim$ 1 for both Gd L_3 and Cu K -edges. If the pressure calibrant is ruby, its powders need to be homogeneously coated on the surface of the MA without mixing with $Gd_5(Si_xGe_{1-x})_4$ and silicon-oil. This allows the emitted ruby fluorescence to be collected efficiently through the perforation of the FPA. The sample mixed with Cu calibrant if needed is then loaded into a 250 μm hole in a nonmagnetic stainless steel gasket, which was pre-indented down to a thickness range of 80 - 60 μm depending on the target pressure range.

3.4. Pressure calibration

Two in-situ pressure calibration methods, Cu XAFS and ruby fluorescence have been used in this work for different considerations. In the beginning, Cu XAFS was used due to the unavailability of ruby-fluorescence optical system. However, this method requires energy switching between different absorption edges (Gd L_3 and Cu K -edges) and extended energy XAFS scans

through the absorption edge of the calibrant material, which is very time consuming. Another disadvantage of the Cu XAFS is that its absolute accuracy is about 0.5 - 1 GPa, poorer than $\sim$ 0.1 GPa acquired in the ruby fluorescence method. The relative change in pressure can be determined with much better accuracy of $\sim$ 0.1 GPa. In addition, Cu XAFS is easily affected by Bragg diffraction induced by the single crystalline diamond anvils which heavily worsens the calibration results. The advantage of the Cu XAFS is that a smooth optical surface of a diamond anvil required in ruby fluorescence method is not necessary, which reduces the cost of diamond anvils. In general, pressure calibration using Cu XAFS is useful when optical access to the DAC is not feasible. The reason why XRD was not used as a pressure calibration method in this work is because it requires a CCD camera (described in Chapter 2) which is not the standard apparatus in 4-ID-D beamline.

3.4.1. Cu XAFS pressure calibration

In-situ pressure calibration using x-ray absorption fine structure measurements can be traced to Ref. [**55, 64**]. Copper is suitable for this method as it has a cubic structure and a known compressibility [**65**]. In addition, its K absorption edge (8.979 keV) is in close proximity to the energy of the wanted measurements (Gd L_3 is 7.243 keV). Since XAFS can probe the local structure of the selected atom (described in chapter 2), it can, therefore, determine the pressure by comparing the bond-length changes against the known compressibility of the calibrant. Fig. 3.3(a) shows raw absorption spectra of Cu K -edge for different pressures. The data were collected from a reference Cu powder sample ($< 1\mu$m), outside (ambient condition) and inside the DAC (2.4 and 9.8 GPa) respectively. It is known that the phase of the XAFS signal depends on inter-atomic distances through

$$\chi(k) \approx \sin[2kR_j + \delta_j(k)] \tag{3.1}$$

where R_j is the bonding length and δ_j is the scattering phase shift. A volume reduction would result in a reduction of the photoelectron phase $2kR$ and an elongation outwards of the k-dependent XAFS oscillations, as shown in the inset of Fig. 3.3(a). The changes in inter-atomic distance with pressure can also be clearly seen in the Fourier transform (FT) of the XAFS as shown in Fig. 3.3(b). The fitting model used FEFF 6.0 standards [**66**] and IFEFFIT 2.8 package [**67**], assuming a uniform compressibility of all Cu-Cu bonds, and the real space fits include contributions from the first two atomic shells only.

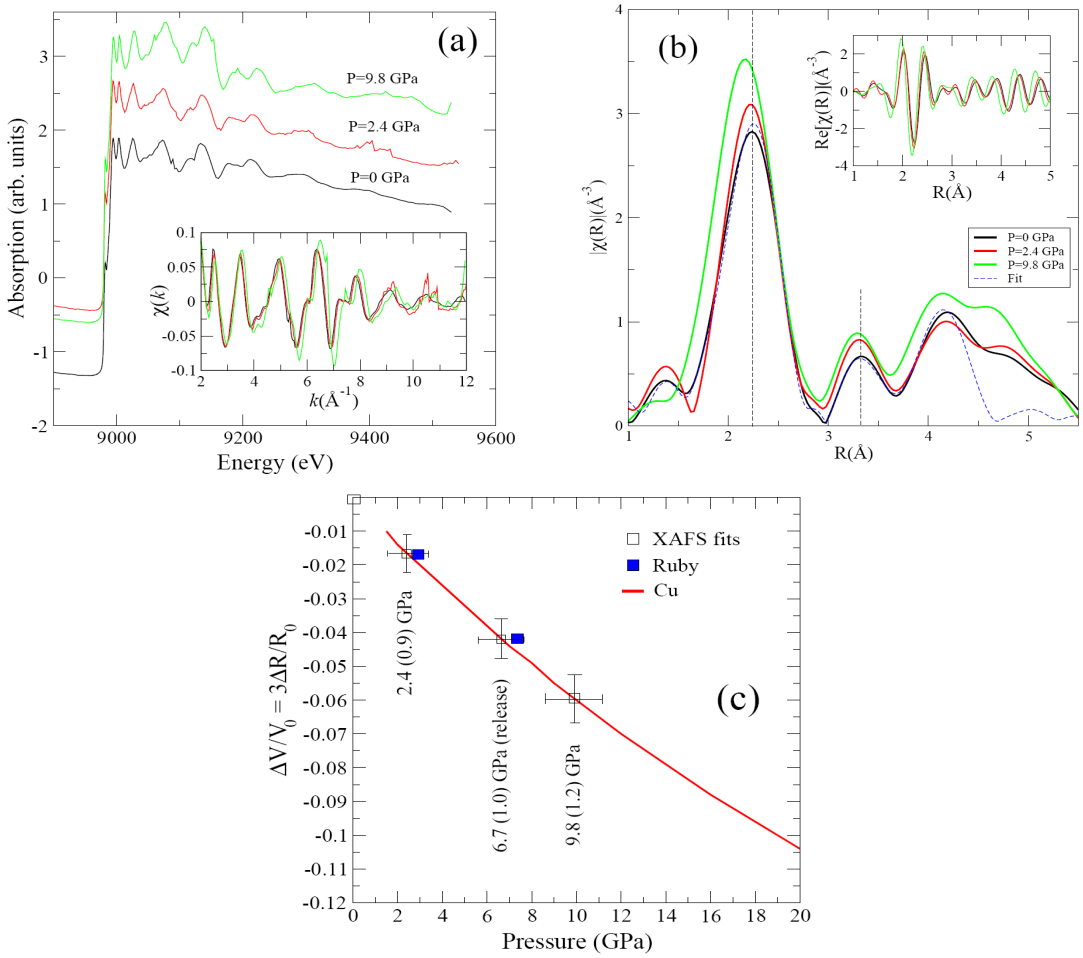

Figure 3.3. (a) Raw Cu K-edge absorption spectra measured at different pressures. Inset shows the background-removed XAFS data.(b) Magnitude (main panel) and real part (inset) of the complex Fourier transform of XAFS data together with representative fits. (c) Pressure calibration using the volume reduction measured by XAFS (empty squares) and the compressibility of Cu at 300 K (red curve). Pressure calibration from ruby fluorescence is also shown (filled squares)

In addition to the decrease in inter-atomic distance, the amplitude increase of the FT is also evident as a result of the decrease of bond-length vibrational disorder upon volume reduction. The pressure was obtained by interpolating the fitted volume change (ΔV) into the known compressibility curve of Cu at 300 K. The fitted volume change can be expressed as

$$\Delta V/V_\circ = 3 \times \Delta R/R_\circ \tag{3.2}$$

where ΔR is the change of bond-length. The pressures obtained from the fitted Cu XAFS were compared with those gained from ex-situ ruby pressure calibration, as shown in Fig. 3.3(c).

3.4.2. Ruby fluorescence pressure calibration

Ruby fluorescence, which is the most widely used pressure calibration method in high-pressure research [**68**] was employed in this work. This method utilizes the spectral shift of the ruby (α-Al_2O_3 contains Cr^{+3}) fluorescence R lines (R_1 and R_2) with the variation of external stress (pressure) [**69**] as shown in Fig. 3.4. It is important to note that the peak positions of R_1 and R_2 will shift with temperature change. In order to account for both pressure- and temperature-dependent shifts of the spectra during the calibrations, a program consulting the fitting formulas reported in Ref. [**70**] was used. The most accurate way to calibrate the pressure is to take the average of two R lines. However, because of the weak intensity of R_2 at low temperature, only R_1 was used for calibration during low temperature measurements. The reported pressure values using ruby fluorescence in this work were the average of that obtained at the lowest temperature ($\sim$ 9 to 17 K) and room temperature (300 K), the difference being usually smaller than $\sim$ 1.5 GPa. The spectra were taken from a portable ruby fluorescence system manufactured

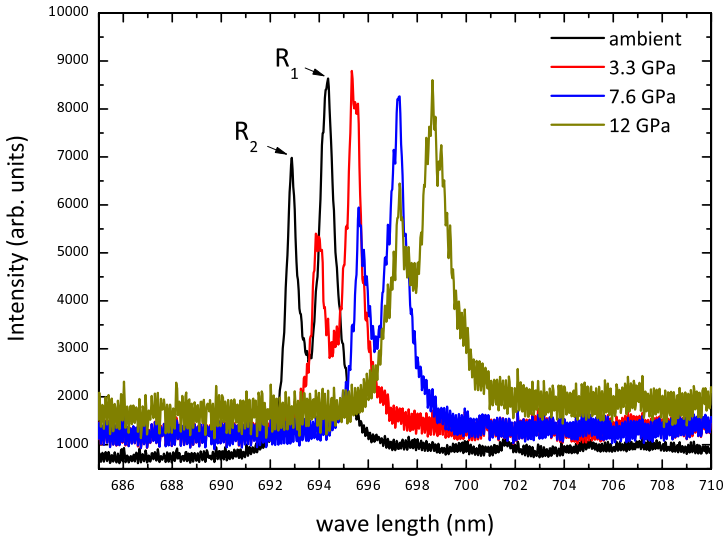

Figure 3.4. Pressure-dependent ruby R-line fluorescence spectra taken at room temperature by Optipress (now easyLab). Pressure was calibrated by translating the cryostat/DAC into the ruby fluorescence station on the side of the electromagnet, as shown in Fig. 3.5 [**71**].

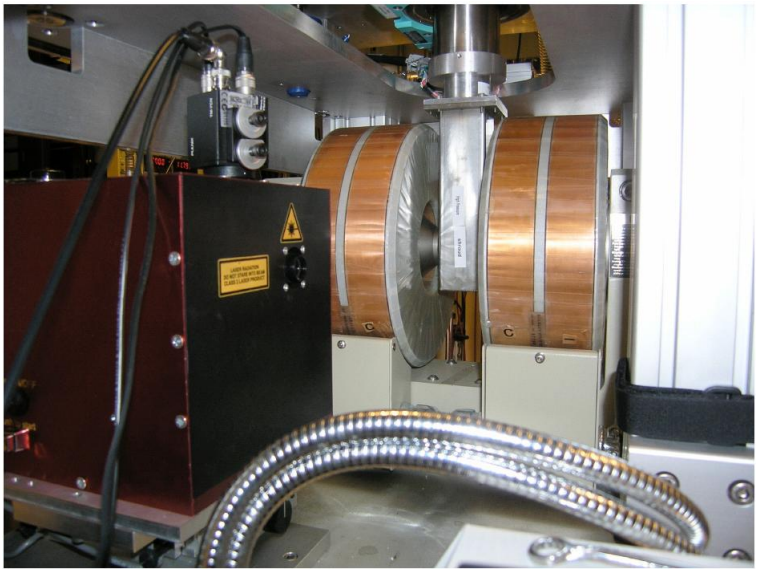

Figure 3.5. Portable ruby fluorescence detector assembled to a translation stage nearby the electromagnet and cryostat.

CHAPTER 4

Role of Si-doping in enhancing ferromagnetic interactions in $Gd_5(Si_xGe_{1-x})_4$ compounds

4.1. Introduction

According to the phase diagram of $Gd_5(Si_xGe_{1-x})_4$ [**13**], in the compositional range $0.24 \leq x \leq 0.5$, the giant MCE is related to a 1st order, magnetic-crystallographic phase transition, in which a PM $\rightarrow$ FM transition on cooling is accompanied by a change in crystal structure from a M to O(I) phase [**18, 19**]. The Ge-rich alloys ($0 \leq x \leq 0.2$), on the other hand, exhibit two phase transitions on cooling: a 2nd order PM $\rightarrow$ AFM transition and a 1st AFM $\rightarrow$ FM transition at lower temperatures. This second transition is accompanied by a structural transition between two orthorhombic polymorphs, i.e. between the so-called O(II)-type structure and O(I) [**20**]. The most notable feature of these phase transitions is the reversible breaking and reforming of covalent Si(Ge)-Si(Ge) bonds connecting Gd-containing slabs, which occurs concomitantly with the change of magnetic state. The crystal structure changes via a martensitic-like mechanism, involving large shear displacement (~ 0.5 Å) of sub-nanometer-thick Gd-containing slabs [**18, 19**]. Since this reversible phase transition can be manipulated by application of a magnetic field, most investigations [**18-21**] of the MCE in these materials have been carried out within the compositional range for $0.24 \leq x \leq 0.5$. In particular, $Gd_5(Si_xGe_{1-x})_4$ is the most (heavily) studied, because its magneto-structural transition occurs near room temperature [**18-21**].

Although for Ge-rich ($0 \leq x \leq 0.2$) and middle range ($0.24 \leq x \leq 0.5$) compositions the material is characterized by different magnetic-crystallographic phases, the FM ordering temperature, T_c, is linearly dependent on Si content. For example, for the three compositions $x =$ 0.125, 0.375 and 0.5 discussed in this chapter, T_c of 80 (3), 190 (5) and 275 (3) K, respectively, are obtained [**72, 73**]. As addressed in Chapter 1, since Si and Ge atoms have markedly different sizes, the unit cell volume is affected by the Si/Ge ratio. Similarly, hydrostatic pressure (P) has been used to alter the unit cell volume, and dT_c/dP of ~ 3.0 K kbar^{-1} has been reported for the $0 \leq x \leq 0.5$ range [**28**]. The goal of this work is to extend the pressure range up to ~ 18 GPa in order to better explore the correlation between Si doping-induced chemical pressure and applied pressure upon the magnetic transitions. In addition, XAFS measurements of the Ge and Si local structure were carried out in order to understand the effect of local lattice distortion around Si dopants. These will be discussed in Chapter 6.

4.2. Experiment

Polycrystalline samples of $Gd_5(Si_xGe_{1-x})_4$ for $x = 0.125$, 0.375 and 0.5 were prepared as described by Pecharsky and Gschneidner [**18**]. In addition, the alloys were heat treated at 1300 °C for 1 hour. Fine powders (≤ 1 μm) of $Gd_5(Si_xGe_{1-x})_4$ were thoroughly mixed with fine powders (≤ 1 μm) of Cu and dispersed in silicon oil which was used as hydrostatic pressure medium. The sample preparation followed the recipe described in Chapter 3, and the in situ pressure calibration was done by measuring Cu XAFS as described in the same chapter. High-quality transmission x-ray data were collected over the Gd L_3 (7.243 keV) and Cu K (8.979 keV) -edges through perforated anvils in the DAC. Gd L_3 (7.243 keV) edge was probed under an applied field strength of ~ 0.7 Tesla.

4.3. Results for $Gd_5(Si_{0.125}Ge_{0.875})_4$ and $Gd_5(Si_{0.5}Ge_{0.5})_4$ compounds

The pressure dependence of the magnetic transition was measured in the 0.25 - 14.55 GPa range for $x = 0.125$ and $x = 0.5$ samples. Figure 4.1 shows temperature-dependent Gd L_3 -edge XMCD data for the $x = 0.125$ sample at applied pressure of 0.25 GPa (Fig. 4.1(a)) and 14.55 GPa (Fig. 4.1 (b)). The inset figures show that the XMCD signal fully reverses upon reversal of a 0.7 Tesla applied field as expected. The XMCD signal does not change significantly from 20 to 80 K, but drops quickly at 90 (3) K. This drop is due to the magneto-structural, 1^{st} order phase transition, which at ambient pressure occurs at 80 (3) K [**23**] as confirmed with XMCD measurements outside the DAC [**73**]. At P = 14.55 GPa the magnetic transition has significantly shifted upward in temperature.

Figure 4.2(a) and (b) show the integrated area under the XMCD curves for $x = 0.125$ and 0.5, respectively, both normalized to the low-temperature saturation value as a function of temperature for different applied pressures. The data show that the magnetic transition temperature, T_c, is enhanced with pressure in both samples. It changes from 80 (3) K at ambient pressure to 257 (5) K at P = 14.55 GPa for $x = 0.125$, and from 275 (3) K at ambient to 336 (5) K at P = 10 GPa for $x = 0.5$.

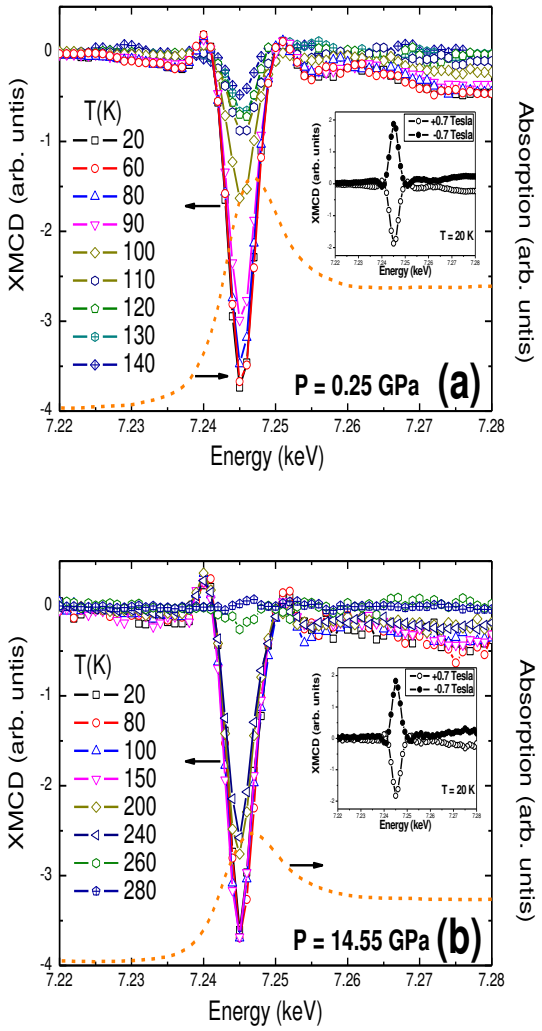

Figure 4.1. Gd L_3 -edge XMCD signal (normalized to the absorption edge jump) as a function of temperature for (a) P = 0.25 GPa and (b) P = 14.55 GPa, for $x = 0.125$ sample. The insets show the reversal of XMCD signal upon reversal of applied magnetic field. The helicity-independent absorption spectra, obtained as the average of absorption spectra for opposite helicities, is shown by the dashed lines. The sample thickness decreases with pressure causing a reduction in absorption edge jump.

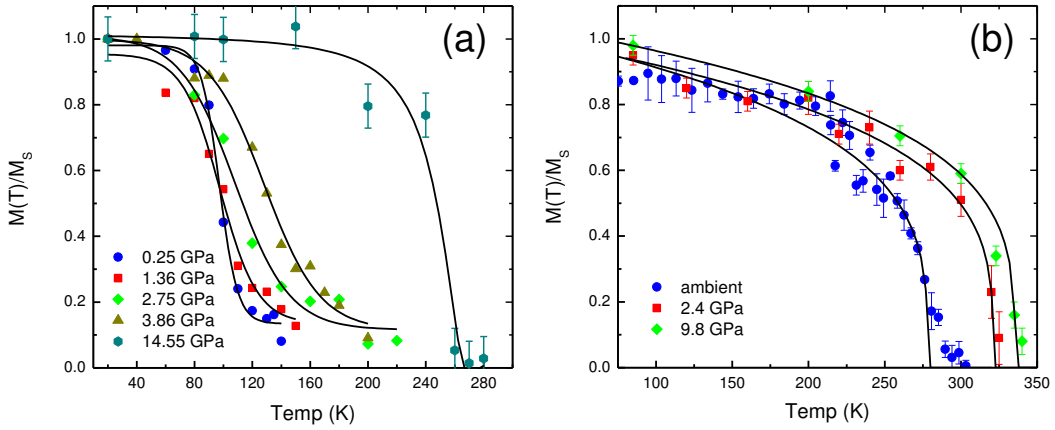

Figure 4.2. Integrated XMCD as a function of temperature for different applied pressures for (a) $x = 0.125$ and (b) $x = 0.5$ samples. The XMCD signal is normalized to the saturation value at 20 K. The lines are guides to the eye. Error bars shown for P = 14.55 GPa data in (a) are the same for the other data sets.

Here, T_c is determined from the maximum absolute value of the derivative of the fitted lines. Another notable feature of the data for $x = 0.125$ sample is the presence of a non-zero XMCD signal above T_c for P = 0.25, 1.36, 2.75, 3.86 GPa, which is related to the AFM phase present in the low-x region ($x \leq 0.2$), whereas this feature is not observed at 14 GPa in this sample, or at any pressure in the $x = 0.5$ sample.

The pressure dependence of T_c for $x = 0.125$ and $x = 0.5$ is summarized in Figs. 4.3 (a) and (b), respectively. The dependence of T_c on x (ambient pressure) is superimposed to highlight the correspondence between x and P.

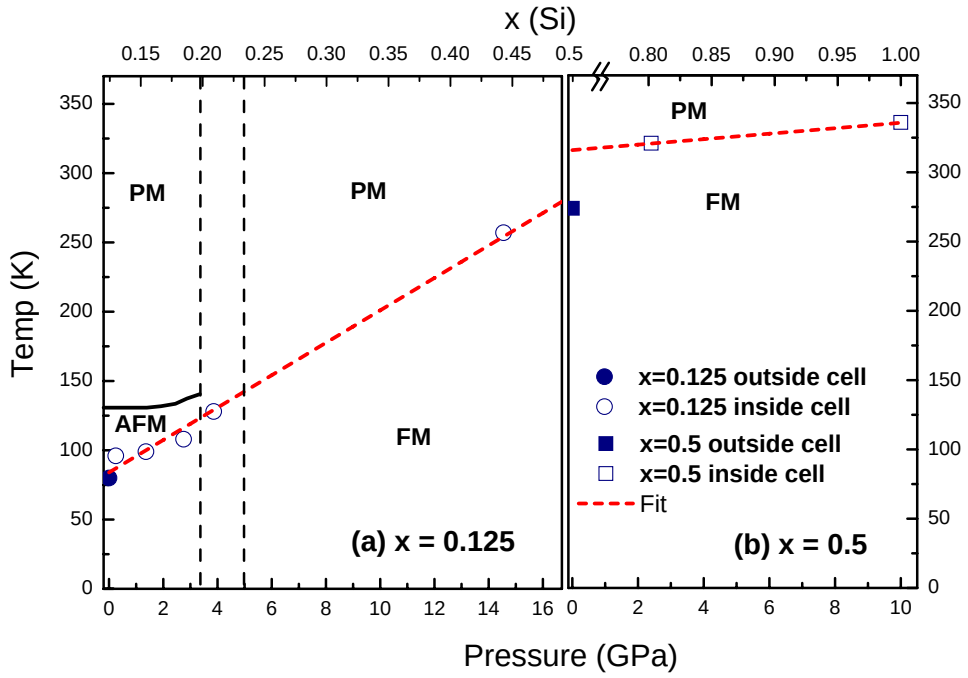

Figure 4.3. Magnetic phase diagram as a function of Si concentration (top) and applied pressure (bottom). The points indicate the observed Curie temperatures, T_c, for different pressures as measured by XMCD for (a) $x = 0.125$ and (b) $x = 0.5$ samples. The "outside cell" data correspond to ambient pressure condition.

The overlaying x scale is determined by using known $T_c(x)$ values from the literature [**25**] for $x = 0.125$, $x = 0.5$ and $x = 1.0$ at P = 0. One can see that the general features of $T_c(x)$ are also present in T_c(P), namely a linear dependence of T_c on P, with a change in slope at $x \sim 0.5$. As we discuss below, an additional common feature is the disappearance of the FM-AFM transition on warming for P > 4 GPa, which manifests itself in the XMCD data as a non-zero XMCD signal above T_c.

4.4. Discussions for $Gd_5(Si_{0.125}Ge_{0.875})_4$ and $Gd_5(Si_{0.5}Ge_{0.5})_4$

The non-zero XMCD signal above T_c for P < 4 GPa in Fig. 4.2(a) indicates the presence of a small ferromagnetic component. Non-zero magnetization above T_c with a similar ratio of $M_s/M_{tail} \sim 5.5$ was also observed in the SQUID data of Morellon et al. [**23**] for an $x = 0.1$ compound. The low-x, Ge-rich compounds are known to undergo a FM-AFM transition at ambient pressure before they become paramagnetic at higher temperature. This intermediate transition is only observed for $x \leq 0.2$, while higher x samples directly transform into a paramagnetic phase on warming [**14, 18, 25**]. The non-zero XMCD tail for $T > T_c$ is likely due to canting of the AFM structure induced by the 0.7 T applied field. For example, Gd_5Ge_4, which is AFM at zero field displays significant canting in an applied field [**74**]. The non-zero XMCD tail is not present in the P = 14.55 GPa data, indicating a direct transition from FM to PM state at this pressure. The presence of a tail for P < 4 GPa (which in Fig. 4.3 (a) is shown to be equivalent to $x < 0.22$) and its absence at P = 14.55 GPa (equivalent to x $\sim$ 0.43) is in agreement with the occurrence of the FM-AFM transition only at low x (low pressure) and its absence at high x (high pressure).

The $P(x)$-T phase diagram shown in Fig. 4.3 highlights the pressure−Si correspondence. Starting with $x = 0.125$ sample, pressures of P = 0.25, 1.36, 2.75, 3.86 and 14.55 GPa produce a

temperature-dependent magnetization corresponding to x = 0.14, 0.15, 0.17, 0.22 and 0.44, respectively, resulting in Δ(Si%)/ΔP = 0.205 (Si%) kbar^{-1} (Fig. 4.3(a)). The pressure dependence of the magnetic transition temperature, T_c, is linear with a slope dT_c/dP = 1.2 K kbar^{-1}. For comparison, a value of dT_c/dP = 3.0 K kbar^{-1} was obtained in Ref. [**28**] for a limited pressure range below 1.0 GPa.

The XMCD data measured on the $x = 0.125$ sample outside the DAC at ambient pressure [**73**] show a Curie temperature of 80 K, which is in agreement with previous SQUID measurements [**14, 23**] and also very close to T_c = 84 K found by a linear extrapolation to P = 0 of the data in Fig. 4.3(a). At the other end of the x scale in this panel, a T_c of 284 K is found by extrapolating the fit to $x = 0.5$, which is 9 K higher than 275 K directly measured in $x = 0.5$ sample at ambient pressure [**73**] (represented by the filled square in Fig. 4.3 (b)).

The data shown in Fig. 4.3 (b) correspond to measurements performed on an $x = 0.5$ sample. Applied pressures of P = 2.4 and 10 GPa result in T_c of 321 (5) and 336 (5) K, corresponding to the x values of 0.8 and 1.0, respectively [**14, 18, 25**]. Interestingly, x = 0.5 sample at an applied pressure of 10 GPa shows the same magnetic ordering temperature as pure Gd_5Si_4 with T_c = 336 K. In addition, even though a T_c of 336 (5) K is the ultimate transition temperature achieved by doping Si up to $x = 1.0$ sample, the data indicate that further increases in transition temperature are expected for pressures beyond 10 GPa. This means that hydrostatic pressure provides an additional flexibility in manipulating T_c than Si doping does (albeit in a reversible way), because it is not limited by the end boundaries of the solid solution.

At ambient pressure, the x = 0.5 sample is located near a structural boundary. While it is monoclinic (M) at room temperature, a slight increase in Si concentration drives it into the orthorhombic (O(I)) phase with a concomitant increase in T_c. Since the compressibility

of monoclinic and orthorhombic phases are markedly different [**75**], this structural transition is responsible for the observed discontinuity in dT_c/dx at $x \leq 0.5$ [**14, 18, 25**]. Similarly, pressure causes a 1st order M $\rightarrow$ O(I) transition in $x = 0.5$ sample within a range of P $\sim$ 1.0$-$2.0 GPa [**26**], with T_c changing from 275 to 305 K. Here the smallest pressure of P = 2.5 GPa is large enough to cause the transition into the O(I) phase, and this transition with its related T_c increase is responsible for the discontinuity in dT_c/dP. The slope of a fit through P = 2.4, 10 GPa data points yields a $dT_c/dP = 0.2$ K kbar^{-1}, which is lower than the 0.9 K kbar^{-1} reported in Ref. [**76**]. The correspondence between doping and pressure using the x = 0.5 data is Δ(Si%)/ΔP = 0.26 (Si%) kbar^{-1}, which is comparable to 0.205 (Si%) kbar^{-1} obtained using the $x = 0.125$ data in Fig. 4.3(a).

The results clearly demonstrate that the FM $\rightarrow$ PM transition in $Gd_5(Si_xGe_{1-x})_4$ alloys is similarly affected by Si doping and applied pressure at least in a qualitative way. Magnetic interactions between localized Gd 4f moments are indirect since there is virtually no overlap between Gd 4f wave-functions. Most intermetallic alloys exhibit an indirect Ruderman-Kittel-Kasuya-Yosida (RKKY) [**77**] coupling through a spin-polarized conduction band. While this is likely the dominant mechanism for exchange coupling between Gd ions inside Gd-slabs (intra-slab), it has also been argued [**14**] that an indirect super-exchange coupling [**78**] plays a role in mediating inter-slab coupling through the intervening, non-magnetic Si(Ge)-Si(Ge) bonds that connect the Gd slabs in the FM, orthorhombic structure. The recent observation of magnetic polarization in Ge 4p orbital due to hybridization with Gd 5d orbital, however, indicates that RKKY coupling may also be involved in mediating the inter-layer magnetic coupling [**73**].

Regardless of whether the inter-slab coupling is of RKKY or superexchange type, its strength is intimately connected with the overlap of Gd 5d and Si 3p (Ge 4p) states. This overlap is

enhanced by a volume contraction induced by either Si doping or applied pressure. For super-exchange interactions, the increased overlap of magnetic Gd 5d and non-magnetic Si 3p (Ge 4p) states increases the probability for virtual hopping needed to mediate Gd-Gd indirect exchange. For RKKY interactions, the increased overlap between Gd 5d-Si 3p (Ge 4p) states promotes hybridization and the related ability to transfer magnetic interactions through a spin-polarized Gd 5d-Si 3p (Ge 4p) conduction band.

Prior to this study, unambiguously distinguishing between the effects of volume reduction, Si(Ge) site occupancy and changes in electronic structure introduced by Si doping upon the magnetic properties of these materials was difficult. Since the related work done by Morellon et.al [**28**] has revealed that volume contraction affects both electronic and crystal structures in a low pressure range ($<$ 1 GPa), the equivalency between x and P in an extended pressure range shown in this work has demonstrates that the application of pressure in an extended range is able to reproduce all of the features in the x-T magnetic phase diagram. This may be interpreted as an indication that, at least qualitatively, volume-driven effects can account for the observed Si-induced changes in the x-T magnetic phase diagram.

However, evaluating the quantity where is the fractional change in volume-induced by pressure by pressure or doping, provides a measure of the efficiency by which a structural volume change is converted into a change in T_c. Using the compressibility value of κ = -0.25 Mbar^{-1} in Ref. [**27**], and the doping-dependent lattice parameters in [**18**], it is found that Si-doping is more effective in increasing T_c than pressure is for a given volume change. This indicates that Si-doping does more to stabilize ferromagnetic interactions than simply uniformly reducing the volume of the unit cell. A more detailed study for this aspect is presented in Chapter 6.

4.5. Results and discussions for $Gd_5(Si_{0.375}Ge_{0.625})_4$

Due to a limited pressure range attained in above experiments ($\leq$ 15 GPa) [**79**], two different compounds, namely $x = 0.125$ and $x = 0.5$ were needed in order to fully explore the correspondence of pressure and chemical Si doping over the entire $0 < x \leq 1.0$ range. In particular, we were not able to directly demonstrate that the observed discontinuity in $T_c(x)$ at $x = 0.5$ [**25**] is volume-driven. Therefore, a $x = 0.375$ sample with Si content between those of the two previously studied samples ($x = 0.125$ and $x = 0.5$) was measured. This allowed us to directly prove that the discontinuity in $T_c(x)$ at $x \sim 0.5$ is volume driven and also to further establish the correspondence between Si doping (chemical pressure) and physical pressure in this class of giant magnetocaloric effect compounds. The T_c of $x = 0.375$ increases with pressure, as was also observed for both $x = 0.125$ and $x = 0.5$ samples. The magnetic transition temperatures as a function of pressure for $x = 0.125$, $x = 0.375$, and $x = 0.5$ samples are presented in Fig. 4.4(a). It is easy to see that the sample with $x = 0.125$ yields a linear dT_c/dP up to $\sim$ 15 GPa, while that with $x = 0.375$ exhibits a discontinuity in dT_c/dP at $\sim$ 7.2 GPa. A similar discontinuity induced by pressure was also observed for $x = 0.5$ [**26, 76, 79**]. It is known that a β (M) $\rightarrow$ α (O(I)) phase transition is responsible for this discontinuity in T_c for $x = 0.5$ as a result of the different compressibilities of M and O(I) structures [**26**]. Since the discontinuity in dT_c/dP occurs at $\sim$ 277 K on both $x = 0.375$ and $x = 0.5$ samples, it is reasonable to assume that the M $\rightarrow$ O(I) structural transition for $x = 0.375$ occurs at $\sim$ 7.2 GPa at T_c of 277 (5) K (see the dashed line in Fig. 4.4(a)). In addition, the dT_c/dP for $x = 0.375$ at pressures below 7.2 GPa in Fig. 4.4 (a) is 1.5 K kbar^{-1}, which is comparable to 1.2 K kbar^{-1} obtained in $x = 0.125$. Furthermore, dT_c/dP measured at higher pressures reduces to 0.15 K kbar^{-1}, comparable to 0.2 K kbar^{-1} obtained for the $x = 0.5$ sample. The good quantitative similarities reveal that $x =$

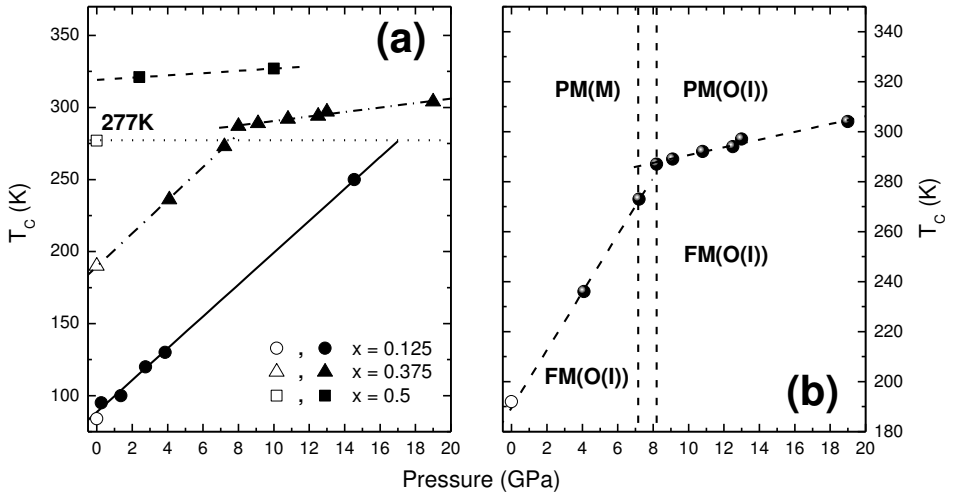

Figure 4.4. (a) The transition temperature as a function of pressure of $x = 0.125$, 0.375, and $x = 0.5$ samples, respectively. Open symbols represent the data measured at ambient conditions. The horizontal dashed line marks slope discontinuity observed for the $x = 0.375$ sample, and the T_c (277K) of $x = 0.5$ under ambient conditions. (b) The $P - T$ phase diagram of $x = 0.375$. The data points indicate the transition temperatures under different pressures. The transition regime is marked by dashed lines located between 7.18 and 8.1 GPa .

0.375 behaves analogously to $x = 0.125$ at low pressures and to $x = 0.5$ at high pressures. This behavior is dictated by the change in compressibility introduced by the M $\rightarrow$ O(I) structural transition.

A P-T diagram is plotted in Fig. 4.4 (b) [**72**] for the $x = 0.375$ sample. The discontinuity in dT_c/dP at 277 K is also observed at this temperature in the x-T phase diagram, where the M $\rightarrow$ O(I) structural transition occurs at $x \sim 0.5$ [**25**]. Hence, our results indicate that this transition is volume driven. When the volume reduction causes T_c to reach 277 K, a low-Si/low-pressure phase (monoclinic) will be converted into a high-Si/high-pressure phase (O(I)).

4.6. Conclusion

Using XMCD we have demonstrated that applying hydrostatic pressure yields similar, qualitative magnetic behavior to that obtained by Si-doping in $Gd_5(Si_xGe_{1-x})_4$ ($x = 0.125$, 0.375, 0.5) over a large pressure range up to $\sim$ 18 GPa. This correspondence is quantified to be 0.233 (Si%) $kbar^{-1}$. All features in the x-T magnetic phase diagram of these materials are also reproduced by applying pressure, namely, the disappearance of the intermediate AFM phase, a linear increase in T_c and a discontinuity in dT_c/dP at T_c of 275 K. Based on the reported compressibility and doping-dependent lattice parameters for these compounds, our results indicate that Si-doping does more to stabilize FM interactions in these materials than is achieved by an uniform reduction in lattice volume alone. This quantitative difference between pressure and Si-doping will be fully addressed in Chapter 6.

CHAPTER 5

Emergence of ferromagnetic order from within antiferromagnetic phase of Gd_5Ge_4: pressure studies of low-x region

5.1. Introduction

In general, the ferromagnetic nature of $Gd_5(Si_xGe_{1-x})_4$ for $x \geq 0.2$ is well established [**14, 18**]. However, the low-x region of the phase diagram is less understood. In this region an intermediate AFM phase is observed for $x < 0.2$ in the 30−130 K temperature range, intermediate to FM (T $<$ 80 K) and PM (T $>$ 130 K) phases (see phase diagram in Fig. 1.5). The presence of this AFM phase at low x and intermediate temperatures, displaying AFM coupling between Gd ions across slabs but FM coupling within the slabs [**76**], is indicative of the close proximity in total energy between FM and AFM phases in the low x region of the phase diagram [**80**]. A contraction of the lattice, either through Si-doping or applied pressure, enhances the inter-slab FM interactions and stabilizes FM ordering. For example, the ground state of pure Gd_5Ge_4 is AFM-O(II) phase, and pressure converts it into FM-O(I) phase [**29**]. However, the mechanism leading to the emergence of FM-O(I) phase from within the AFM-O(II) phase of the parent Gd_5Ge_4 compound at low x is still a matter of debate. In particular, the question arises whether the low-x samples should be described as AFM-O(II)/FM-O(I) mixtures, or otherwise as structurally homogeneous, ternary solid-solutions where competing FM and AFM interactions are simultaneously present [**31**]. Because of the strong electron-lattice coupling present in these compounds, both scenarios are expected to result in an inhomogeneous magneto-structural ground state. This inhomogeneity

could in principle be removed by expanding the lattice volume, which favors an AFM phase, or by contracting the lattice with external pressure or chemical pressure (Si-doping), which favors the FM state [**25, 28, 79, 80**].

In this chapter we present evidence from x-ray diffraction, temperature-dependent bulk magnetization measurements, and x-ray magnetic circular dichroism measurements at ambient- and high-pressure conditions indicating that the magnetism of low-x samples ($0 < x \leq 0.075$) is characterized by the simultaneous presence of the AFM-O(II) and FM-O(I) phases, their volume fractions depending not only on Si content, x, but also on applied pressure and magnetic field. The application of pressure reduces the lattice volume and stabilizes the FM-O(I) phase, leading to a magnetically- and structurally- homogeneous ground state where ordered magnetic moments typical of high x samples are recovered.

5.2. Experiment

Polycrystalline samples of $Gd_5(Si_xGe_{1-x})_4$ with $x = 0$, 0.025, 0.05, 0.075, 0.125 and 0.5 were prepared at Ames Laboratory. The samples were heat-treated at 1300 °C for 1 hour to achieve homogeneous atomic distribution, and then were finely ground into micron-sized powders. X-ray diffraction patterns were collected on a Rigaku TTRAX rotating anode powder diffractometer using Mo Kα radiation and fitted by Rietveld refinement (by Ya. Mudryk at Ames lab). The x-ray powder diffraction measurements at temperatures from 10 K to 300 K and in magnetic fields from 0 to 30 kOe were performed on the same diffractometer equipped with a continuous flow helium cryostat and a superconducting magnet [**81**]. Room temperature results show a linear dependence of the lattice parameters on Si content, indicating that Si incorporates into the lattice (Fig. 5.1). Superconducting Quantum Interference Device (SQUID, Quantum Design MPMS

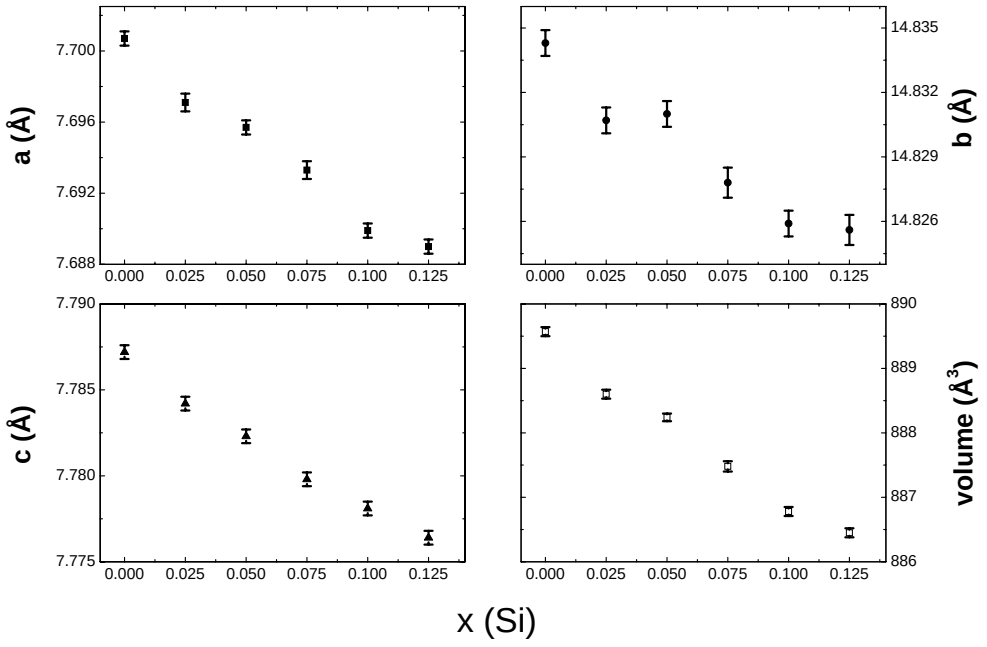

Figure 5.1. Lattice parameters and unit-cell volume of $Gd_5(Si_xGe_{1-x})_4$ compounds at room temperature as a function of Si content. All samples exhibit the O(II)-type structure at ambient conditions.

XL-7) measurements of the dc magnetic susceptibility in a 50 Oe applied field (at Northwestern University), both for field-cooling (FC) and zero-field cooling (ZFC), show that all samples display ferromagnetic transitions with T_c values of 32, 46, 58, 80, and 275 K for $x = 0.025$, 0.05, 0.075, 0.125 and 0.5 respectively (Fig. 5.2). In this chapter results from only $x = 0.025$, 0.05, and 0.075 samples are presented since high-x samples were already described in Chapter 4. Other experimental details related to the high-pressure XMCD measurements are also as described in Chapter 4.

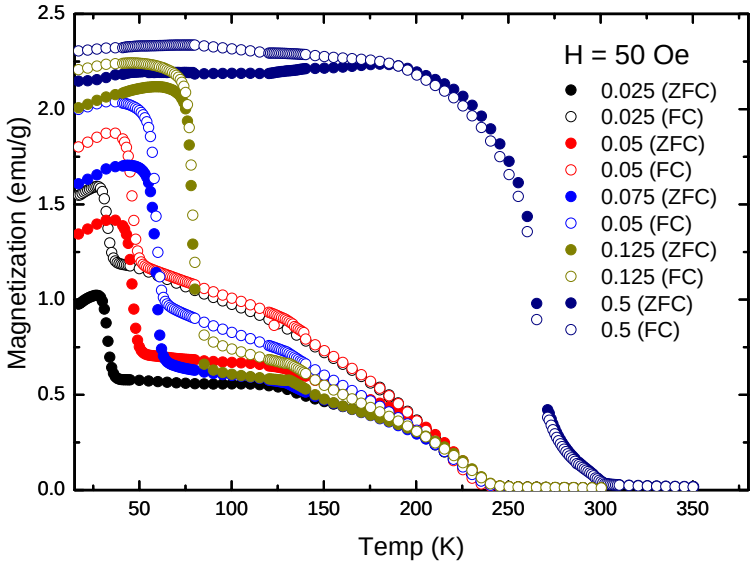

Figure 5.2. Temperature-dependent dc magnetization data of $Gd_5(Si_xGe_{1-x})_4$ compounds for $x = 0.025$, 0.05, 0.075, 0.125, and 0.5 samples measured on warming in a H = 50 Oe applied field after field (FC) and zero-field cooling (ZFC).

5.3. Results

The lattice parameters (a, b, and c) and unit cell volume as a function of x are plotted in Fig. 5.1. All samples have a PM-O(II) phase at room temperature. Fig. 5.2 shows the temperature-dependent FC and ZFC SQUID magnetization data measured on warming for low-x (0.025, 0.05, 0.075) and higher-x (0.125, 0.5) samples. According to the Gd_5Si_4 – Gd_5Ge_4 phase diagram (Fig. 1.5), the lowest temperature transition found in $x = 0.025$, 0.05, 0.075, and 0.125 samples on warming is FM → AFM, and the second transition displaying a week anomaly at ∼ 130 K is AFM → PM, which occurs only for $x < 0.2$ where an AFM intermediate phase is present [**18, 21, 23**]. The $x = 0.5$ sample only shows a FM → PM transition. The ferromagnetic ordering temperature T_c increases linearly with x as expected [**18, 21, 23**], but

the magnetization is strongly reduced below T_c in both FC and ZFC data for $x < 0.125$. The saturation magnetization changes drastically with x at low-x, but is similar for $x = 0.125$ and 0.5 samples. Furthermore, significant irreversibility between FC and ZFC data is observed in the low-x samples, whereas this irreversibility is much less significant in $x = 0.125$ and 0.5 samples.

The x-ray diffraction pattern measured at ambient pressure and 17 K for the $x = 0.025$ sample is shown in Figs. 5.3 (a)−(b), together with Rietveld refinements using single phase [O(I)] and mixed phase [O(I)+O(II)] structural models, respectively. The Rietveld refinements show that both O(II) and O(I) phases are present in the sample, with roughly equal volume fractions at T = 17 K. However, the fraction of O(I) phase at low temperature increases with Si doping, reaching ~ 80 % for $x = 0.05$ (Fig. 5.3(c)).

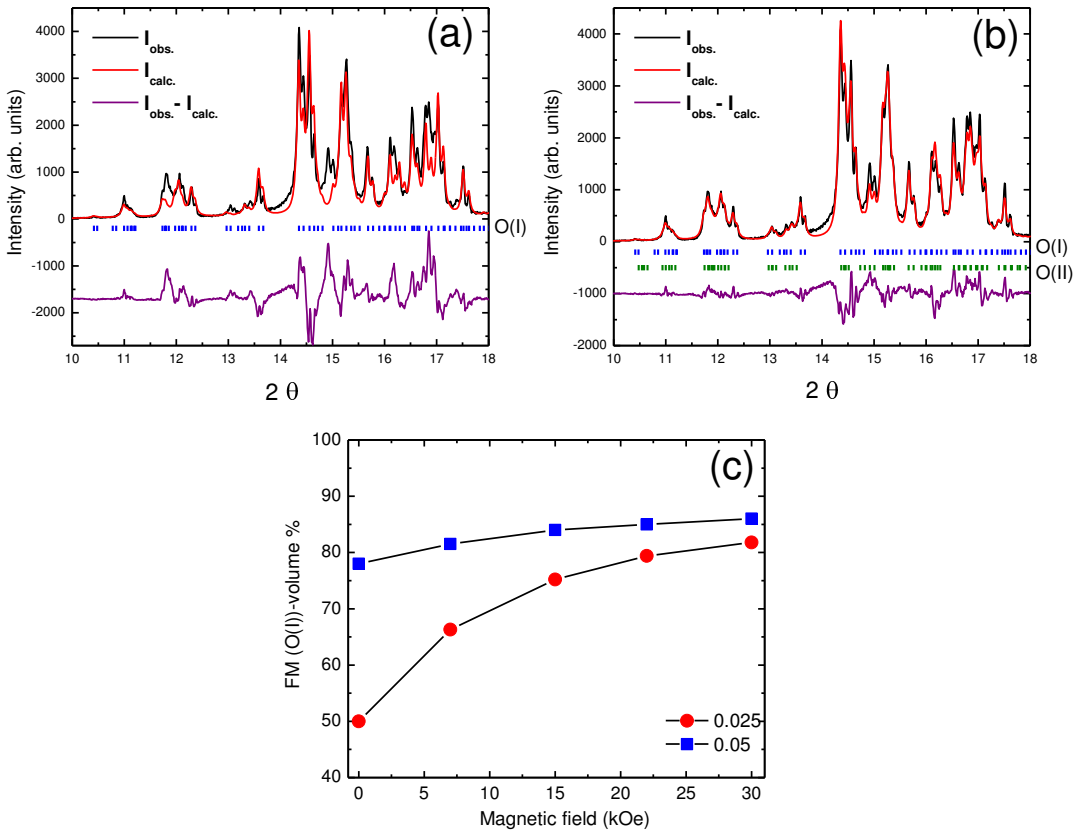

Figure 5.3. X-ray diffraction pattern of $Gd_5(Si_xGe_{1-x})_4$ for $x = 0.025$ at H =0, T = 17 K together with results of Rietveld refinements using (a) single-phase O(I) structure and (b) mixed-phased O(II)/O(I). Quality of fit parameters is $R_p = 22.52$ %, $R_{wp} = 28.04$ %, $R_{Bragg} = 16.12$ % for the single-phase model and $R_p = 9.95$ %, $R_{wp} = 13.15$ %, $R_{Bragg} = 5.52$ % for the mixed-phase model. The x-dependent FM-O(I) volume fraction at T = 17K is shown in (c) as a function of applied field H. Only small fractions of the diffraction pattern are shown in (a) and (b) for clarity.

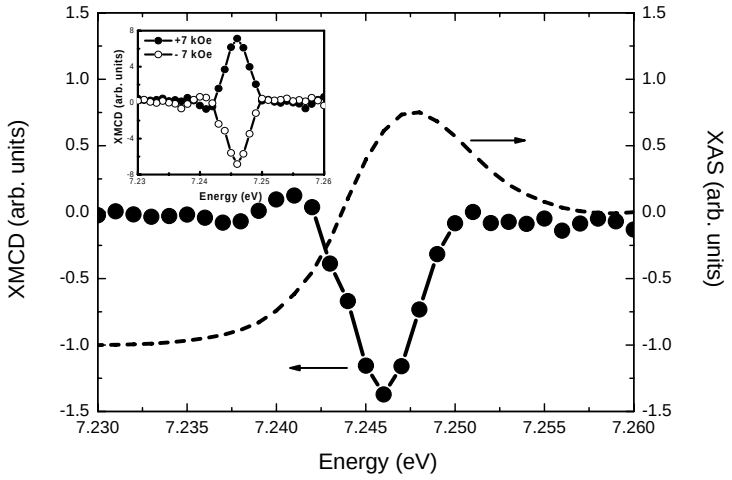

Figure 5.4. X-ray absorption (dashed lines) and edge-jump normalized XMCD signal at the Gd L_3 -edge of $Gd_5(Si_xGe_{1-x})_4$ alloys for $x = 0.025$ a T = 15 K, P = 9.2 GPa, and H = 7 kOe. Inset shows the reversal of XMCD signal upon reversal of the applied magnetic field.

It is also observed that the application of a magnetic field increases the volume fraction of O(I) phase at the expense of the O(II) phase, as shown in Fig. 5.3(c). A field-induced transition from AFM-O(II) to FM-O(I) was previously reported in single phase Gd_5Ge_4 [**20**].

Figure 5.4 shows that Gd L_3 -edge XMCD signal switches upon applied field of ± 7 kOe for $x = 0.025$ sample. Figure 5.5 shows the temperature dependence of the integrated XMCD signal measured in a 7 kOe applied field for the three low x samples at ambient pressure with ZFC. The integrated signals are proportional to the sample's net magnetization. The data show two clear phase transitions. According to the phase diagram [**23, 25**] and as seen in Fig. 5.2, the first transition on warming is a FM → AFM transition while the second transition is AFM → PM, as indicated in the figure. The measured XMCD signal above the FM-AFM transition temperature is due to the canting of AFM ordered moments in the H = 7 kOe applied field [**79**].

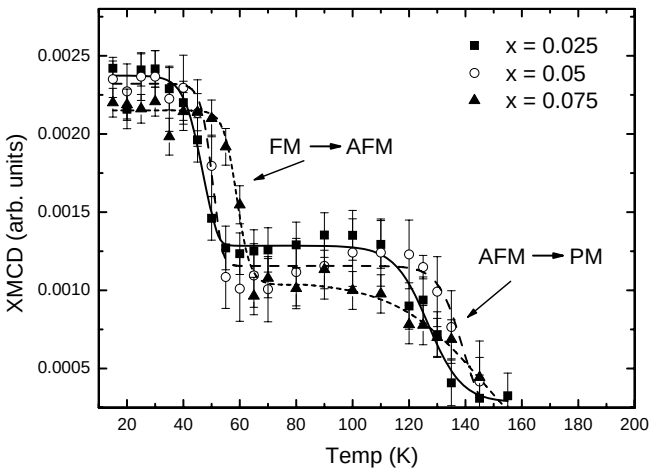

Figure 5.5. Temperature-dependent Gd L_3 -edge XMCD integrated intensities for $x = 0.025$, 0.05, and 0.075 measured at ambient-pressure in H = 7 kOe. Lines through data points are guides for the eyes.

The saturated XMCD values for FM and canted-AFM phases are henceforth labeled as M_s(FM) (for $T < T_c$) and M_s(AFM) (for $T_c < T < T_N$), respectively. These values are proportional to the net FM component in either phase. When both FM and AFM transitions are present (low pressure) T_c and T_N are defined as the local maxima in the data's first derivative for the corresponding transitions. Generally, this corresponds to a ~ 60 % reduction in magnetization relative to M_s(FM, AFM). At higher pressures where a single transition is observed T_c is defined where the XMCD is reduced by ~ 60 % from M_s(FM).

Figure 5.6(a)−(c) show temperature-dependent XMCD intensities measured at various applied pressures for $x = 0.025$, 0.05, 0.075, respectively. It can be seen that pressure initially induces a systematic increase in the saturation magnetization, M_s(FM), and Curie temperature T_c, while M_s(AFM) and associated Neẽl temperature $T_N \sim 130$ K remain nearly unchanged. At larger pressures, the intermediate AFM phase is no longer present and the data display a single

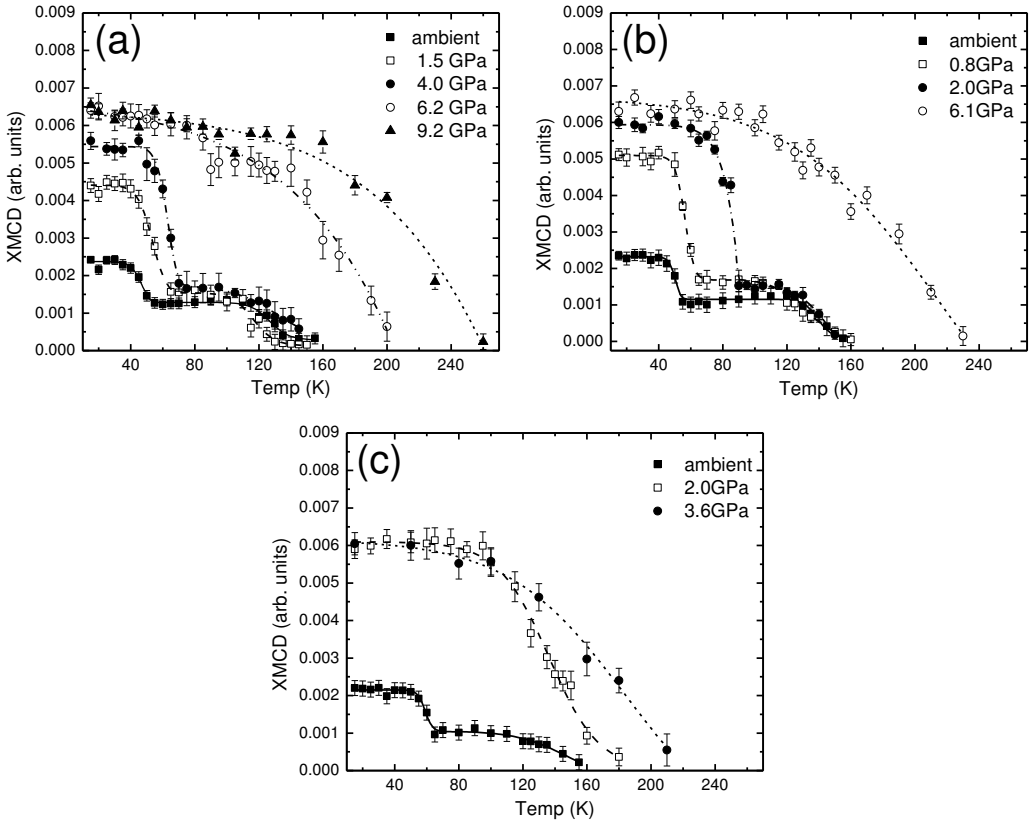

Figure 5.6. Temperature-dependencies of integrated XMCD intensities for (a) $x = 0.025$, (b) $x = 0.05$, and (c) $x = 0.075$ at various applied pressures.

FM $\rightarrow$ PM transition with a pressure-enhanced T_c. This later behavior is also observed for $x = 0.125$ sample described in Chapter 4.

The pressure dependence of M_s(FM) for the three low x samples and for $x = 0.125$ (the latter taken from Ref. [**71**]) is summarized in Fig. 5.7 (a). All M_s(FM) data are for T = 17 K and H = 7 kOe. The pressure dependence of T_c and T_N for the three samples is summarized in Fig. 5.7 (b).

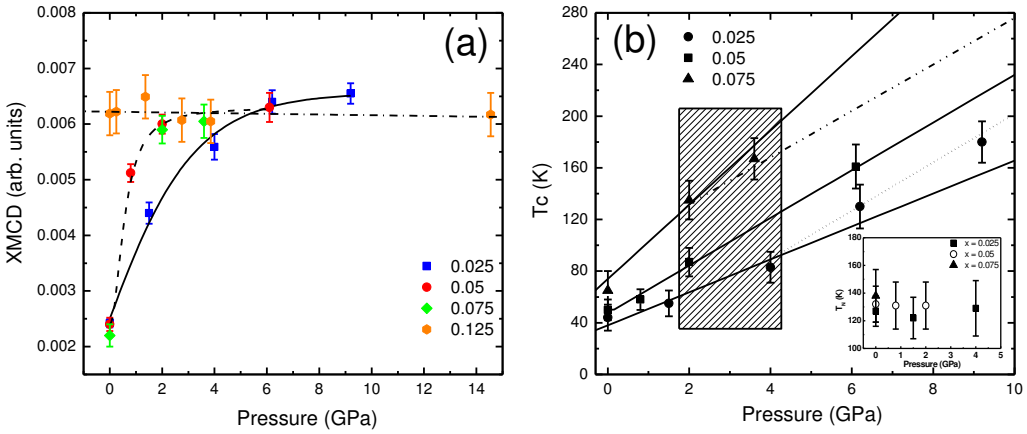

Figure 5.7. (a)Saturated magnetization, M_s (FM), as a function of pressure for x = 0.025, 0.05, 0.075 and 0.125. Data are obtained from integrated XMCD intensities at T = 17 K. (b)The pressure dependence of T_c and T_N (inset figure) for x = 0.025, 0.05, and 0.075 samples. Dashed lines correspond to dT_c/dP = 1.85 K kbar^{-1}, close to the dT_c/dP = 1.2−1.5 K kbar^{-1} values found for higher-x 0.125 and 0.375 samples. The shadowed area indicates pressures below (above) which an inhomogeneous (homogeneous) magneto-structural ground state is present at low temperature.

5.4. Discussion

The presence of a significant volume fraction of O(II) phase (50 %) for x = 0.025 (Fig. 5. 3(c)) at H = 0 and T = 17 K is due to the incomplete AFM-O(II) to FM-O(I) phase transition in this sample on cooling. The presence of both FM-O(I) and AFM-O(II) phases in the ground state at ambient pressure is a result of the close proximity in the total energy of these phases at low x [**80**]. The mixed-phase nature of the sample can be directly associated with the irreversible behavior observed in FC and ZFC SQUID measurements for x = 0.025, 0.05, and 0.075 samples (Fig. 5.2) since an applied magnetic field stabilizes the FM-O(I) phase. The larger irreversibility

occurs for $x = 0.025$, which has the largest AFM fraction. The strong irreversibility between FC and ZFC magnetization data decreases with x (Fig. 5.2) as the fractional volume of the AFM-O(II) phase decreases (Fig. 5.3). This strong irreversibility is nearly absent in $x = 0.125$ and $x = 0.5$ samples which show pure Gd_5Si_4-type O(I) phase in the ground state [**19, 29**]. The results show that the presence of the AFM component is responsible for the reduced M_s(FM) seen in $x = 0.025$, 0.05, and 0.075 samples. Increasing Si content stabilizes the FM-O(I) phase at the expense of the AFM-O(II) phase, with M_s(FM) reaching saturation at $x \sim 0.125$. The low M_s(FM) obtained for the three low x samples can be thought of as due to compositional frustration where FM and AFM components coexist within the sample volume. This behavior is strongly x-dependent for $0 < x \leq 0.075$ and disappears between $x = 0.075$ and $x = 0.125$.

The temperature-dependent XMCD intensities shown in Fig. 5.5 show that T_c increases with Si-doping ($x = 0.025$, 0.05, 0.075) at an estimated rate $dT_c/dx \sim 4.2$ K Si%$^{-1}$. This is in agreement with the 5.0 K Si%$^{-1}$ estimated from the phase diagram [**5, 11**]. Additionally, the $T_N \sim 130$ K found by XMCD is nearly independent of x, also in agreement with previous findings [**23, 25**]. The systematic increase in low-temperature magnetization with increasing x observed in the low-field (H = 50 Oe) SQUID measurements (Fig. 5.2) is not evident in the high-field (7 kOe) XMCD measurements. The stronger 7 kOe applied field results in the low temperature XMCD signal including contributions from both FM-O(I) and canted AFM-O(II) phases. These contributions have opposite x-dependencies, the FM-O(I) increasing with x but the AFM-O(II) decreasing with x. This compensation results in a much weaker x dependence of the low-temperature magnetization in the high-field XMCD measurements.

Nevertheless, one can quantitatively estimate the true x-dependent FM-induced XMCD signals by subtracting the FM fraction from Fig. 5.3(c) at H = 7 kOe. For example, FM phase is

found to be $\sim$ 65 % and $\sim$ 83 % with H = 7 kOe for $x = 0.025$ and 0.05, respectively. Since the XMCD signals of these two samples are similar at low temperature, it gives rise to a $\sim$ 20 % increase in true FM-induced XMCD. This value is in fair agreement with the SQUID measurements shown in Fig. 5.2, where a 30 % increase in FM order is found from $x = 0.025$ to $x = 0.05$ with H = 50 Oe at low temperature.

The low-temperature magnetization of the low-x samples at ambient pressure is reduced relative to the values achieved under high pressure (Figs. 5.5 and 5.6). This behavior is different than what was reported previously for $x = 0.125$, 0.5 samples [**63, 79**] where pressure, much like Si doping, enhances T_c but does not affect the saturation magnetization. Here, pressure increases both T_c and the net FM moment at low temperature. After the saturation magnetization reaches values typical of fully ordered FM compounds such as $x = 0.125$ and $x = 0.5$ an additional increase in pressure only causes an increase in T_c without further changes in M_s(FM). The different behavior of low-x and high-x samples is due to the presence of an AFM-O(II) phase in the ground state of low-x samples. Pressure transforms the AFM phase into a FM phase [**29**] and M_s(FM) increases accordingly. As shown in Fig. 5.7 (a), applied pressures of $\sim$ 5.0, 3.0, and 2.0 GPa are needed to fully convert the low-x, inhomogeneous AFM/FM samples [low M_s(FM)] into a homogeneous FM [large M_s(FM)] phase for $x = 0.025$, 0.05 and 0.075, respectively.

A pressure-induced AFM $\rightarrow$ FM transition is known to occur in Gd_5Ge_4, as originally reported by Magen et al. [**29**]. It is shown that the AFM-O(II) structure featuring magnetically disconnected Gd-containing slabs can be transformed into a FM-O(I) phase at a pressure P $\sim$ 1 GPa. Pressure reduces the lattice volume and causes the reforming of Ge-Ge bonds connecting Gd-slabs leading to emergence of FM order. Similarly, Pecharsky et al. reported [**20**] that this AFM $\rightarrow$ FM transition can be induced by magnetic fields where a 93 % FM volume fraction

is observed for H = 35 kOe. Our field-dependent (Fig. 5.3 (c)) and high-pressure (Fig. 5.7 (a)) results are consistent with these studies, suggesting that the pressure-induced increase in FM interactions within the inhomogeneous AFM/FM ground state (the three low-x samples) is qualitatively similar to what is observed in Gd_5Ge_4. However, in Gd_5Ge_4, the pressure- and field-induced AFM $\rightarrow$ FM transitions are 1^{st} order [**20, 29**] while field- and pressure-induced transitions in the mixed phase of the low-x samples appear sluggish, requiring significantly larger pressures and fields (Fig. 5.3 (c) and Fig. 5.7 (a)). In what follows the possible reasons for this behavior are addressed.

The AFM $\rightarrow$ FM transition in $Gd_5(Si_xGe_{1-x})_4$ is coupled to martensitic-like structural change [**14, 19, 23**] which can occur rapidly under the presence of an effective stress. However, the growth of the martensitic phase has to be along the habit plane [**82**] which allows the occurrence of macroscopic shape deformation; e.g. in our case, the habit plane is the $\vec{a}$-axis along which the atomic displacements during the breaking and reforming of Ge-Ge bonds connecting Gd-slabs take place [**14, 19, 23**].

However, the growth of the martensitic phase together with the concomitant appearance of FM ordering will be retarded by defect-rich interfacial boundaries as has been reported in surface-related studies [**83**]. This type of defect-rich boundary is bound to exist in an inhomogeneous AFM(O(II))/FM(O(I)) phase which bears large structural misfit, acting as barrier to hinder the growth of the FM-O(I) phase under applied pressure or field, leading to the sluggish behavior seen in Fig. 5.3(c) and Fig. 5.7 (a). Obviously, other details of a sample's microstructure will also play a role in determining the dynamics of the phase transition.

Alternatively, the sluggish nature of the pressure- and field-induced transition in the low-x samples could be attributed to the existence of a glass-like state for low applied fields and

temperatures rendering the materials into a kinetically-arrested state [**84**]. For example, glass-like dynamics has been observed in Gd_5Ge_4 in the presence of a complex AFM structure [**85**]. This glassy state varies with T and H and was observed in Gd_5Ge_4 for H $\leq$ 2.5 T and T $\leq$ 30 K [**84**]. Within this H−T region the AFM $\rightarrow$ FM transition was found to be sluggish while a sharp, 1st order transition is recovered away from this H−T boundary. In samples with low Si content, the energy barrier between AFM-O(II) and FM-O(I) states may be lowered preventing formation of a highly metastable state. In such case a gradual transformation is expected instead of a sharp one. The irreversibility, however, suggests that the kinetic arrest is still present in these samples. The compositional disorder (uneven Si distribution through the lattice), phase coexistence, and complex magnetic structure create a highly frustrated system with multiple energy barriers, which may or may not be easily overcome by external influences.

Thus, it is remarkable that applied pressure restores nearly full FM-O(I) order at the expense of reducing the fractional volume of the AFM-O(II) phase. The pressure-induced lattice contraction enhances intra- and inter-layer Gd-Gd indirect FM exchange interactions. Recently, spin-dependent hybridization between Gd 5d and Si 3p (Ge 4p) states was reported to change dramatically at the magneto-structural transition affecting the overlap between Gd 5d states and the strength of indirect FM exchange [**73**]. A volume reduction with pressure results in band broadening and a related increase in the overlap between Gd 5d states resulting in enhanced long-range indirect Ruderman-Kittel-Kasuya-Yoshida (RKKY) exchange coupling [**77**]. The lower total energy of the FM-O(I) phase versus the AFM-O(II) phase for contracted lattices is the driving force for the pressure- and Si doping (x)-induced transition from an inhomogeneous AFM/FM state into a nearly homogeneous FM state.

Since the AFM-O(II)/FM-O(I) ratio decreases with x (Fig. 5.3) the pressure needed to achieve a homogeneous FM-O(I) ground state also decreases with x (Fig. 5.7 (a)). We note that, while both M_s (FM) ($T \leq T_c$) and T_c increase with pressure, M_s (AFM) ($T_c < T < T_N$) and T_N are only weakly dependent on pressure (Figs. 5.6(a)−6(c)). This is consistent with previous reports on Gd_5Ge_4 [**29**] and $Gd_5(Si_{0.125}Ge_{0.875})$ [**79**], where a much weaker pressure dependence is reported for T_N than for T_c. Pressure increases the fractional volume of the FM state in the mixed ground state ($T \leq T_c$) at the expense of the AFM phase but does not significantly affect the AFM -O(II) structure that is energetically favorable at higher temperature ($T_c < T < T_N$). At small enough volumes (high pressures or $x > 0.2$) the FM-O(I) phase is stabilized to higher T and the AFM-O(II) phase is no longer present.

The ability of pressure and Si-doping to restore a homogeneous FM ground state in the low-x samples confirms the previously established concept [**28, 79**] that a unit cell volume reduction, either through Si doping or applied pressure, enhances the FM exchange interactions and leads to enhanced T_c. However, in the previous pressure studies [**72, 79**] it was reported that dT_c/dP = 1.2−1.5 K kbar^{-1} for samples with $x = 0.125$ and $x = 0.375$; i.e., at these higher doping levels ($0.125 < x < 0.5$) the rate at which T_c increases with pressure is nearly independent of Si concentration provided that applied pressures are small enough that a structural phase transition from monoclinic to orthorhombic-O(I) is not induced at room temperature [**79**]. We argued that this is due to the fact that the strength of ferromagnetic interactions is mostly determined by lattice volume and hence dT_c/dP is dictated by lattice compressibility. In contrast, the low-x samples show markedly different behavior. At low pressures $P \leq 4$ GPa, dT_c/dP shows strong x dependence, with values of 1.28, 1.85, and 2.87 K kbar^{-1} obtained for $x = 0.025$, 0.05, and 0.075, respectively (solid lines in Fig. 5.7 (b)).

This could be interpreted as a result of different compressibilities for these low-x samples associated with the x-dependent fractional volumes of AFM-O(II) and FM-O(I) phases in the mixed state. However, if these samples were to have different compressibilities, one would expect the lowest x sample with the largest O(II) fractional volume and largest unit-cell volume to have the largest compressibility and the largest dT_c/dP, while the opposite is observed. On the other hand the martensitic-like, magento-structural transition AFM-O(II) $\rightarrow$ FM-O(I) is expected to be affected by strain. The gradual reduction in interfacial O(II)/O(I) volume in the mixed-phase, low-x samples, in going from $x = 0.025$ to $x = 0.075$ may explain the observed changes in dT_c/dP since the sample with largest nominal strain ($x = 0.025$) displays the slowest pressure-induced increase in T_c. One would expect that once a homogeneous FM-O(I) state is reached for P $\geq$ 4 GPa the expected values of dT_c/dP would be restored for all samples [**79**]. Although the limited number of data points in Fig. 5.8 precludes us from making a definitive statement, the available data are consistent with this expectation (dashed lines in Fig. 5.7 (b) correspond to dT_c/dP = 1.85 K kbar^{-1}).

Finally a comparison of dT_c/dP in Gd_5Ge_4, low-x samples (x = 0.025, 0.05, 0.075), and high-x samples (x = 0.025, 0.05, and 0.075) is presented. The largest dT_c/dP of $\sim$ 4.8 K kbar^{-1} is obtained for Gd_5Ge_4, followed by the low-x samples (1.28, 1.85, and 2.87 K kbar^{-1} for x = 0.025, 0.05, and 0.075, respectively) while the smallest dT_c/dP of 1.2$-$1.5 K kbar^{-1} is obtained for $x = 0.125$ and 0.375. In Gd_5Ge_4, the pressure-induced first-order transition from AFM-O(II) to FM-O(I) involving the reforming of Ge-Ge bonds connecting Gd slabs leads to a sudden stabilization of the FM state. For the mixed-phase low-x samples discussed here, the ability of applied pressure to stabilize a homogeneous FM state is strongly dependent on the level of Si doping, i.e., on the AFM-O(II)/FM-O(I) ratio. When the FM-O(I) phase is fully developed for x

= 0.125 and 0.375 samples (or for P $\geq$ 4 GPa in low-x samples), pressure enhances FM ordering at the lowest rate. The drastic change in dT_c/dP behavior, which increases in low-x samples from 0.025 to 0.075 but decreases to become constant in higher-x samples ($0.1 < x < 0.5$) and in low-x samples at high pressures is further evidence that the magnetism in the low-x region of the phase diagram is influenced by Si doping in a way that is fundamentally different than what takes place in the high-x region of the phase diagram.

5.5. Modified phase diagram of $Gd_5(Si_xGe_{1-x})_4$

According to the results presented in this chapter, the phase diagram (Fig. 1.5) needs to to be modified. Fig. 5.8 and 5.9 show the modified magnetic and structural phase diagram, respectively, updated with the coexisting AFM(O(II))-FM(O(I)) phase region at low Si-doping region ($0 < x \leq 0.75$) and low temperature. In this region, materials display magneto-structural inhomogeneity (phase coexistence), so the magnetization is reduced compared to that of $x \geq 0.125$ where single phase behavior is found. One possible explanation for the coexisting AFM(O(II))-FM(O(I)) phase region is an incomplete AFM(O(II)) $\rightarrow$ FM(O(I)) transition upon cooling. Since at low x AFM(O(II)) and FM(O(I)) phases have close proximity in their total energies (the FM-O(I) phase being lower) it is possible that variations in microstructure (e.g. local strain or defect density) may stabilize the AFM phase in certain regions of the sample to lower temperatures, resulting in the observed coexistence. Alternatively, the mixed-phase behavior may be due to variations in sample composition at the atomic scale (Si content). XRD shows that the lattice parameters of the low-x ($0 < x \leq 0.75$) samples linearly decrease with Si content (XRD, Fig. 5.3). However, being XRD a probe of the average structure, this only proves that Si incorporates

into the lattice in a manner proportionately to the nominal Si concentration. This does not prove that the Si concentration is homogeneous at the atomic scale.

If Si atoms are not homogeneously distributed at the atomic-scale, one might expect that phase separation will take place with Si-rich and Ge-rich regions nucleating FM-O(I) and AFM-O(II) phases, respectively. In this scenario atomic scale variations in Si composition result in phase separation, while in the previous scenario of an incomplete AFM'FM transition a similar inhomogeneous, mixed phase results from variations in local strain and/or defect concentration (microstructure). We note that it is possible to distinguish between these two scenarios by directly probing the degree of compositional homogeneity at the atomic, nano and micro scales using a combination of element-specific real space mapping techniques such as energy dispersive x-ray spectroscopy (EDX) [**87**] in the electron microscope (SEM/TEM) or x-ray fluorescence microprobe imaging [**88**], together with XAFS and diffuse-scattering techniques. These will be discussed further in Chapter 7.

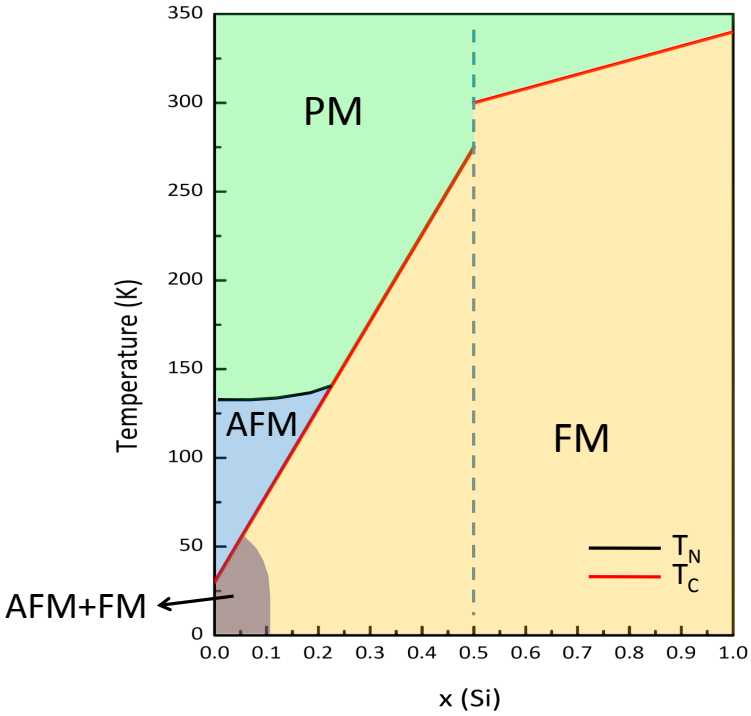

Figure 5.8. Modified magnetic phase diagram of $Gd_5(Si_xGe_{1-x})_4$. Red line marks T_c of the corresponding composition (x). Compared to Fig. 1.5, the modified phase diagram includes coexisting AFM-FM phases at low Si-doping region ($0 < x \leq 0.75$) and low temperature. Precise determination of the phase boundary requires additional measurements beyond the three Si concentrations probed in this thesis.

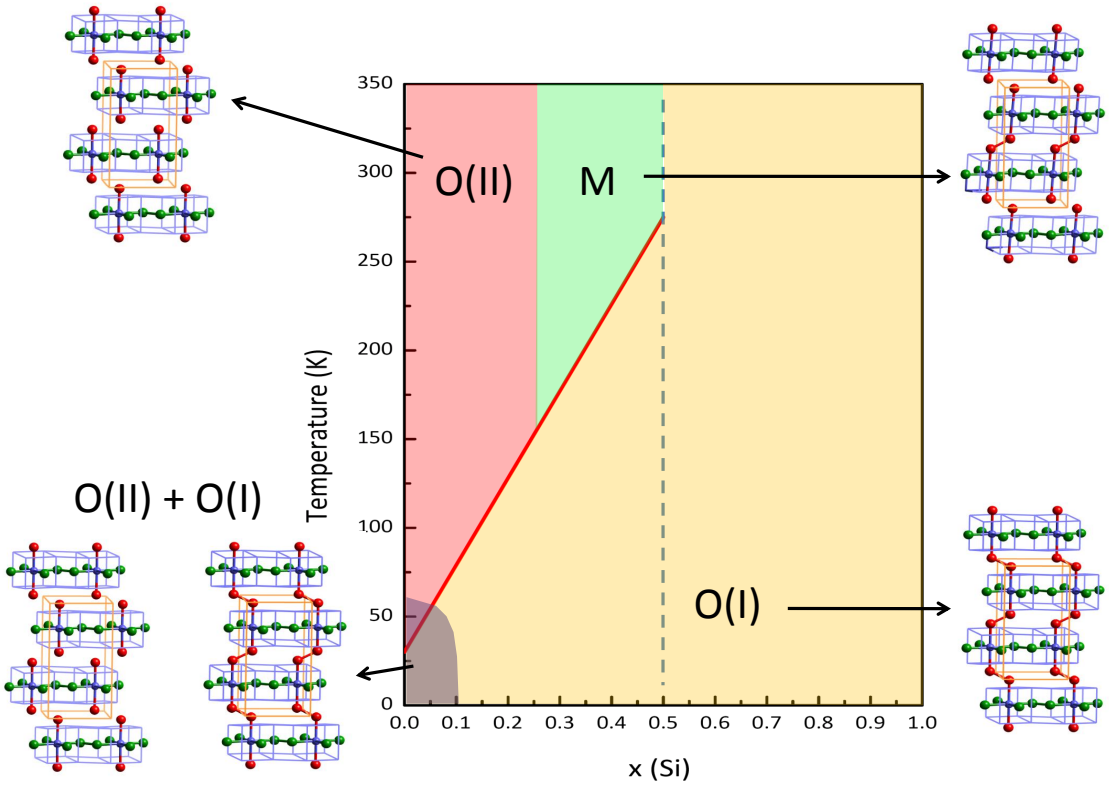

Figure 5.9. Modified structural phase diagram of $Gd_5(Si_xGe_{1-x})_4$. The low Si-doping region ($0 < x \leq 0.75$) at low temperature is structurally characterized with the coexisting O(II)-O(I) phase. Precise determination of the added phase boundary requires additional measurements beyond the three Si compositions measured in this thesis.

5.6. Conclusion

The magnetic and structural properties of low-x (0.025, 0.05, and 0.075) Ge-rich $Gd_5(Si_xGe_{1-x})_4$ compounds were probed with element-specific XMCD measurements in a diamond-anvil cell, together with SQUID magnetometry and x-ray diffraction measurements. While the small Si-doping levels lead to the emergence of partial FM order, the ground state is inhomogeneous due to an incomplete AFM $\rightarrow$ FM transition on cooling. This inhomogeneous ground state features a reduced low-temperature magnetization accompanied by strong irreversibility in FC and ZFC magnetization data, indicative of a glassy behavior. Applied pressure reduces the lattice volume and enhances the FM exchange interactions, restoring a nearly fully-ordered FM state. Although T_c increases with pressure as previously observed in high-x samples [**28, 79**], dT_c/dP is strongly x-dependent for low-x samples in contrast with the nearly x-independent dT_c/dP found for $0.125 \leq x \leq 0.5$ [**72**]. The results suggest that the emergence of FM from within the AFM phase of Gd_5Ge_4 cannot simply be described by a volume effect and that the presence of an inhomogeneous magneto-structural ground state ought to be considered in order to explain the rather complex low-x region of the phase diagram of these materials. Finally, the phase diagram is also modified by adding the coexisting AFM(O(II))-FM(O(I)) phase region at low Si-doping region ($0 < x \leq 0.75$) and low temperature. The examination of compositional homogeneity of the low-x samples using element-specific and real space mapping is also suggested.

CHAPTER 6

Quantitative discrepancy between Si-doping and pressure effects upon $Gd_5(Si_xGe_{1-x})_4$ compounds

6.1. Introduction

In the last two chapters, it has been demonstrated that pressure is similar to Si-doping in enhancing the FM order of $Gd_5(Si_xGe_{1-x})_4$ alloys. The enhancement of FM order could be seen in the pressure-induced, linear increase of T_c ($0.125 \leq x \leq 0.5$), and in the removal of the magneto-structural inhomogeneity characterized by fully restored magnetization for low-x samples ($0 < x < 0.1$), as described in Chapter 4 and 5, respectively. Although both pressure and Si-doping enhance the FM order by contracting the lattice, the extent of their similarities has not been rigorously validated to date [**72, 79**]. While pressure simply contracts the lattice macroscopically, doping Si into the alloys can result in (i) non-random atomic substitution within the three in-equivalent Si(Ge) sites [**14, 24**] that may lead to anisotropic lattice contraction, (ii) volume-independent modifications to the electronic structure due to different wave functions of Si $3p$ and Ge $4p$ states, which may mediate magnetic interactions differently via nonmagnetic(Si(Ge))-magnetic(Gd) orbital hybridization, and (iii) atomic substitution-induced microscopic local structure effects that may influence magnetic ordering but hard to observe by structural probes of the average lattice. These factors could influence the magnetic interactions in a more complex way both within and between the Gd-containing slabs, hence increasing the FM interactions differently than pressure. The quantitative correspondence between Si-doping

and pressure is critically important in $Gd_5(Si_xGe_{1-x})_4$ because of a long-standing debate on whether the materials properties, in particular T_c of these alloys, are *solely* macroscopically volume-dependent since their re-discovery in 1997 [**18, 21, 24**]. Despite some efforts aimed at this problem and some reports of higher efficiency of Si-doping than pressure in increasing T_c [**28, 79**], solid and direct evidence hasn't been reported yet.

This unsolved issue has important consequence of the magnetic refrigeration technology based on $Gd_5(Si_xGe_{1-x})_4$ alloys, where Si-doping is only able to enhance T_c up to 275 K, i.e. close to but not above room temperature without losing the GMCE [**14, 24**]. A standard route for more efficient T_c enhancement through doping is unclear due to incomplete understanding of other doping-induced effects in addition to the macroscopic volume contraction. In this chapter, a study is presented comparing the rate of increase in T_c with Si-doping and pressure for a given unit cell volume contraction. This allows us to compare the volume-effects in both cases and hence contrast this with other factors, such as anisotropic lattice constant change or local structure effects that may affect increase in T_c. This also allows for a quantitative comparison, beyond previous qualitative studies. This study facilitates the understanding of the core essence of doping-induced FM increase in $Gd_5(Si_xGe_{1-x})_4$ alloys, which is valuable to establishing a formula in seeking other promising doping elements that may enhance T_c more effectively and eventually enable a R. T. operational magnetic refrigerator.

6.2. Experiment

Polycrystalline samples of $x = 0.125$ and $x = 0.5$ in $Gd_5(Si_xGe_{1-x})_4$ formula were used in this work. Samples were prepared at Ames Lab as described in Ref. [**18**]. The experimental data were collected at different beamlines of the Advanced Photon Source, Argonne National

Laboratory. XMCD measurements were carried out at beamlines 4-ID-C and D at the Si (Ge) K ($1s \rightarrow 3(4)p$) transition at 1.839 (11.103) keV edges with applied magnetic field (H) of 4T along x-ray photon wave-vector, in order to probe the magnetic polarization of Si $3p$ (Ge $4p$) induced by Gd $5d$ conduction electrons. Due to its orbital and elemental specificity, XMCD allows us to probe the relevant wave functions in mediating the FM coupling through Si $3p$ (Ge $4p$)- Gd $5d$ hybridization over three Si(Ge) sites. Gd L_3 -edge ($2p_{1/2} \rightarrow 5d$ transition at 7.243 keV) XMCD was probed at beamline 4-ID-D through perforated anvils in an asymmetric DAC with H = 0.7 T in order to obtain the pressure-induced T_c increase as described in the last two chapters [**63, 72, 79, 86**]. Si and Ge K -edge XAFS spectra were collected to probe the local structure of the selected atoms at beamlines 4-ID-C and D, respectively.

High-pressure angle-dispersive experiments using a Mao-type symmetric DAC [**89**] were carried out at 16-ID-B to track the pressure-induced structural change, and also monitor the change in lattice constants (Fig. 6.4). The collected two-dimensional diffraction rings were integrated with FIT2D program [**59**] into diffraction pattern of intensity versus 2θ (Fig. 2.9(d)). Rietveld refinement [**60**] was used to determine crystallographic structures and lattice constants (Fig. 6.2). FEFF6.0 theoretical standards [**66**] and IFEFFIT package [**67**] were used to fit the collected Si(Ge) K -edge XAFS spectra, including the contributions from the first two atomic-shells and assigning independent compressibilities as variables for Si-Si, Si-Gd, Si-Ge, and Ge-Gd bonds. Details of the fitting process are described in Appendix A. Si(Ge) K -edge XMCD and x-ray absorption near edge structure (XANES) were simulated by FDMNES code [**90**] and compared with experimental data, in order to both theoretically and experimentally monitor Si $3p$ (Ge $4p$)-Gd $5d$ hybridization. Details of the calculations are present in Appendix B.

Local spin density approximation calculations with the onsite Coulomb parameter (LSDA + U) approach [**91, 92**] was employed in simulating the $x = 0.125$ sample to highlight the electronic structure modifications upon local structure change. The calculations have been performed using the scalar relativistic version (which includes the mass velocity and Darwin correction terms) of the LSDA+U method implemented in the tight binding linear muffin-tin orbital (TB-LMTO) scheme [**93, 94**]. In these calculations, the density of state (DOS) of Gd $5d$ is the average of all Gd ions located within the slabs and the results were obtained with Si located at T_2 sites considered as the preferential site [**95, 96**].

6.3. Results

Figure 6.1 shows the XRD pattern of selected pressure points for $x = 0.125$ sample marked with corresponding phases. The results confirm the fact that pressure is able to yield a O(II) $\rightarrow$ M phase transition as Si-doping does. The detail of the mixed-phase fitting is highlighted in Fig. 6.2, where a 75 % M - 25 % O(II) mixture found at P = 7 GPa is presented and the sum of the two phases agrees fairly well with the experimental one. Fig. 6.3 describes the details of pressure-induced changes in lattice constants below and above the phase transition ($\sim$ 5 GPa) and its inset shows the volume fraction of M phase as a function of applied pressure. The result suggests that the O(II) $\rightarrow$ M transition is completed at P = 8 GPa. In order to subtract the volume effects, the pressure scale of Fig. 6.3 was converted into unit cell volume. The converted diagram is displayed in Fig. 6.4, where it shows the volume-dependence of lattice constants reduction in percentage resulted by pressure (left panel) and Si-doping (right panel, taken from Ref. [**97**]). The main panel of pressure shows data up to 5 GPa (840 Å^3) before the O(II) $\rightarrow$ M transition takes place, for the purpose of having a clear comparison of dT_c/dV (V defined as unit

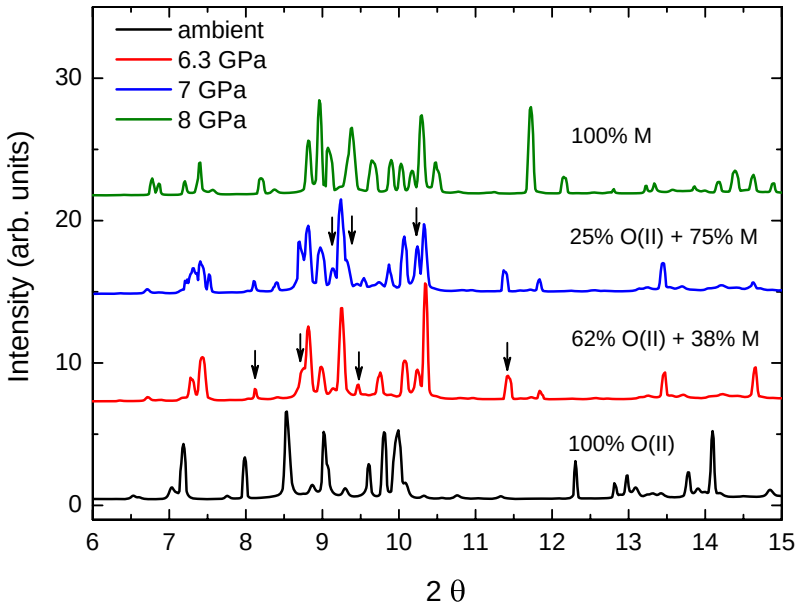

Figure 6.1. Comparison of XRD at selected pressure points for $x = 0.125$. The fitted fractional volumes in the mixed-phase region are indicated. The arrows indicate the minority M phase at P = 6.3 GPa and O(II) phase at P = 7 GPa

cell volume) with Si-doping. Its inset figure shows the change in three lattice constants in the M phase for continuous volume contraction down to 790.7 $Å^3$ (8 GPa). Si-doping panel shows data up to $x = 1.0$ sample (854 $Å^3$), displaying O(II), O(II)+M, M, and O(I) phase according to Ref. [**97**]. The volume-dependent T_cs are plotted as independently determined by XMCD (pressure) and magnetometer SQUID (Si-doping) [**79, 97**]. Since the high-pressure XRD data were collected at R.T., the magnetic phases of the material is in the paramagnetic phase (PM) at all pressures.

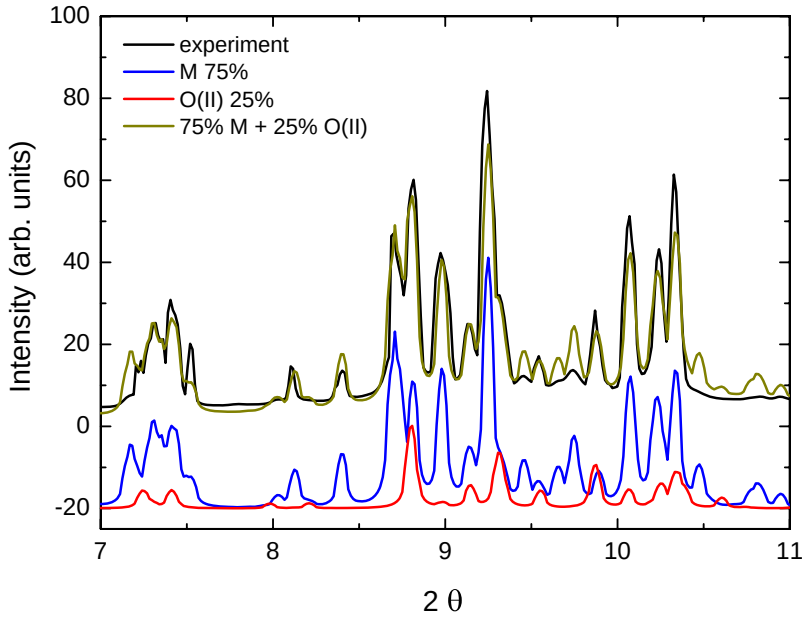

Figure 6.2. XRD pattern of $x = 0.125$ sample at P = 7 GPa together with results of Rietveld refinement using a mixture of O(II) and M phases. Quality of fit parameters are $R_p = 19.57$ %, $R_{wp} = 22.32$ %, $R_{Bragg} = 17.14$ %

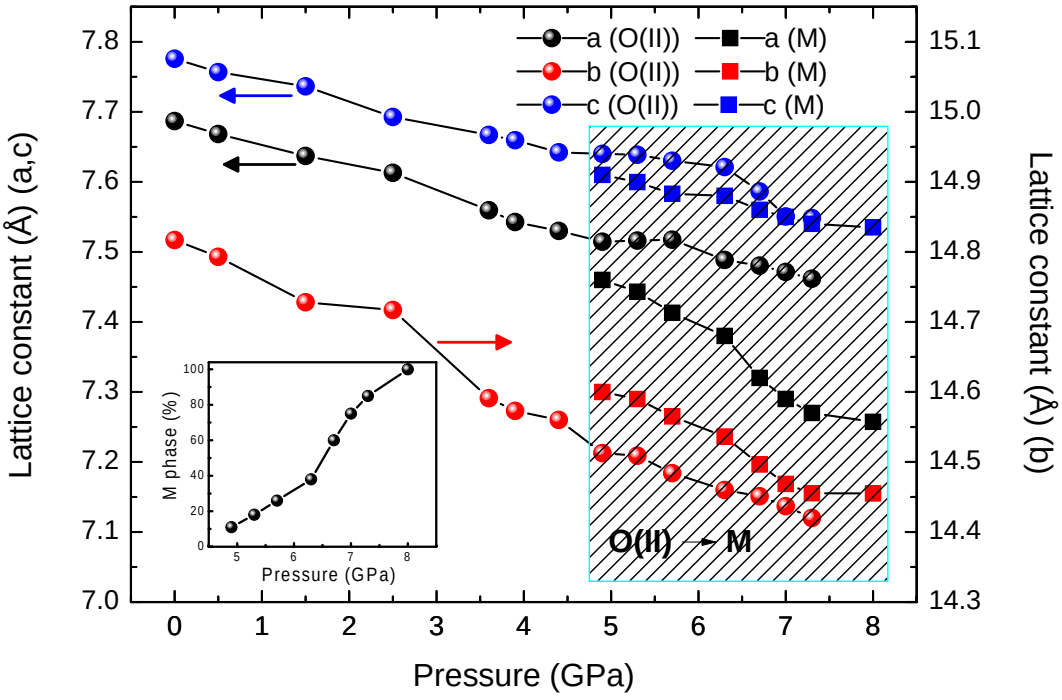

Figure 6.3. Pressure-dependence of three lattice constants from ambient to 8 GPa for the $x = 0.125$ sample. $\vec{a}$ and $\vec{c}$ are shown in the left-vertical axis and $\vec{b}$ is shown in the right-vertical axis. Shadowed area highlights the O(II) (circle) $\rightarrow$ M (square) phase transition range where both O(II) and M phases coexist. Inset figure displays the pressure-dependent volume fraction (in %) of M phase from 5 to 8 GPa.

In order to address the importance of local structure effects that may contribute to dT_c/dV (Fig. 6.4) besides macroscopic volume contraction, XAFS measurements of Si(Ge) at ambient condition were carried out. Fig. 6.5 shows the Fourier transform (FT) of Si and Ge K -edge XAFS for the $x = 0.5$ sample probed at 10 K. At such temperature, the material displays a slab-connected FM-O(I) state. Benefited by its sensitivity to local structure, XAFS reveals that all Si covalent bonds (Si-Si, Si-Gd) display a significant contraction, while Ge's local environment displays a lattice expansion, as presented in Table 6.1. Here, XAFS probes the nature of the average of the three sites. For $x = 0.5$ sample, the material exhibits a nearly random distribution among the three Si(Ge) sites [**19**]. Hence, the collected XAFS provides the microscopic nature contributed nearly equally from each site. The nearly random atomic distribution can also be seen by the similar features shown in Si and Ge K -edge XAFS. The comparison for theoretical and experimental Si(Ge) K -edge XANES and XMCD (inset figure) at various pressures and T = 10 K for $x = 0.5$ sample, is illustrated in Fig. 6.6. They are used to highlight the difference between pressure- and local structure- induced orbital hybridization of the selected atoms.

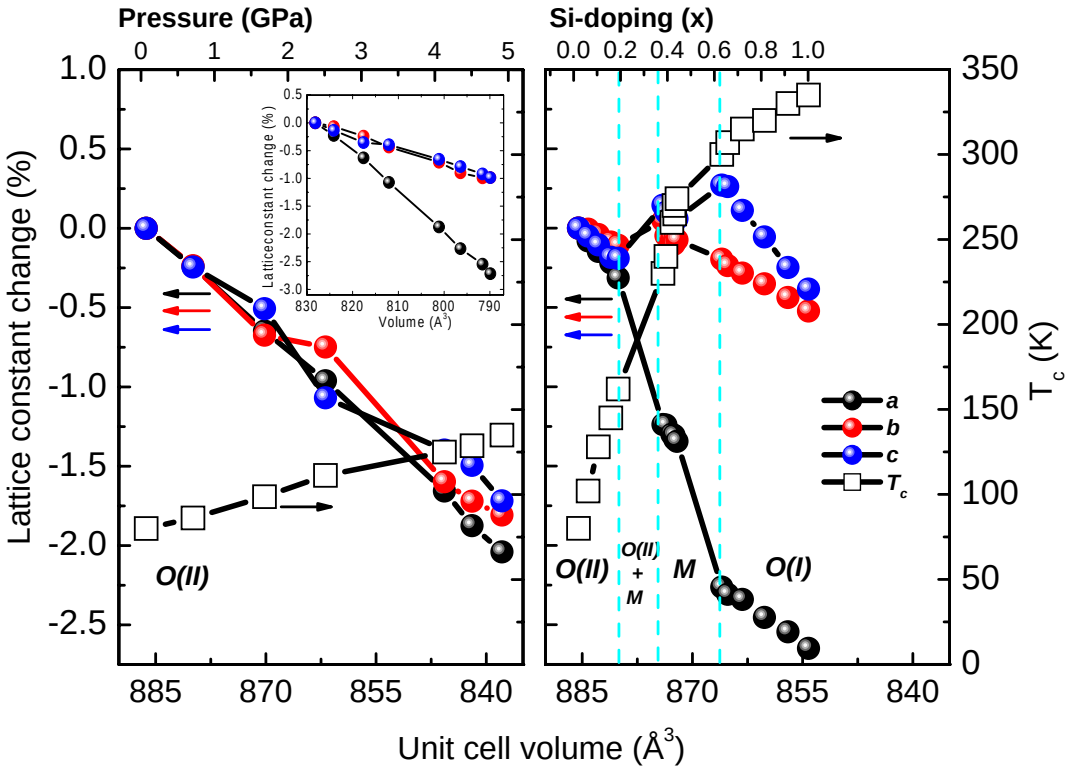

Figure 6.4. Lattice constant change and related volume change with pressure (left) and Si-doping (right)(units read from left-vertical axis) and T_c (opened squares, units read from right-vertical axis) for the $x = 0.125$ sample. The inset in the pressure panel depicts the pressure-induced volume change in the M phase. Pressure data were converted from Fig. 6.3. Si-doping data were taken from Ref. [**97**] and the diagram is marked with different phases by dashed lines. dT_c/dP with pressure and Si-doping are obtained from XMCD [**79**] and SQUID magnetometer [**25**], respectively. The scale of the unit cell volume is fixed for both main panels for a clear dT_c/dV comparison. The smallest volume shown in the pressure panel ($\sim$ 837 Å^3) is given by P = 5 GPa, and the material's structure remains as O(II) within this pressure range. For Si, the smallest volume is $\sim$ 852 Å^3 when x reaches 1.0.

6.4. Discussion

In Fig. 6.3, it is evident that the pressure-induced phase transition takes place at $\sim$ 5 GPa, in excellent agreement with Ref. [**79**]. In the O(II) region, the three lattice constants display a nearly linear contraction, which can be further confirmed in the pressure panel of Fig. 6.4 given in percentage scale. A notable feature is that pressure contracts the lattice anisotropically in the M phase (larger compressibility along $\vec{a}$-axis), whereas an isotropic compression is seen in the O(II) both in the pure and mixed phase regions. Similar behaviors can be obtained with Si-doping as shown in the right panel of Fig. 6.4. This suggests that macroscopically, pressure and Si-doping contract the lattice in a similar way. This supports the notion that the O(II) $\rightarrow$ M transition involves a martensitic-like transition which requires a significant shear displacement along the $\vec{a}$-axis [**14, 18, 19**].

Nevertheless, a much smaller volume contraction is needed for Si-doping to trigger and finish the O(II) $\rightarrow$ M phase transition. For example, it takes a volume reduction of $\sim$ 6 and $\sim$ 50 Å^3 for Si-doping and pressure, respectively, to drive O(II) into O(II)+M, respectively; and $\sim$ 5 and $\sim$ 42 Å^3 to complete the O(II)+M region, respectively. Besides, Si-doping is able to yield a dT_c/dV of 13.55 K Å^{-3} much larger than 1.2 K Å^{-3} yielded by pressure crossing O(II), O(II)+M and M phases, as illustrated in Fig. 6.4. The results indicate that although pressure and Si-doping are seemingly analogous to each other, the later exhibits a more effective volume contracting-induced phase transition and increase in T_c, with a factor of $\sim$ 8 and $\sim$ 11.3, respectively.

The sluggish process of pressure in modifying structures and increasing T_c is likely due to the uniform compression upon the lattice [**72, 79**]. Especially for FM order increase, pressure takes a macroscopic route to homogeneously increase the overlap between Gd 5d and Si 3p (Ge 4p) states and changes the magnetic interactions accordingly. This, however, is fundamentally distinct from

Si-doping which relies on the local chemical pressure as a result of atomic substitution upon the three inequivalent crystallographic sites, which should yield a more complex way in varying the magnetic interactions. Subtle magnetic transitions resulted from microscopic effects such as local lattice distortion [**49**] or bonding anisotropy [**98**] are commonly reported. In this case, Si substituting for Ge is expected to result in local structure adjustment hard to detect as it is in macroscopic probes of structure. In particular, these materials' FM exchange strength is critically related to the level of Gd $5d$ and Si $3p$(Ge $4p$) hybridization [**73**]. Any subtle local structural modifications either within or between slabs, are likely to vary the hybridization hence leading to notable change in the FM exchange throughout the system.

The hypothesis was validated by XAFS as shown in Fig. 6.5, where a local lattice contraction effect is obtained around Si atom with significant bond length reduction relative to those around Ge atoms (present in Table 6.1). This microscopic stress is of atomic-scale level and unable to relax macroscopically, as addressed in other related works on other systems [**99, 100**]. How this local contraction effect affects the FM order is addressed as follows.

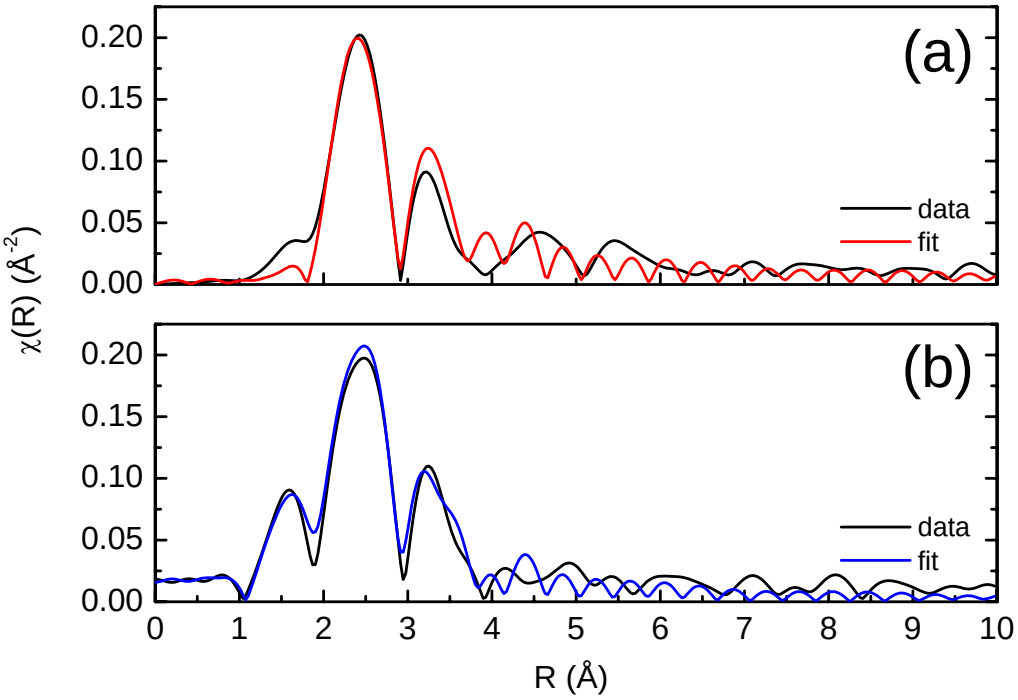

Figure 6.5. Magnitude of Fourier transform (FT) of Ge (top) and Si (bottom) K -edge XAFS spectra using the k = [2, 10] Å range for $x = 0.5$ sample at T = 10 K. The spectra were fitted using the crystal structure determined from XRD at 10 K.

Atom	interatomic distance		
Si	**Si - Si**	**Si - Ge**	**Si - Gd**
	-0.0395 ± 0.0074 Å	0.0012 ± 0.0013 Å	-0.031 ± 0.0182 Å
Ge	**Ge - Ge**	**Ge - Si**	**Ge - Gd**
	+0.083 ± 0.0021 Å	0.0012 ± 0.0013 Å	+0.004 ± 0.003 Å

Table 6.1. Si and Ge interatomic distances relative to those in the average structure determined by crystallography for $x = 0.5$ sample. The results only include contributions from the first two atomic shells around the selected Si and Ge atoms.

In Fig. 6.6, simulated and experimental XANES and XMCD (insets) spectra for Si and Ge K -edge are presented. Both Si and Ge display clear XMCD signal, indicating a spin polarized conduction band through Si $3p$ (Ge $4p$)-Gd $5d$ hybridization [**73**]. The most distinct feature between two elemental spectra is that, Si experimental XANES displays a much broader shoulder on the rising absorption edge together with a $\sim$ 5 times larger XMCD signal than Ge after edge-jump normalization. Interestingly, Si experimental XANES at ambient condition doesn't agree with the simulated result using lattice parameters at ambient condition, while it is more consistent with the simulation using lattice parameters of P = 7 GPa. This reveals important information that in terms of XANES and the related electronic structure of Si $3p$ conduction states, the local contraction is able to yield a chemical pressure (at ambient condition) comparable to that obtained by a very large macroscopic lattice compression resulted by applied pressure. For example, considering the contracted Si-Si and Si-Gd bonds, they give rise to 1 % and 1.5 % interatomic distance reduction, respectively. According to Eq. 3.2, this will result in a local volume reduction of $\sim$ 3 % around Si atom at ambient condition within the first two atomic shells.

Details of the estimation is described in Appendix A. This is in a close approximation to $\sim$ 1 % reduction for each axis with an applied pressure of $\sim$ 3 GPa. The results also suggest that

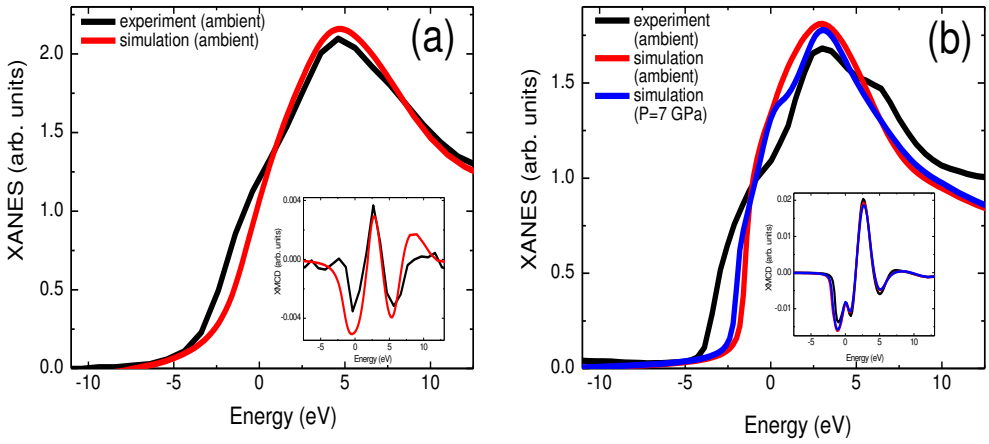

Figure 6.6. (a) Ge and (b) Si K -edge experimental and simulated XANES and XMCD (inset) results for $x = 0.5$ sample at T = 10 K. The simulation was conducted using the FDMNES code [**90**] using lattice parameters obtained by XRD (macroscopic) at ambient and P = 7 GPa condition. For Ge, theory and experiment show reasonable agreement. For Si, the experimental data feature a broadened shoulder distinct from the simulation, indicating a significant modification of local structure from average structure. This distinction is reduced when the lattice is artificially compressed (P = $\sim$ 7 GPa).

the broader shoulder of Si XANES is not due to its dissimilar wave-function of final p states than Ge's [**101, 102**], but refers to a stronger Si 3p-Gd 5d hybridization as a result of $\sim$ 0.03 Å contraction of Si-Gd bonds over all sites (Table 6.1).

The concept of local contraction and the correlation between microscopic and macroscopic volume contraction are schematically illustrated in Fig. 6.7. Although it is very difficult to quantify the true pressure exerted by local contraction merely by XANES, the unexpectedly large value of 7 GPa already demonstrates the fact that doping is able to generate tremendous atomic-scale stress in addition to macroscopic contraction, which is impossible to achieve with applied pressure alone. The enhanced Si 3p-Gd 5d hybridization generated by the local pressure

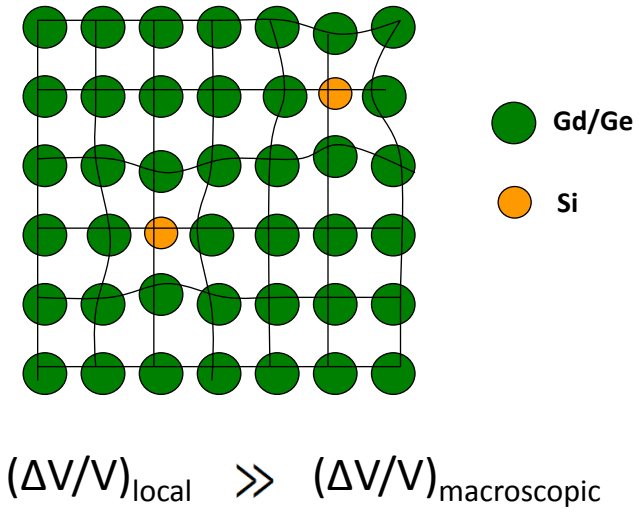

Figure 6.7. schematic illustration of the local contraction effect present in crystal lattice. The local structure around Si atoms is contracted as a result of atomic substitution (also see Table 6.1). It yields a local volume reduction much greater than the macroscopic one, particularly at low x.

consequently provides the best explanation why Si-doping increases T_c much faster than pressure. More importantly, it suggests that the local contraction plays a far more dominant role in increasing T_c than macroscopic contraction. This overthrows the concept prior to this work that macroscopic contraction is the major driving force for T_c increase in $Gd_5(Si_xGe_{1-x})_4$. In addition to $x = 0.5$ sample, the local contraction is also obtained in $x = 0.125$ sample, indicating that its existence is not a single compositional case.

Band structure calculations (LSDA + U, not shown here) with Si occupying T_2 site show that local lattice contraction can give rise to $\sim$ 9 % increase in spin splitting of Gd $5d$ DOS near Fermi level and result in $\sim$ 4 % increase in exchange interaction (J_{ex}). Si magnetic moment spin-polarized by Gd also increases from 0.06 to 0.09 μ_B/atom when the local contraction effect is accounted for. One should note that these results were established on low occupancy by Si of

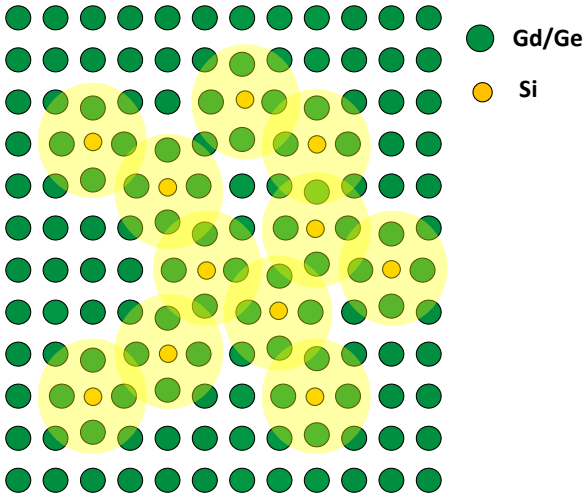

Figure 6.8. Illustration of FM percolation in $Gd_5(Si_xGe_{1-x})_4$. Each Si atom accompanied by local lattice contraction serves an efficient FM exchange pathway and the yellow circle represents its effective area. The FM percolation is triggered when the circled areas overlap with each other.

T_2 site only. Thus, a more pronounced increase in both J_{ex} and spin splitting of Gd $5d$ DOS is expected when the local contraction is performed on available Si sites. Over all, it is believed that the local contraction around Si atoms enables more efficient FM exchange pathway and assists the FM percolation as illustrated in Fig. 6.8, thus resulting in a faster emergence of and increase in the strength of FM order in $Gd_5(Si_xGe_{1-x})_4$.

6.5. Conclusion

This chapter presents an important study of the quantitative correspondence between Si-doping and hydrostatic pressure effects upon $Gd_5(Si_xGe_{1-x})_4$. Prior to this study, the understanding of their correspondence was confined in qualitative scope. The role of Si-doping in

increasing T_c has been misconceived for long as merely a result of macroscopic volume contraction because similar qualitative behaviors were obtained with Si-doping and pressure. In this study, a quantitative comparison between the two was examined by comparing their dT_c/dVs. Si-doping displays a much larger value than pressure with a factor of ~ 11.3, suggesting its higher efficiency in increasing the FM order. The results demonstrate an important observation of local contraction around Si atoms that yields a tremendous local chemical pressure that hasn't been found thus far. This effect results in more enhanced Si $3p$-Gd $5d$ hybridization which, in turn, is responsible for the faster T_c increase than with macroscopic volume contraction. The local contraction centered on Si dopants also plays a critical role in percolating the FM order with a filament network fashion. The study unveils the mystery of doping-induced FM increase in $Gd_5(Si_xGe_{1-x})_4$, as well as establishes a route for selecting suitable dopants to achieve higher operational temperature of the magnetic refrigerator.

CHAPTER 7

Summary and future work

7.1. Thesis summary

The principal accomplishment of this thesis is two-fold. First, a high-pressure (HP) setup using diamond anvil cell (DAC) and x-ray magnetic circular dichroism (XMCD) has been demonstrated. The DAC used in this thesis is able to generate pressures up to $\sim$ 1 Mbar (100 GPa), and the pressure can be calibrated $in-situ$ using either Cu XAFS or ruby fluorescence method. Thanks to the high brilliance of third generation synchrotron radiation coupled with focusing optics provided by the Advanced Photon Source, Argonne National Laboratory, XMCD can be collected through the DAC for absorption energy greater than $\sim$ 6 keV due to the use of perforated anvils which reduce absorption. This technique enables element- and orbital- specific probe of magnetism under high pressure, enabling studies of the intimate connection between overlapping electronic orbitals and resultant spin configurations of participating electrons.

Second, $Gd_5(Si_xGe_{1-x})_4$ giant magnetocaloric compounds have been studied as materials of interest using the HP setup. These materials exhibit a tunable T_c with Si-doping which possesses potential applications to magnetic refrigerators that operate near room temperature. Magnetic refrigeration is an environmentally- and energy-friendly technology which uses adiabatic demagnetization of ferromagnetic substances to generate cooling power. The results indicate that pressure can alter the crystal structures and magnetic properties (T_c) similar to Si-doping. For crystal structure, the pressure-induced O(II) $\rightarrow$ M transition involves a martensitic-like process

that has been extensively addressed for the analogous case of Si-doping. For magnetic properties, pressure increases T_c linearly due to the enhanced overlapping between Si $3p$ (Ge $4p$) and Gd $5d$ conduction states which effectively mediates the FM interactions as a result of uniform lattice compression. The qualitative correspondence between two counterparts can be summarized in P-T phase diagram, where the most notable features found in the x-T phase diagram are reproduced.

The pressure studies were also extended to low-x region ($0 < x \leq 0.075$) to investigate the emergence of FM order from within the Gd_5Ge_4 AFM-O(II) parent compound. It is found that the materials display a mixed AFMO-(II) and FM-O(I) ground state resulting in low saturation magnetization, and pressure can remove the magneto-structural inhomogeneity by fully restoring the magnetization that is found in higher x samples ($x \geq 0.125$). This inhomogeneous magneto-structural ground state results in a x-dependent dT_c/dP, which is unlike the nearly constant dT_c/dP for $0.125 \leq x \leq 0.5$ where pressure only stabilizes the FM order.

Finally, the quantitative correspondence between Si-doping and pressure was examined by comparing their dT_c/dVs in order to decipher whether the magnetic properties of these materials are solely macroscopically volume-dependent. The results show that Si-doping increases T_c much faster than pressure for a given unit cell volume change. A local lattice contraction is found around Si atoms as a result of atomic substitution. This local contraction yields remarkable chemical pressure and responsible for a faster T_c increase due to greatly enhanced Si $3p$-Gd $5d$ hybridization. This adds a new dimension to the former understanding that macroscopic volume contraction alone is the dominant driving force. The local contraction also enables Si atoms to become an efficient FM exchange pathway that facilitates the FM percolation within the material.

7.2. Future work

7.2.1. Compositional homogeneity of the low-x region

As addressed in Chapter 5, the low-x ($0 < x \leq 0.75$), low temperature region of the phase diagram is characterized by magneto-structural inhomogeneity due to coexistence of FM-O(I) and AFM-O(II) phases. The driving force behind this phase separation was preliminarily attributed to an incomplete AFM-O(II)'FM-O(I) phase transition. However, an alternative explanation can be given based on atomic scale variations in Si composition. Whether Si atoms are homogeneously distributed at the atomic-scale, or inhomogeneously distributed in Si-rich (FM(O(I))) and Ge-rich (AFM(O(II))) clusters remains to be demonstrated. As suggested in Chapter 5, element-specific real space mapping, like energy dispersive x-ray spectroscopy (EDX) in the electron microscope (SEM/TEM) or x-ray fluorescence microprobe imaging, are suitable tools for probing homogeneity of Si composition at the nano and micro scale.

Besides real-space mapping probes, other synchrotron techniques such as XAFS [**55**] or diffuse scattering [**103**] can also probe the compositional inhomogeneity by probing Si-Si, Si-Ge and Ge-Ge pair correlations. For XAFS, one can see if a theoretical model based on a random population of Si among three inequivalent crystallographic sites is able to fit the experimental data, as addressed in Appendix A. The inconsistency between the experiment and the theory will emerge if Si tends to form a cluster in which the distribution of Si-Si and Si-Ge pairs is inconsistent with a random alloy for the given composition. For diffuse scattering, if Si atoms are randomly populated without any short range order, then one only observes sharp Bragg peaks in the diffraction pattern. While if Si atoms are not randomly populated and short range order exists (not a solid solution), then the intensity of the Bragg peaks is diminished and some

of the scattered intensity appears as "diffuse" scattering. However, diffuse scattering is more easily interpreted using single crystalline samples. An alternative approach is to measure the total scattering intensity and employ the pair distribution analysis method that is suitable for powder samples. Details of diffuse scattering can be found in Ref. [**103, 104**]

7.2.2. Microstructural analysis

To the writer's knowledge, microstructural work of $Gd_5(Si_xGe_{1-x})_4$ compounds is relatively scarce. Most of the work was dedicated to the study of magnetic and structural properties. It has been reported in Ref. [**105**] that a field-induced AFM(O(II)) $\rightarrow$ FM(O(I)) transition was observed in a Gd_5Ge_4 sample using a 30×30 μm^2 Hall probe imaging, and the obtained FM domain size is about 60 $\sim$ 300 μm. Though the AFM(O(II)) and FM(O(I)) domain size distribution was not investigated in this work, information of domain size can be determined by the integral breadth of corresponding structural Bragg peaks acquired in the mixed phase region studied in this work (Fig. 5.3). Since the fraction of FM-O(II) phase increases with applied field as shown in Fig. 5.3, one will expect that the width of its corresponding Bragg peaks would become narrower and the intensity would increase as the FM domain size grows. Details for determining domain size using the integral breadth of Bragg peak can be found in Ref. [**104**].

The importance of the microstructural work also lies in if the materials are structurally homogeneous. If the microstructure is not homogeneous and there are some countable point or line defects such as interstitials, vacancies or dislocations, they could possibly influence the dynamics of the phase transition. For example, these defects might perform as pinning centers hindering the FM domain growth or switching. These questions will be clarified if more microstructural work is brought to the forum.

7.2.3. Experimental setup

For experimental setup, the magnetic field used in HP setup is limited by the open-gap of the electromagnet due to DAC size. In this thesis, the maximum field strength is only 0.7 T. A smaller DAC adapted into a superconducting magnet might be considered if high magnetic field is the key for study interest. However, this type of DAC is usually not membrane driven and requires ex-situ pressure calibration, which is more time-consuming than the current setup. In addition, XAFS measurements for materials of interest under high pressure were not carried out in this thesis work due to unavoidable Bragg diffraction peaks from the diamond anvils appearing in extended energy region. This is because of the use of single crystalline diamond anvils. Polycrystalline diamond anvils are recommended to probe XAFS with pressure. However, the polycrystalline anvil is usually optically opaque and may not be suitable for in-situ ruby fluorescence pressure calibration.

7.2.4. Remaining questions for Si-doping and pressure

For $Gd_5(Si_xGe_{1-x})_4$, although it has been addressed in Chapter 6 that pressure contracts three lattice constants similarly to Si-doping, whether the most contracted $\vec{a}$-axis in M phase leads to the faster T_c increase viz-*à*-viz local contraction is unclear. In order to verify this, uniaxial pressure-studies of T_c in single crystalline samples with (100), (010) and (001) orientations are needed. This will determine whether the contraction of $\vec{a}$-axis increases T_c faster than the other two.

7.2.5. Other magnetocaloric material suitable for HP study

Besides $Gd_5(Si_xGe_{1-x})_4$, $Tb_5(Si_xGe_{1-x})_4$ for example, is a very close family to $Gd_5(Si_xGe_{1-x})_4$ worth of HP study. Unlike $Gd_5(Si_xGe_{1-x})_4$ whose low temperature saturation magnetization is $\sim$ 200 emu/g and with FM-O(I) phase for $x \geq 0.125$, the low temperature magnetization of $Tb_5(Si_xGe_{1-x})_4$ increases with x and the samples perform distinct hysteresis curves [**106**]. It has been reported that $Tb_5(Si_xGe_{1-x})_4$ sample has a mixed FM-M+O(I) phase at low temperature [**107**] and the level of this inhomogeneity may be x-dependent and thus results in different ground states. It is worth comparing chemical pressure with physical pressure effects in these related compounds, as well.

References

[1] E. Warburg, Ann. Phys. **13**, 141 (1881)

[2] Wikipedia, http://en.wikipedia.org/wiki/Magnetic_ refrigeration.

[3] P. Debye, Ann. Phys. **81**, 1154 (1926).

[4] W. F. Giauque, J. Am. Chem. Soc. **49**, 1864 (1927).

[5] V. K. Pecharsky and K. A. Gschneidner, Jr., J. Magn. Magn. Mater. **200**, 44 (1999).

[6] C. Magen, Ph.D thesis, University of Zaragoza.

[7] S. Fujieda, A. Fujita and K. Fukamichi, Appl. Phys. Lett. **81**, 1276 (2002).

[8] A. Fujita, S. Fujieda, Y. Hasegawa and K. Fukamichi, Phys. Rev. B **67**, 104416 (2003).

[9] F. X. Hu, B. G. Shen, J. R. Sun, G. J. Wang and Z. H. Cheng, Appl. Phys. Lett. **80**, 826 (2002).

[10] H. Wada and Y. Tanabe, Appl. Phys. Lett. **79**, 3302 (2001).

[11] H. Wada, T. Morikawa, K. Taniguchi, t. Shibata, Y. Yamada and Y. Akishige, Physica B **328**, 114 (2003).

[12] Z. B. Guo, Y. W. Du, J. S. Zhu, H. Huang, W. P. Ding and D. Feng, Phys. Rev. Lett. **78**, 1142 (1997).

[13] V. K. Pecharsky and K. A. Gschneidner Jr., J. Appl. Phys. **90**, 4614 (2001).

[14] V. K. Pecharsky and K. A. Gschneidner Jr., Adv. Mater. **13**, 683. (2000).

[15] V. K. Pecharsky and K. A. Gschneidner Jr., Adv. Cryo. Eng. **43**, 1729. (1998).

[16] L. Morellon, C. Magen, P. A. Algarabel, M. R. Ibarra and C. Ritter, Appl. Phys. Lett. 79, 1318 (2001).

[17] V. V. Ivtchenko, V. K. Pecharsky and K. A. Gschneidner Jr., Adv. Cryo. Eng. **46A**, 405. (2000).

[18] V. K. Pecharsky and K. A. Gschneidner, Jr, J. Alloys. Compd. **260**, 98 (1997).

[19] W. Choe, V. K. Pecharsky, A. O. Pecharsky, K. A. Gschneidner Jr., V. G. Young, Jr., and G. J. Miller, Phys. Rev. Lett. **84**, 4617 (2000).

[20] V. K. Pecharsky, A. P. Holm, K. A. Gschneidner Jr., and R. Rink, Phys. Rev. Lett. **91**, 197204 (2003).

[21] V. K. Pecharsky and K. A. Gschneidner Jr., Phys. Rev. Lett. **78**, 4494 (1997).

[22] J.R. Sun, R.X. Hu and B.G. Shen, Phys. Rev. Lett. **85**, 4191 (2000).

[23] L. Morellon, J. Blasco, P.A. Algarabel, and M. R. Ibarra, Phys. Rev. B **62**, 1022 (2000).

[24] H. Tang, V. K. Pecharsky, G. D. Samolyuk, M. Zou, K. A. Gschneidner, Jr., V. P. Antropov, D. L. Schlagel, and T. A. Lograsso, Phys. Rev. Lett. **93**, 237203 (2004).

[25] V. K. Pecharsky and K. A. Gschneidner Jr. , Appl. Phys. Lett. **70**, 3299 (1997).

[26] Ya. Mudryk, A. P. Holm, K. A. Gschneidner Jr., and V. K. Pecharsky, Phys. Rev. B **72**, 064442 (2005).

[27] Ya. Mudryk, D. Paudyal, V. K. Pecharsky and K. A. Gschneidner, Jr., Phys. Rev. B **77**, 024408 (2008).

[28] L. Morellon, Z. Arnold, P. A. Algarabel, C. Magen, M. R. Ibarra and Y. Skorokhod. J. Phys.: Condens. Matter. **16**, 1623 (2004).

[29] C. Magen, Z.Arnold, P. A. Algarabel, L. Morellon, Y. Skorokhod, P. A. Algarabel, M. R. Ibarra, and J. Kamarad, Phys. Rev. Lett. **91**, 207202 (2003).

[30] D. Paudyal, V. K. Pecharsky, K. A. Gschneidner, Jr., and B. N. Harmon, Phys. Rev. B **73**, 144406 (2006).

[31] F. Casanova, S. d. Brion, A. Labarta, and X. Batlle. J. Phys. D: Appl. Phys. **38**, 3343 (2005).

[32] J. W. Freeland, J. C. Lang, G. Srajer, R. Winarski, D. Shu, and D. M. Mills, Rev. Sci. Instrum. **73**, 1408 (2002).

[33] K. Hirano, K. Izumi, T. Ishikawa, S. Annaka, and S. Kikuta, Jpn. J. Appl. Phys. **30**, L407, (1991); J. C. Lang and G. Srajer, Rev. Sci. Instrum. **66**, 1540 (1995).

[34] G. Schutz et al., Phys. Rev. Lett. **58**, 737 (1987); P. Carra and M. Altarelli, ibid. **64**, 1286 (1990); J. Stohr, J. Magn. Magn. Mater. **200**, 470 (1997).

[35] N. Spaldin, magnetic materials: fundamentals and device applications, Cambridge Press (2003).

[36] R. C. O'handley, modern magnetic materials: principles and applications, 2000.

[37] D. J. Keavney, S. H. Cheung, S. T. King, M. Weinert, and L. Li, Phys. Rev. Lett. **95**, 257201 (2005).

[38] D. Haskel, G. Srajer, J. C. Lang, J. Pollmann, C. S. Nelson, J. S. Jiang, and S. D. Bader, Phys. Rev. Lett. **87**, 207201 (2001).

[39] J. W. Freeland, K.E. Gray, L. Ozyuzer, P. Berghuis, E. Badica, J. Kavich, H. Zheng, and J. F. Mitchell, Nature Mater. **4**, 62 (2005).

[40] T. Zhao, A. Scholl, F. Zavaliche, H. Zheng, M. Barry, A. Doran, K. Lee, M. P. Cruz, and R. Ramesh, Appl. Phys. Lett. **90**, 123104 (2007).

[41] C. I. Pearce, R. A. Pattrick and D. J. Vaughan, Rev. Mineralogy and Geochemistry, **61**, 127 (2006).

[42] R. J. Hemley and H.K. Mao, Mineralogical Magazine, **66**, 791 (2002).

[43] C. Carvallo, P. Sainctavit, M.-A. Arrio, N. Menguy, Y. Wang, G. Ona-Nguema, and S. Brice-Profeta, American Mineralogist, **93**, 880 (2008).

[44] T. Funk, P. Kennepohl, A. J. Di Bilio, W. A. Wehbi, A. T. Young, S. Friedrich, E. Arenholz, H. B. Gray, S. P. Cramer, J. Am. Chem. Soc. **126**, 5859 (2004).

[45] B. T. Thole, P. Carra, F. Sette, and G. van der Lann, Phys. Rev. Lett. **68**, 1943 (1992).

[46] P. Carra, B. T. Thole, M. Altarelli, and X. Wang, Phys. Rev. Lett. **70**, 694 (1993).

[47] C. T. Chen, Y. U. Idzerda, H. J. Lin, N. V. Smith, G. Meigs, E. Chaban, G. H. Ho, E. Pellegrin, and F. Sette, Phys. Rev. Lett. **75**, 152 (1995).

[48] J. Jin, S. Ohkoshi, and K. Hashmoto, Adv. Mater. **16**, 48 (2004).

[49] M. Popovici, M. Gich, D. Niznansky, A. Roig, C. Savii, L. Casas, E. Molins, K. Zaveta, C. Enache, J. Sort, S. de Brion, G. Chouteau, and J. Nogués, Chem. Mater. **16**, 5542 (2004).

[50] Y. C. Tseng, N. M. Souza-Neto, D. Haskel, M. Gich,C. Frontera, A. Roig, M. van Veenendaal, and J. Nogués, Phys. Rev. B **79** 094404 (2009).

[51] Y. Z. Yoo, O. Chmaissem, S. Kolesnik, A. Ullah, L. B. Lurio, D. E. Brown, J. Brady, B. Dabrowski, C. W. Kimball, M. Haji-Sheikh and A. P. Genis, Appl. Phys. Lett. **89**, 124104 (2006).

[52] T. Takeda and S. Ohara, J. Phys. Soc. Jpn. **37**, 275 (1974).

[53] Y. Choi, Y.C. Tseng, D. Haskel, D.E. Brown, D. Danaher and O. Chmaissem, Appl. Phys. Lett. **93**, 192 (2008).

[54] Y. Choi, Y. Z. Yoo, O. Chmaissem, A. Ullah, S. Kolesnik, C. W. Kimball, D. Haskel, J. S. Jiang and S. D. Bader, Appl. Phys. Lett. **91**, 022503 (2007).

[55] E. A. Stern, Phys. Rev. B **10**, 3027 (1974); P. A. Lee and J. B. Pendry, ibid. **11**, 2795 (1975).

[56] S. Kelly, "Basics of fundamental XAFS analysis",
http://cars9.uchicago.edu/xafs/NSLS_EDCA/July2003/Kelly.pdf

[57] M. Newville, "fundamentals of XAFS",
http://cars9.uchicago.edu/xafs/xas_fun/xas_fundamentals.pdf

[58] J. Als-Nielsen and D. McMorrow, Elements of Modern X-ray Physics, Wiley published.

[59] A. P. Hammersley, S. O. Svensson, M. Hanfland, A. N. Fitch, and D. Hausermann, High Press. Res., **14**, 235 (1996).

[60] L. B. McCusker, R. B. Von Dreele, D. E. Cox, D. Louër and P. Scardi, J. Appl. Cryst., **32**, 36 (1999).

[61] HPCAT, Carnegie Institution of Washington,
http://www.hpcat.aps.anl.gov/16ID-B.htm

[62] M. Suzuki, N. Kawamura, M. Mizumaki, A. Urata, H. Maruyama, S. Goto, T. Ishikawa, Jpn. J. Appl. Phys. **37**, L1488 (1998).

[63] D. Haskel, Y. C. Tseng, J. C. Lang and S. Sinogeikin, Rev. Sci. Instrum. **78**, 083904 (2007).

[64] S. Kelly, R. Ingalls, F. Wang, B. Ravel, and D. Haskel, Phys. Rev. B **57**, 7543 (1998).

[65] A. Dewaele, P. Loubeyre and M. Mezouar, Phys. Rev. B **70**, 094112 (2004).

[66] S. I. Zabinsky, J. J. Rehr, A. Ankudinov, R. C. Albers and M. J. Eller, Phys. Rev. B **52**, 2995 (1995).

[67] http://cars9.uchicago.edu/ifeffit/

[68] R. A. Forman, G. J. Piermarini, J. D. Barnett and S. Block, Science **176**, 284 (1972).

[69] K. Syassen, High. Press. Res. **28**, 75 (2008).

[70] D. D. Ragan et al., J. Appl. Phys. **72**, 5539 (1992); B. A. Weinstein, Rev. Sci. Instrum. **57** 910 (1986); A. D. Chijioke et al., J. Appl. Phys. **98**, 114905 (2005).

[71] D. Haskel, Y. C. Tseng, N. M. Souza Neto, J. C. Lang, S. Sinogeikin, Ya. Mudryk, K. A. Gschneidner Jr. and V. Pecharsky, High Press. Res. **28**, 185 (2008).

[72] Y. C. Tseng, D. Haskel, J. C. Lang, Ya. Mudryk, V. K. Pecharsky and K. A. Gschneidner, J. Appl. Phys. **103**, 07B301 (2008).

[73] D. Haskel, Y. B. Lee, B. N. Harmon, Z. Islam, J. C. Lang, G. Srajer, Ya. Mudryk, K. A. Gschneidner, V. K. Pecharsky, Phys. Rev. Lett. **98**, 247205 (2007).

[74] L. Tan, A. Kreyssig, J. W. Kim, A. I. Goldman, R. J. McQueeney, D. Wermeille, B. Sieve, T. A. Lograsso,D. L. Schlagel, S. L. Budko, V. K. Pecharsky, and K. A. Gschneidner, Jr. Phys. Rev. B **71**, 214408 (2005).

[75] C. Magen, L. Morellon, P. A. Algarabel, M. R. Ibarra, Z. Arnold, J. Kamarad, T. Lograsso, D. L. Schlagel, V. K. Pecharsky, A. O. Tsokol, K. A. Gschneidner. Phys. Rev. B **72**, 024416 (2005).

[76] A. Magnus, G. Carvalho, Cleber S. Alves, Ariana de Campos, Adelino A. Coelho, Sergio Gama, Flavio C. G. Gandra, Pedro J. von Ranke, Nilson A. Oliveira. J. Appl. Phys. **97**, 10M320 (2005).

[77] M. A. Ruderman and C. Kittel, Phys. Rev. **96**, 99 (1954); T. Kasuya, Prog. Theor. Phys. **16**, 45 (1956); K. Yosida, Phys. Rev. **106**, 893 (1957).

[78] P. W. Anderson, Phys. Rev. B **79**, 350 (1950).

[79] Y. C. Tseng, D. Haskel, J. Lang, S. Sinogeikin, Y. Mudryk, V. K. Pecharsky and K. A. Gschneidner, Phys. Rev. B **76**, 014411 (2007).

[80] D. Paudyal, V. K. Pecharsky, K. A. Gschneidner, Jr., and B. N. Harmon, Phys. Rev. B **75**, 094427 (2007).

[81] A. P. Holm, V. K. Pecharsky, K. A. Gschneidner, Jr., R. Rink, and M. Jirumanus, Rev. Sci. Instrum. **75**, 1081 (2004).

[82] Martensitic, G. B. Olson and W. S. Owen (ASM International, Materials Park, Ohio, 1992), Chaps. 7, 9, and 10.

[83] P. Porsch, M. Kallmayer, T. Eichhorm, G. Jakob, H. J. Elmers, C. A. Jenkins, C. Felser, R. Ramesh, and M. Huth, Appl. Phys. Lett. **93**, 025501 (2008).

[84] V. K. Pecharsky and K. A. Gschneidner Jr., Pure Appl. Chem. **79**, 1383 (2007).

[85] S. B. Roy, M. K. Chattopadhyay, P. Chaddah, J. D. Moore, G. K. Perkins, L. F. Cohen, K. A. Gschneidner, and V. K. Pecharsky, Phys. Rev. B **74**, 012403 (2006).

[86] Y. C. Tseng, D. Haskel, N. M. Souza-Neto,Y. Mudryk, V. K. Pecharsky and K. A. Gschneidner, Phys. Rev. B. **78**, 214433 (2008).

[87] R. Glocker and H. Schreiber, Ann. Physik., **85**, 1089 (1928).

[88] R. Jaramillo, T. F. Rosenbaum, E. D. Isaacs, O. G. Shpyrko, P. G. Evans, G. Aeppli, and Z. Cai, Phys. Rev. Lett. **98**, 117206 (2007).

[89] A. F. Goncharov, V. V. Struzhkin, M. S. Somayazulu, R. J. Hemley and H. K. Mao, Science, **273**, 218 (1986).

[90] Y. Joly, Phys. Rev. B **63**, 125120 (2001).

[91] V. I. Anisimov, F. Aryasetiawan, and A. I. Lichtenstein, J. Phys.: Condens. Matter. **9**, 767 (1997).

[92] B. N. Harmon, V. P. Antropov, A. I. Lichtenstein, I. V. Solovyev, and V. I. Anisimov, J. Phys. Chem. Solids **56**, 1521 (1995).

[93] O. K. Andersen and O. Jepsen, Phys. Rev. Lett. **53**, 2571 (1984).

[94] U. von Barth and L. Hedin, J. Phys. **C5**, 1629 (1972).

[95] W. Choe, A. O. Pecharsky, M. Worle and G. J. Miller, Inorg. Chem. **42**, 8323 (2003).

[96] S. Misra and G. J. Miller, J. Solid State Chem. **179**, 2290 (2006).

[97] A. O. Pecharsky, K. A. Gschneidner Jr., V. K. Pecharsky and C. E. Schindler, J. Alloys Compd. **338**, 126 (2002).

[98] J. Y. Kim, D. Y. Koo and J. H. Park, Phys. Rev. Lett. **96**, 047205 (2006).

[99] P. Shanthakumar, M. Balasubramanian, D. M. Pease, A. I. Frenkel, D. M. Potrepka, V. Kraizman, J. I. Budnick, and W. A. Hines, Phys. Rev. B **74**, 174103 (2006).

[100] Z. Sun, W. Yan, H. Oyanagi, Z. Pan, and S. Wei, Phys. Rev. B **74**, 092101 (2006).

[101] E. Fermi, Nuclear Physics. University of Chicago Press (1950).

[102] P. A. M. Dirac , Proc. Roy. Soc. (London), **A114**, 243 (1927).

[103] W. A. Wooster, diffuse x-ray reflections from crystals, Oxford, Clarendon Press (1962).

[104] B. E. Warren, x-ray diffraction, chapter 12, Dover Press (1968).

[105] J. D. Moore, G. K. Perkins, Y. Bugoslavsky, L. F. Cohen, M. K. Chattopadhyay, S. B. Roy, P. Chaddah, K. A. Gschneidner, and V. K. Pecharsky, Phys. Rev. B **73**, 144426 (2006).

[106] Y. C. Tseng, D. Haskel, N. M. Souza-Neto,Y. Mudryk, V. K. Pecharsky and K. A. Gschneidner, unpublished.

[107] L. Morellon, C. Ritter, C. Magen, P. A. Algarabel, and M. R. Ibarra, Phys. Rev. B **68**, 024417 (2003); C. Ritter, L. Morellon, P. A. Algarabel, C. Magen, and M. R. Ibarra, Phys. Rev. B **65**, 094405 (2002).

APPENDIX A

Local structure analysis using IFEFFIT calculation

A.1. Introduction to IFEFFIT

IFEFFIT is a program for analyzing XAFS data [**67**], also a package allowing graphical data manipulation and analysis. It is designed to fit experimental XAFS spectra to theoretical calculations from FEFF [**66**]. IFEFFIT contains several graphical user interface (GUI) programs including ATHENA, ARTEMIS, TKATOMS and SIXPACK. This thesis uses ATHENA and ARTEMIS primarily. This chapter provides the details of the local structure probes of the selected Si(Ge) atom using IFEFFIT program which is not described in Chapter 6.

A.2. Data analysis process

The first step to analyze data is to use ATHENA GUI program to generate XAFS spectrum. In ATHENA, an optimized spectrum with proper background removal, taking Ge K -edge for example (shown in A.1(a)), can be gained by manipulating the interfacial functions provided by the program (not shown here). A k-dependent spectrum (Fig. A.1(b)) converted from $\mu(E)$ diagram will enter the ARTEMIS program to run the fitting. More details for XAFS analysis can be found in Chapter 2.

Figures A.2−4 show ARTEMIS interface for running FEFF fittings. Figure A.2 shows several FEFF calculations for selected atoms (Si or Ge). In this thesis, Si and Ge FEFFs were calculated simultaneously. Because the three inequivalent crystallographic sites T_1, T_3, and T_3 can be populated by either Si or Ge, each site was assigned two FEFFs to calculate the different

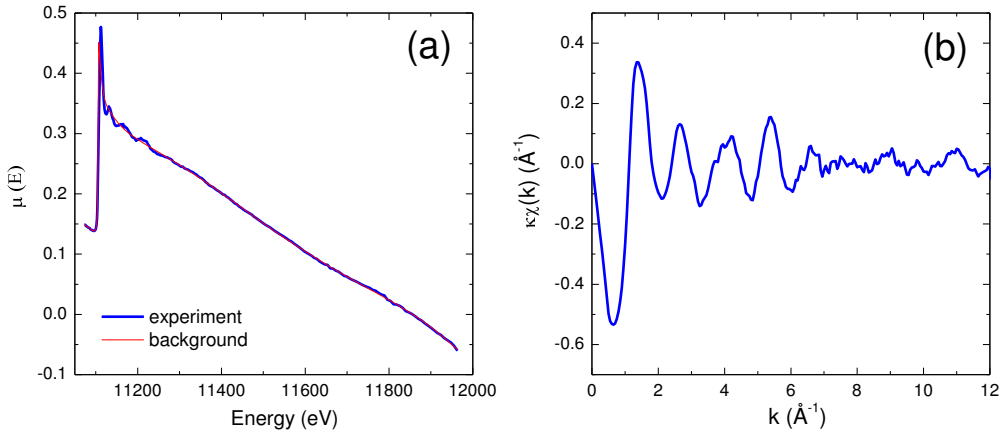

Figure A.1. (a)Ge K -edge XAFS raw data with background removal and its (b) k -dependent spectrum.

contributions from the two doping counterparts at the same site to the absorbing atom. For example, in Fig. A.2, FEFF0 and FEFF1 represent the photoelectron scattering contributions of Ge ($T_1(x)$) and Si (1-$T_1(x)$) to the selected Ge atom, respectively, where $T_1(x)$(1-$T_1(x)$) is defined as the occupancy of Ge (Si) at T_1 site. In the calculations, T_1 (x), T_2 (x), and T_3 (x) were also set to be variables and restrained as ≤ 1. The results for $T_1(x)$, $T_2(x)$, and $T_2(x)$ are all close to 0.5, which agrees well with what has been reported in Ref. [**19**]. A FEFF path is characterized with the related interatomic distance (bond length) for single scattering path (Reff), the amplitude of path (amp), and the photoelectron scattering, as also depicted in Fig. A.2. The paths with amplitude lower than 15 were not chosen due to insignificant photoelectron scattering effect. In addition, paths with Reff difference smaller than 0.15 Å were merged in order to reduce the total number of the paths in calculation. The value of 0.15 was gained from

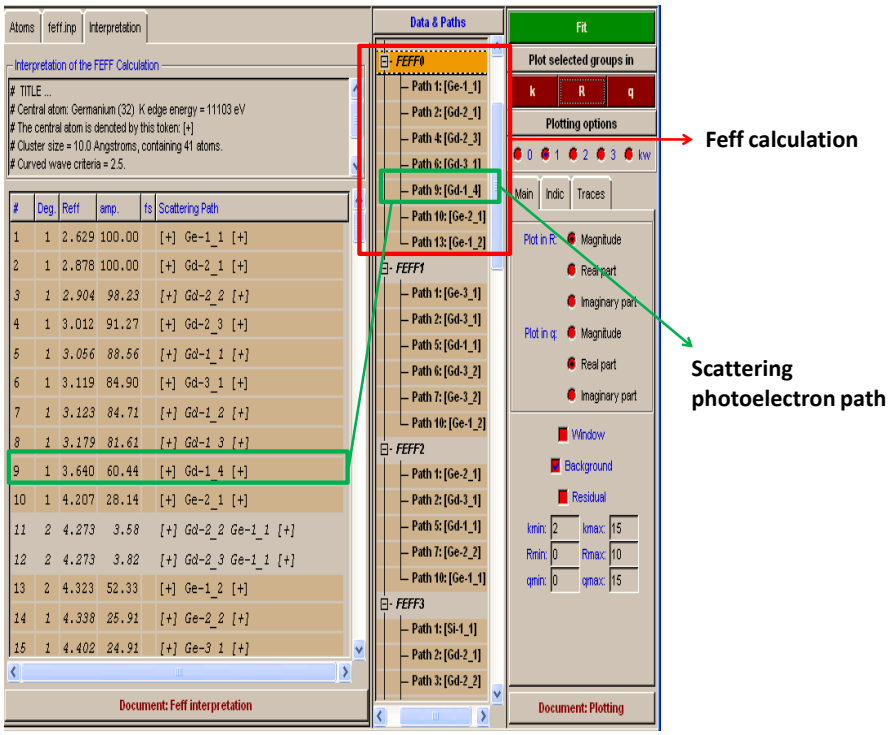

Figure A.2. ARTEMIS interface with FEFF calculations (red) and scattering photoelectron paths (green).

$\Delta r = \pi/2\Delta k$, which is used as the general way to determine the XAFS resolution. Here, $\pi = 3.14$ and Δk is 8 $Å^{-1}$.

The path parameters include degeneracy of path (N), passive electron reduction factor (S02), energy shift (delE0), bond length change (delR), and mean squared displacement ($sigma^2$) while not shown here. One should note that the degeneracy of the merged paths should be modified accordingly. Here, $sigma^2$ was set to be 0.003 as a standard value for the calculation.

In order to investigate the element-specific local structure modifications, variables for bonding compressibilities were assigned to Si and Ge independently. As can be seen in Fig. A.3, alpha,

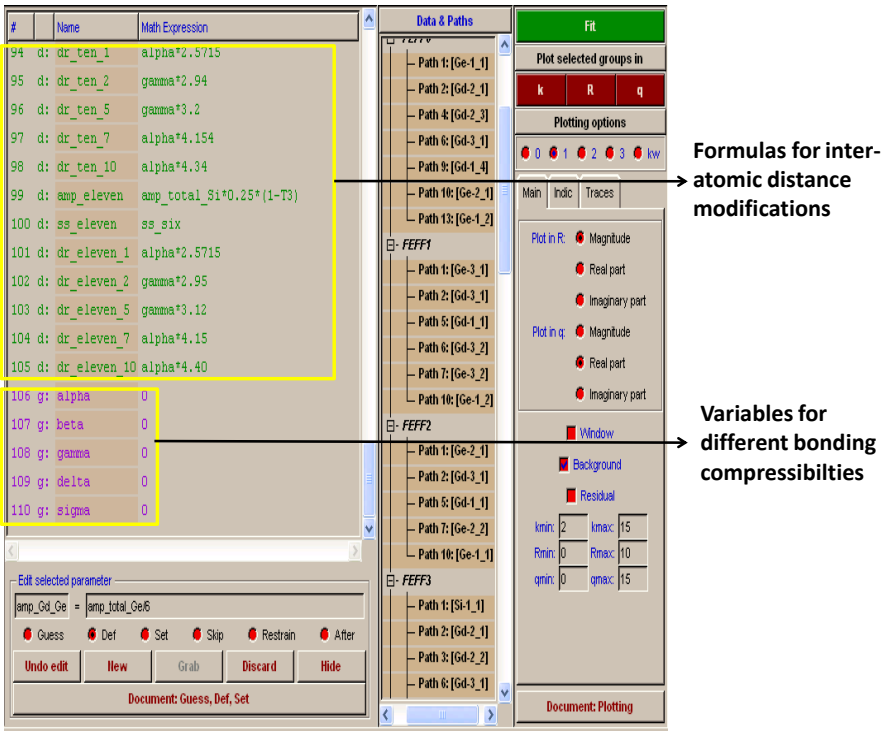

Figure A.3. FEFF fitting parameters.

beta, gamma, delta and sigma represent $\Delta l/l$, where l is bond length, for Si-Si, Si-Ge, Ge-Ge, Ge-Gd, and Si-Gd, respectively. Therefore, the resultant interatomic distance change can be expressed as l × compressibility (alpha, beta, etc.) as the formulas presented in Fig. A.3. The fitting k range is 2−10 Å^{-1}, and R range is 2−4.2 Å considering the FEFF paths included in the first two atomic shells.

The fitting results are shown in Fig. A.4. Usually the R-factor is expected to be no more than 5 % for a good fit. The sign for the compressibility indicates either contraction or expansion for the selected, relative interatomic distance. For example, in this case, alpha is -0.0055, which

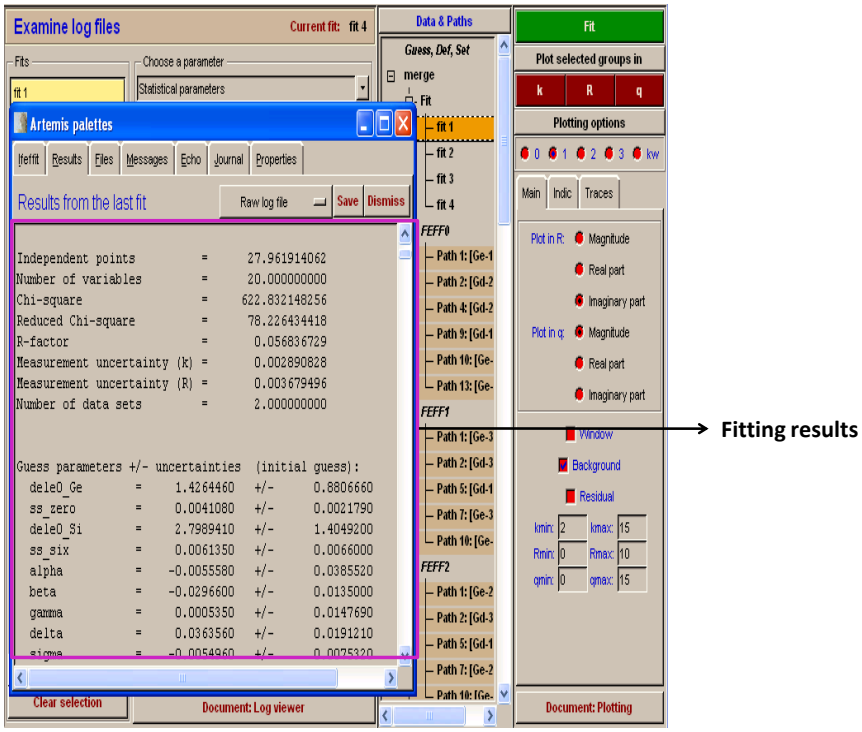

Figure A.4. FEFF fitting results.

means in average, the Si-Si interatomic distances within the first two atomic shells are contracted. The average interatomic distances count the scattering paths (Reff) over the T_1, T_3, and T_3 sites since the XAFS probes the average of the three. The resultant k-dependent spectrum and the Fourier transform of Ge K -edge XAFS with their fittings are illustrated in Fig. A.5. One can see in FT result, the experimental and theoretical results are in fair agreement within the first two atomic shells (2−4.2 Å).

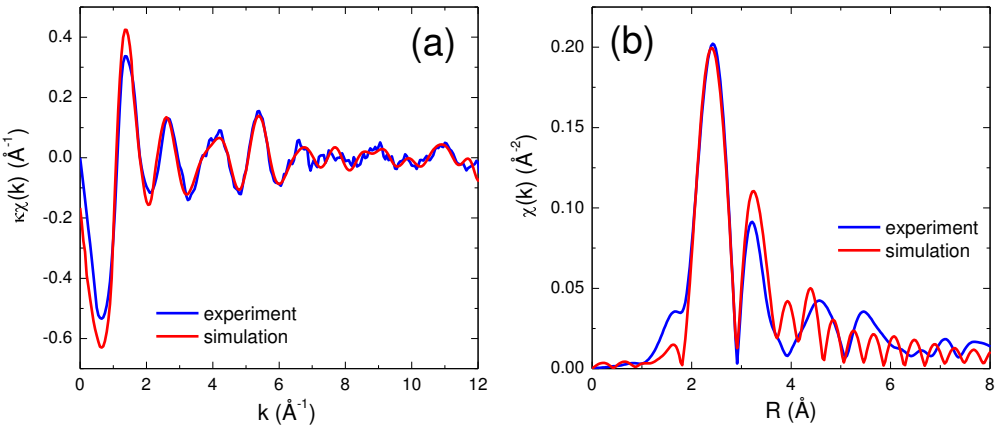

Figure A.5. (a) k -dependent and (b) Fourier transform of Ge K -edge XAFS with FEFF fitting results.

APPENDIX B

FDMNES calculations

B.1. Introduction

The FDMNES program [**90**] calculates the x-ray absorption spectroscopy of the selected atomic species in the materials. It gives the absorption cross sections of photons around the ionization edge, which is also x-ray absorption near edges structure (XANES). The code uses two techniques of monoelectronic calculations. The first is based on the Finite Difference Method (FDM) to solve the Schrödinger equation. The second uses the Green function (multiple scattering) on a muffin-tin approximation. The second is less precise but faster and was employed in this thesis to calculate circular polarization. In this thesis, both XANES, XMCD spectra were calculated to compare with the experimental results as described in Chapter 6.

B.2. Program inputs

Figure B.1 shows the necessary codes for FDMNES calculation, including crystal structure, electronic configuration, and atomic position, etc. The program allows to calculate basic parameters first (crystal structure, atomic position, electronic configuration, etc.) and then to convolute later (energy shift, Fermi-level). Therefore, the convolution can be varied independently and added into the same calculation result without running the entire process again (as described in Fig. B.2).

```
Filout                                  file directory
Si/T1/Si_Si_Si/(010)_out
Range                                   energy range for scan
-15. 2. -8. 0.5 -5. 0.2 8. 1.0 20.
Green                                   Green function (muffin-tin approximation)
K Edge                                  selected edge
Polarization                            polarization orientation [000] in lattice and
0. 0. 0. 0. 1. 0.                       photon wave-vector In [010] direction
Rayon                                   muffin-tin cluster radius  (in Å)
 6.0
Spinorbit                               circularly polarized absorption
Density                                 density of state calculation
Absorber                                selected absorbing atom
4
Atom                                    atomic number, electronic configurations
 64 3  4 3 7. 0.   5 2 0.7 0.3  6 0 2. 0.
 32 3  3 2 5. 5.   4 0 1. 1.   4 1 2. 0.
 14 2  3 0 1. 1.   3 1 2. 0.
Spgroup                                 space group
 Pnma
Cryst                                   crystal structure, lattice parameters and atomic
7.51370 14.7920  7.78580,  90. 90. 90.  position
 1  0.02296    0.40318    0.18232
 1  0.67962    0.37732    0.82255
 1  0.14958    0.75000    0.51011
 2  0.84689    0.45984    0.52930
 2  0.02350    0.75000    0.10210
 2  0.26810    0.75000    0.87110
Arc                                     Fermi level convolution (in eV)
Efermi
-1.5
End
```

Figure B.1. Basic codes for FDMNES calculation.

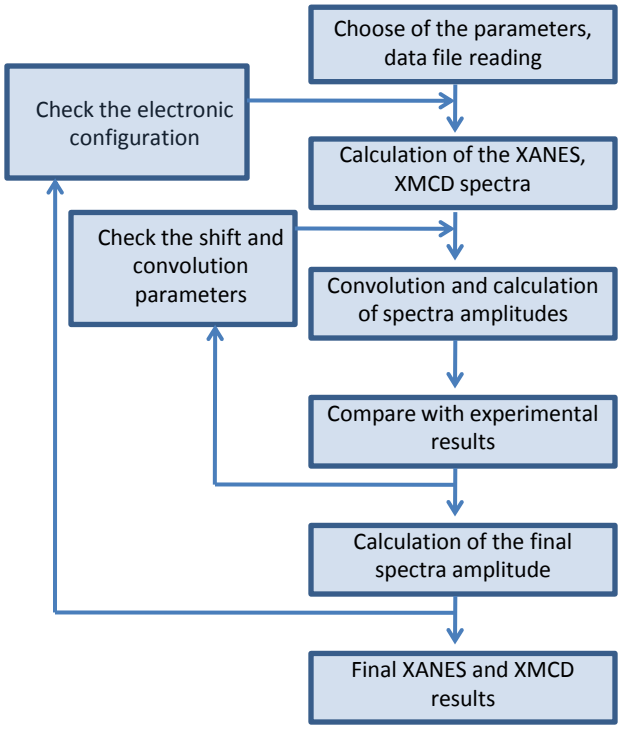

Figure B.2. Flow-chart for a complete FDMNES calculation process.

In the codes, command "spinorbit" is used to perform a spin-orbit coupling condition to calculate XMCD spectra. It generates two helicity-dependent XANES spectra (μ^+ and μ^-, described in Chapter 2) first, and XMCD spectrum is gained by taking the difference between the two XANES spectra, μ^+ - μ^- (equation (2.1)). In polarization option, the first [0,0,0] indicates that there is no specific polarization orientation within the crystallographic lattice wanted to probe. The second [0,1,0] indicates the direction of photon wave-vector. Because of the use of polycrystalline powders in the experiments and assuming the magnetic moments of the samples are randomly oriented, photon wave-vector of [1,0,0], [0,1,0], and [0,0,1] directions were considered (Fig. B.1 shows only [0,1,0]) in the calculation to probe the magnetic moments in

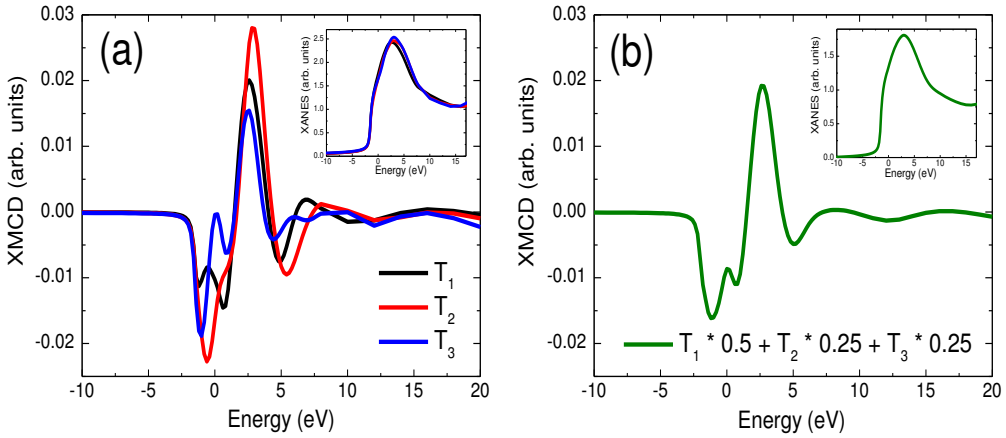

Figure B.3. Si K -edge XMCD (main) and XANES (inset) spectra collected from FDMNES for (a) T_1, T_2 and T_3 sites and (b) the average of the three sites for $Gd_5(Si_{0.5}Ge_{0.5})_4$.

entire sample volume. The final XMCD results are the average of the [1,0,0], [0,1,0], and [0,0,1] absorption spectra.

Figure B.2 shows the flow-chart for a complete calculation process employed in this thesis. As can be seen, convolution, energy shift, and electronic configuration, etc. may take a few times of adjustments during the entire calculation in order to obtain a better fit to the experimental results.

B.3. Examples

In this thesis, Si (Ge) K -edges XANES and XMCD are focused. For $Gd_5(Si_xGe_{1-x})_4$, Si (Ge) occupies three in-equivalent crystallographic sites. Therefore, the FDMNES calculations were run for the three sites independently, averaged with corresponding site occupancies [**19**] and then compared to the experimental results. For example, Fig. B.3(a) shows the Si K -edge

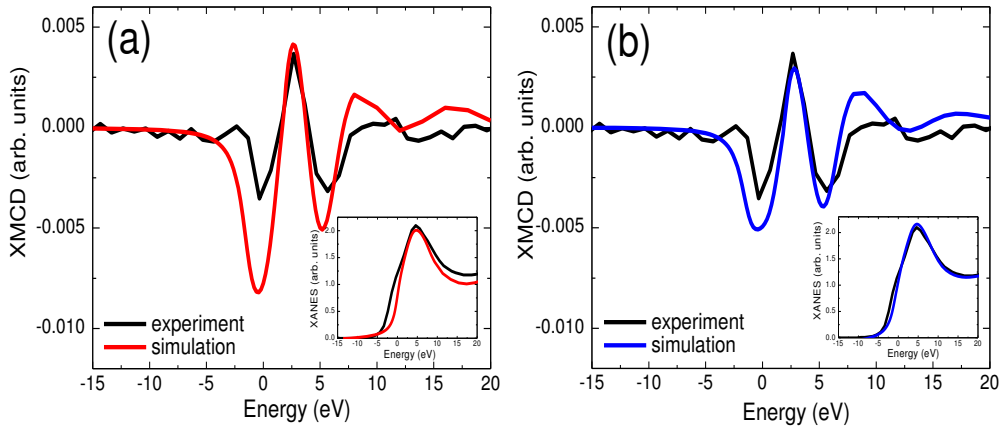

Figure B.4. Ge K -edge XMCD and XANES using (a) an automatic convolution width and (b) a convolution width of 1.9 eV.

XMCD (main) and XANES (inset) spectra for T_1, T_2 and T_3, for $Gd_5(Si_{0.5}Ge_{0.5})_4$ sample. This can be easily done by selecting the absorbing atom in codes (see Fig. B.1, Absorber). Fig. B.3(b) shows the sum of the three spectra with proper occupancies: T_1 = 50 %, T_2 = 25 %, and T_3 = 25 % [**19**]. The comparison for experimental an theoretical results is present in Fig. 6.6(b). FDMNES will determine the convolution width automatically. The convolution width depends on both the core level and the final state width. Nevertheless, it is possible to modify the convolution width with the keyword "*Gamma_hole*" as needed. For example, Fig. B.4(a) shows Ge K -edge XMCD (main) and XANES (inset) using the convolution width automatically determined by FDMNES, while the simulation result doesn't agree with the experimental one very well. The spectra can be improved significantly using *Gamma_hole* = 1.9 eV, as shown in Fig. B.4(b), where simulation and experiment are more consistent.